Diese Dissertation haben begutachtet:

....

TU WIEN

DISSERTATION

Precision measurements of the CKM-matrix element $|V_{cb}|$ and the form factors of semileptonic decays of B mesons

ausgeführt zum Zwecke der Erlangung des akademischen Grades eines Doktors der technischen Wissenschaften unter der Leitung von

Privatdoz. Mag.rer.nat. Mag.phil. Dr.rer.nat. Manfred Jeitler

E141

Atominstitut der Österreichischen Universitäten

eingereicht an der Technischen Universität Wien
Fakultät für Physik

von

Dipl.-Ing. Wolfgang Dungel

Matrikelnummer: 0125604
Leobendorferstrasse 48/4/8, 2100 Korneuburg

Wien, am 26. 11. 2009

Kurzfassung

Ein faszinierendes Problem in der Teilchenphysik ist eine Asymmetrie zwischen Materie und Antimaterie, die sich in der so genannten "CP-Verletzung" manifestiert. Innerhalb des Standardmodells wird dieser Effekt durch die Theorie der beiden japanischen Physiker Makoto Kobayashi und Toshihide Maskawa beschrieben, die unter anderem auf der Vorhersage einer dritten Generation von Quarks aufbaute. In diesem Modell wird die elektroschwache Wechselwirkung zwischen up- und down-artigen Quarks mit Hilfe einer 3×3 dimensionalen, unitären Matrix beschrieben, der so genannten "CKM Matrix", welche eine komplexe Phase enthält.

Im Rahmen dieser Arbeit wurden Hochpräzisionsmessungen des Betrages eines der Matrixelemente der CKM Matrix durchgeführt, welches als $|V_{cb}|$ bezeichnet wird und die Stärke der Kopplung zwischen Charm- und Bottom-Quark beschreibt. Die experimentellen Daten wurden durch das Belle Experiment in Tsukuba, Japan, aufgezeichnet. Aus den im Detektor nachgewiesenen Teilchenspuren werden zunächst Bottom-Zerfälle der Art $B \to D^* \ell \nu$ rekonstruiert, welche als "semileptonische Zerfälle" bezeichnet werden. ℓ stellt ein leichtes geladenes Lepton (Elektron oder Myon) dar und sowohl neutrale als auch geladene B Mesonen werden untersucht. Der Impuls des Neutrinos ist nicht direkt bestimmbar, aufgrund der Hermetizität des Detektors können allerdings alle restlichen Teilchenspuren verwendet werden, um den Impuls des ursprünglichen B Mesons zu bestimmen. Durch diesen neuartigen Rekonstruktionsansatz können hervorragende Auflösungen in den betrachteten kinematischen Größen erzielt werden.

Da innerhalb eines Mesons die Einflüsse aufgrund von Quantenchromodynamik eine wichtige Rolle spielen, ist es äußerst wichtig auch diese Prozesse zu studieren. Zu diesem Zweck wird eine effektive Feldtheorie verwendet, die speziell für diesen Zweck entwickelt wurde und einen Satz von Formfaktorparametern (ρ^2, $R_1(1)$ und $R_2(1)$) einführt. Um die korrekte Trennung von QCD-Effekten von jenen des CKM-Matrixelements zu erreichen, werden die Verteilungen in insgesamt vier Variablen betrachtet. Durch eine numerische

Anpassungsprozedur können sowohl $|V_{cb}|$ als auch die Formfaktorparameter mit hervorragender Genauigkeit bestimmt werden.

Die vorläufigen Resultate der Analyse von Zerfällen von neutralen B^0 Mesonen ergeben, basierend auf ungefähr 69000 rekonstruierten $B^0 \to D^{*-}\ell^+\nu_\ell$ Zerfällen, $\rho^2 = 1.293 \pm 0.045 \pm 0.029$, $R_1(1) = 1.495 \pm 0.050 \pm 0.062$, $R_2(1) = 0.844 \pm 0.034 \pm 0.019$ und $\mathcal{F}(1)|V_{cb}| = 34.4 \pm 0.2 \pm 1.0$ ([1]). Aus der Analyse von Zerfällen von geladenen B^+ Mesonen, basierend auf rund 27000 rekonstruierten $B^+ \to \bar{D}^{*0}\ell^+\nu_\ell$ Ereignissen, ergeben sich die vorläufigen Resultate $\rho^2 = 1.376 \pm 0.074 \pm 0.056$, $R_1(1) = 1.620 \pm 0.091 \pm 0.092$, $R_2(1) = 0.805 \pm 0.064 \pm 0.036$ und $\mathcal{F}(1)|V_{cb}| = 35.0 \pm 0.4 \pm 2.2$ ([2]). Der erste der angebenen Fehler stellt die statistische, der zweite die systematische Unsicherheit dar. Die Resultate der B^0 Analyse stellen die momentan präziseste Messung dieser Parameter dar.

Abstract

One of the fascinating problems in particle physics is an asymmetry between matter and anti-matter, manifested in the the so-called "CP-violation". Within the Standard Model, this effect is being described by a theory developed by the two japanese physicists Makoto Kobayashi and Toshihide Maskawa, which was based in part on the prediction of a third generation of quarks. Within this model the electroweak interaction between up- and down-type quarks is being described by a 3×3-dimensional matrix, the so-called "CKM matrix", which contains one complex phase.

This work describes high precision measurements of the magnitude of one of the CKM matrix elements, which is labeled as $|V_{cb}|$ and describes the strength of the coupling between charm and bottom quark. The experimental data has been recorded by the Belle experiment in Tsukuba, Japan. From particle tracks recorded by the detector, decays of the type $B \to D^* \ell \nu$ are being reconstructed, which are labeled "semileptonic decays". ℓ represents a light charged lepton (electron or muon) and both charged and neutral B mesons are being investigated. The momentum of the neutrino cannot be determined. However, due to the hermeticity of the detector we can use all the remaining particles to determine the momentum of the original B meson. This novel reconstruction ansatz allows to obtain excellent resolutions in each of the considered kinematic variables.

Within a meson, the effects of quantum chromodynamics play an important role. It is therefore essential to investigate these processes as well. An effective field theory is being used, which is specifically tailored to this purpose and introduces a set of form factor parameters ($\rho 2$, $R_1(1)$ and $R_2(1)$). To ensure the adequate separation of the effects of QCD from those of the CKM matrix element, the distributions of four variables are being investigated. A numerical fit allows to determine both $|V_{cb}|$ and the form factor parameters with excellent precision.

The preliminary results of the analysis of B^0 decays, based on about 69,000 reconstructed $B^0 \to D^{*-} \ell^+ \nu_\ell$ decays, are $\rho^2 = 1.293 \pm 0.045 \pm 0.029$, $R_1(1) =$

$1.495 \pm 0.050 \pm 0.062$, $R_2(1) = 0.844 \pm 0.034 \pm 0.019$ and $\mathcal{F}(1)|V_{cb}| = 34.4 \pm 0.2 \pm 1.0$ ([1]). The analysis of B^+ decays, based on about 27,000 reconstructed $B^+ \to \bar{D}^{*0}\ell^+\nu_\ell$ events, yields $\rho^2 = 1.376 \pm 0.074 \pm 0.056$, $R_1(1) = 1.620 \pm 0.091 \pm 0.092$, $R_2(1) = 0.805 \pm 0.064 \pm 0.036$ and $\mathcal{F}(1)|V_{cb}| = 35.0 \pm 0.4 \pm 2.2$ ([2]). The first of the errors stated above shows the statistical uncertainty, the second error gives the systematic one. The results of the B^0 analysis represent the most precise measurement of these parameters which is available up to date.

Contents

Chapter 1

Introduction

> *True glory consists in doing what deserves to be written,*
> *in writing what deserves to be read.*
>
> *Pliny the Elder*

The study of the decay $B \to D^* \ell \nu$ is an important item on the B physics agenda for many reasons. First, the total rate is proportional to the magnitude of the Cabibbo-Kobayashi-Maskawa (CKM) matrix element V_{cb} squared [3]. We can thus determine this quantity from the measurement of these decays. Second, $B \to D^* \ell \nu$ is a major background for charmless semileptonic B decays or semileptonic B decays with large missing energy. A precise knowledge of the form factors of this decay will thus help reducing systematic uncertainties in these analyses.

This work contains the results of two analyses investigating the decays of neutral and charged B mesons. The experimental data have been recorded with the Belle experiment situated in Tsukuba, Japan.

In the framework of Heavy Quark Effective Theory (HQET), these decays are described by three form factor parameters, ρ^2, $R_1(1)$ and $R_2(1)$ [4, 5] along with the fundmental parameter $|V_{cb}|$ times a form factor normalization $\mathcal{F}(1)$ derived from lattice QCD [6].

The analysis of $B^0 \to D^{*-}\ell^+\nu_\ell$ decays allows for a very precise determination of these parameters. Our analysis technique follows closely previous studies of this decay using $e^+e^- \to \Upsilon(4S)$ data [7, 8, 9], *i.e.*, we initially reconstruct only the D^* meson and the charged lepton, without making any requirement on the other B meson in the event. The main difference to earlier analyses [7, 8] is that we measure the CKM matrix element and all three HQET form factors of this decay simultaneously. Also, by using an enhanced reconstruction technique of the B meson four-momentum, we achieve a better resolution in the kinematic variables describing the $B^0 \to D^{*-}\ell^+\nu_\ell$ decay, which translates into an improved determination of the HQET form factors.

The numerous measurements of the B^0 mode which are available are unfortunately barely consistent [10], suggesting a hidden systematic uncertainty. To shed light on this inconsistency, we also investigate the related decay $B^+ \to \bar{D}^{*0}\ell^+\nu_\ell$ which carries different experimental systematics. This is also interesting because only few measurements of the B^+ mode are available in the literature [11, 12, 13].

This work is organized as follows:

In Chapter 2 the main motivation of this work is discussed. Precision measurements like those by the particle physics experiment Belle at the "B factory" KEKB allow to probe our understanding of the basic underlying physics of CP violation. This effect plays a major role in our picture of the evolution of the universe. The analysis of $B \to D^*\ell\nu$ decays allows to extract one of the fundamental parameters of the Standard Model related to this phenomenon, labeled $|V_{cb}|$.

In order to extract these experimental results, the interplay of effects due to the weak interaction and those due to Quantum chromodynamics (QCD) has to be probed. Chapter 3 is devoted to introducing the underlying theoretical framework. The most appropriate approach is to use an effective theory, which is specifically tailored to the problems at hand.

Chapter 4 is dedicated to the experimental setup of the Belle experiment, describing both the KEKB particle accelerator and the components of the Belle detector.

The reconstruction procedures, including extraction of the required decay cascade are the topic of Chapter 5. The procedure used to estimate the expected background is described there as well.

The fitting procedures used to extract both $|V_{cb}|$ and the parameters of the QCD effects in terms of form factors is described in Chapter 6. Additionally we present a direct test of the parametrization which is used in this procedure.

The results of these analyses are presented seperately for charged and neutral B mesons in Chapter 7.

Finally the conclusions drawn from the results presented in this work are given in Chapter 8.

The appendix contains some additional information on the main fit procedure and describes its validation.

Chapter 2

Theoretical motivation

There is a single light of science, and to lighten in any-where is to lighten it everywhere.

Isaac Asimov

2.1 Symmetries

One of the most powerful concepts in modern particle physics is that of symmetries. Assuming a symmetry holds means that if one knows the behavior of a given system (say the probability that a particle decays in a given way), one can then transform the system in a particular fashion and the result remains the same. One example for such a behavior is translation symmetry, which implies that physical observables are independent of the system's position in space. Translation symmetry is an example of a continuous symmetry: infinitesimal changes of the system are possible. According to Noether's theorem [14, 15], any continuous symmetry is related to a globally conserved quantity. E.g translation symmetry implies conservation of momentum and vice versa.

Not all transformations can be formulated in a continuous way. For example

the charge conjugation transformation C requires to change the sign of all internal quantum numbers, like the electric charge of a system. These are the so-called "discrete" symmetries. Their most important instances are C, the parity transformation P (where the entire space coordinate system is mirrored at the origin), and time reversal T (where the time component is reversed). Naturally, these transformations can also be combined. Applying both the C and the P transformation to a particle, one changes the sign of the charge, the momentum and the helicity of the system and ends up with a particle carrying the quantum numbers of the anti-particle to the original system. Therefore, applying the combination of the C and P transformations "creates" the corresponding anti-particle.

Symmetry under any of these transformations implies again that observables do not change. If, however, changes can be observed this is labeled a "violation of the symmetry".

One of the most basic relations in quantum field theories, as derived by Wolfgang Pauli and proved by Gerhart Lüders ([16, 17]), states that any theory fulfilling the requirements,

- locality,

- causality,

- existence of a stable vacuum state (i.e. a lower bound on the Hamiltonian), and

- invariance with respect to orthochronic Poincaré transformations,

will be invariant under the combined transformation C, P and T.

Nonetheless, each of these symmetries might be violated individually. To the extent of today's knowledge, each symmetry is conserved by the quantum field theories of electromagnetic and strong interactions as well as by gravity, which is being described by the theory of general relativity. The weak interaction, on the other hand violates each transformation: C and P maximally, and CP by about 1‰.

2.2   CP violation

The simplest interpretation of particles and anti-particles would imply that aside from the different charges there is no distinction whatsoever. In this naive picture, the decay rates and other quantities are conserved under a CP transformation. However this is not the case, there exists a violation of CP symmetry.

The first observation of this violation was based on experimental data of the decay of neutral kaons. According to the quark model, we can construct two such particles, K^0 (which is interpreted as a $d\bar{s}$ combination) and $\bar{K}^0$ ($\bar{d}s$). K^0 and $\bar{K}^0$ are eigenstates with respect to the strong interaction. In weak interaction, e.g. decays, we see linear combinations of these particles. One of the neutral kaons has a long mean lifetime, $\tau = (5.116 \pm 0.020) \times 10^{-8}s$ [18]; it is therefore labeled the "K long" (K_L). The other one, the "K short" or K_S, has a much shorter mean lifetime, $\tau = (0.8958 \pm 0.0005) \times 10^{-10}s$ [18]. The dominant decay modes of these states are $K_L \rightarrow \pi\pi\pi$ and $K_S \rightarrow \pi\pi$. These final states carry well-defined CP eigenvalues of -1 ($\pi\pi\pi$) and $+1$ ($\pi\pi$). Therefore it was originally assumed that K_L and K_S are identical to the CP eigenstates of the system of neutral kaons, labeled with K_1 and K_2. This would mean that with respect to the weak interaction K_L and K_S define the most appropriate basis, wheras for the strong interaction it is formed by K_0 and $\bar{K}_0$.

In 1964 Christensen, Cronin, Fitch and Turley showed that the decay $K_L \rightarrow \pi\pi$ exists [19], with a relative branching ratio of $\mathcal{B}(K_L \rightarrow \pi\pi)/\mathcal{B}(K_L \rightarrow \pi\pi\pi) \sim 10^{-3}$. A "branching ratio", denoted by $\mathcal{B}(X \rightarrow Y)$, gives the relative frequency of the decay of the particle X to the final state Y[1]. Cronin and Fitch were awarded the Nobel Prize in Phyics in 1980 for this discovery.

Interpreting this result might imply two possibilities. Either K_L and K_S are not exactly the CP eigenstates of the system, but simply "very close" to the

---

[1]The branching ratio can be calculated from the decay width of a process by $\mathcal{B}(X \rightarrow Y) = \Gamma(X \rightarrow Y)/\Gamma_{tot}$, where Γ_{tot} is the total decay width and $\Gamma(X \rightarrow Y)$ is the partial decay width related to the process $X \rightarrow Y$.

real eigenstates K_1 and K_2. In this case relations like

$$K_L \approx K_1 + \epsilon K_2, \tag{2.1}$$

$$K_S \approx K_2 + \epsilon K_1, \tag{2.2}$$

would hold, with $\epsilon \sim 10^{-3}$. The CP-violating decay $K_L \to \pi\pi$ could simply be due to the small admixture of the K_2 component and thus be the result of an inadequate choice of the basis. This is labeled the "indirect CP violation". Alternatively, the second possibility would be that indirect CP-violation is not enough to explain the experimental data. In this case one would actually see the CP-violating decay $K_1 \to \pi\pi$, which is labeled as "direct CP-violation".

Models like the superweak theory, which introduced a fifth fundamental force, tried to explain CP-violation in the kaon sector as a purely indirect one. Experimental results by highly specialized precision experiments, like NA48 at CERN and KTeV at Fermilab, did however prove the existence of direct CP-violation.

2.3 The origin of the universe

The most exciting implication one can draw from CP violation comes from investigating a cosmological question.

According to current cosmological models, the initial state of the universe was a dense hot state, which expanded rapidly. This is usually labeled the "Big bang". This initial state had zero net charges, and there is no evidence which would suggest an excess of either quarks or anti-quarks. Rather, it consisted purely of energy. In these extreme conditions, pairs of quarks and anti-quarks as well as pairs of leptons and anti-leptons were produced with enormous rates and immediately annihilated again into photons. When the universe cooled during the expansion and the average temperature dropped below a certain, so-called "critical" temperature T_c, the average energy was too low for continued spontaneous creation of new particles. The annihilation

of matter and anti-matter was no longer countered by pair production and all the hadrons would soon have annihilated completely again[2].

Thus, if the assumption that matter and anti-matter decay in exactly the same way would hold, the universe would only consist of the photons created in these annihilations after the big bang. Obviously, this is not the case; at least some matter still remains. In fact one finds a very small value when comparing the amount of matter with the amount of photons in the universe, however, this factor is still finite (for example, the WMAP satellite experiment found that the density of photons in the cosmic microwave background exceeds the density of baryons by a factor of about 10^{10}). For the big picture of the evolution of the universe to be consistent, we therefore have to be able to explain an excess of baryons over anti-baryons.

In 1966, the russian physicist Andrei Sakharov stated three criteria for the occurrence of "Baryogensis", that is the development of some excess of matter over anti-matter in the course of the expansion of the universe. These criteria are that

- the universe must not be in a thermal equilibrium,

- the conservation of baryon number must be violated and can at best be only be an approximate conservation and

- both C and CP symmetries must be violated.

Each of these criteria poses a fascinating question and topic in modern physics. The mechanism of CP-violation can be directly probed in laboratory conditions, for example in particle collider experiments.

---

[2]The same is true of leptons, where the critical temperature is lower than for hadrons.

2.4   The Cabibbo-Kobayashi-Maskawa (CKM) mechanism

The experiment by Christensen, Cronin, Fitch and Turlay showed the existence of CP violation in nature. The Sakharov conditions stress the importance of this result in terms of the big picture of the evolution of the universe itself. However, within the framework of particle physics the question is, whether one can understand the existence of CP violation within the current theories. If one has to add further theoretical assumptions, there have to be testable predictions, which can be compared with experimental data.

The Standard Model of particle physics, as it presented itself during the 1960s when CP violation was found, did not incorporate any CP violation. At this time only 3 quarks were known (the u, d and s quarks). In 1970, the charm quark (c) was predicted by the GIM-mechanism [20], however even the Standard model describing four quark kinds did not contain CP violation.

In 1973, Kobayashi Makoto and Toshihide Maskawa developed ideas by Nicola Cabibbo further, in order to give a formalism to CP-violation within a specifically enhanced Standard Model [3]. Cabibbo had introduced the concept of "weak mixing" in order to explain strange quark decays into up quarks [21]. The mass eigenstates of the quarks are not identical to the weak interaction eigenstates, a fact which has already been mentioned above in the discussion of neutral kaons. Cabibbo theorized that this behavior can be interpreted in terms of a rotation, such that one can write the weak eigenstates as e.g.

$$\begin{pmatrix} u_w \\ d_w \end{pmatrix} = \begin{pmatrix} u_m \\ d_m \cos\theta_c + s_m \sin\theta_c \end{pmatrix}, \qquad (2.3)$$

where x_w and x_m denote the eigenstates of the weak interactions and the mass eigenstates, respectively. θ_c is the so-called Cabibbo angle. This idea was also the basis of the GIM-mechanism [20], adding

$$\begin{pmatrix} c_w \\ s_w \end{pmatrix} = \begin{pmatrix} c_m \\ s_m \cos\theta_c - d_m \sin\theta_c \end{pmatrix}. \qquad (2.4)$$

In their paper [3], Kobayashi and Maskawa discuss various approaches how to describe CP-violation in a framework containing four quarks, but finally conclude that the only solution is to consider the existence of a total of six quark types, grouped in three generations. In such a framework, the weak mixing can be interpreted as the rotation related to a three-times-three unitary matrix, which is called the Cabibbo-Kobayashi-Maskawa (CKM) matrix. The postulated new quarks, called the "bottom" or "beauty" quark b and the "top" or "truth" quark t, have been found experimentally in 1977 and 1995, respectively.

Starting from the assumption by Kobayashi and Maskawa, one can write the charge current interaction in the Lagrangian of the theory as,

$$- \mathcal{L}_{W^{\pm}} = \frac{g}{\sqrt{2}} \, \bar{u}_{Li} \, V_{ij} \, d_{Rj} \, W_{\mu}^{+} + h.c. \tag{2.5}$$

Up-type quarks u are coupled to down-type quarks d and the W boson. However, there is no constraint that such couplings can only occur within one generation. The CKM matrix elements V_{ij} mix the three generations. The matrix can be written in the widely used Wolfenstein parametrization ([22]) as

$$V = \begin{pmatrix} V_{ud} & V_{us} & V_{ub} \\ V_{cd} & V_{cs} & V_{cb} \\ V_{td} & V_{ts} & V_{tb} \end{pmatrix} \approx \begin{pmatrix} 1 - \frac{\lambda^2}{2} & \lambda & A\lambda^3(\rho - i\eta) \\ -\lambda & 1 - \frac{\lambda^2}{2} & A\lambda^2 \\ A\lambda^3(1 - \rho - i\eta) & A\lambda^2 & 1 \end{pmatrix}, \tag{2.6}$$

where λ, ρ and η are the Wolfenstein parameters, and $\lambda \approx 0.2$ corresponds to $\sin\theta_c$. While this parametrization is only an approximation, it allows to estimate the size of the CKM matrix elements. The modulus of each of the diagonal elements is close to 1, so the coupling between quarks of the same generation will dominate. However, the couplings to the other generations are not zero, they are simply very small. An exact representation of this complex matrix is to use three Euler angles, which can describe any rotation, and one

complex phase: [23]

$$
V = \begin{pmatrix} 1 & 0 & 0 \\ 0 & c_y & s_y \\ 0 & -s_y & c_y \end{pmatrix} \begin{pmatrix} c_z & 0 & s_z e^{-i\phi} \\ 0 & 1 & 0 \\ -s_z e^{-i\phi} & 0 & c_z \end{pmatrix} \begin{pmatrix} c_y & s_y & 0 \\ -s_y & c_y & 0 \\ 0 & 0 & 1 \end{pmatrix} =
$$
$$
= \begin{pmatrix} c_x c_z & s_x c_z & s_z e^{-i\phi} \\ -s_x c_y - c_x s_y s_z e^{i\phi} & c_x c_y - s_x s_y s_z e^{i\phi} & s_y c_z \\ s_x s_y - c_x c_y s_z e^{i\phi} & -c_x s_y - s_x c_y s_z e^{i\phi} & c_y c_z \end{pmatrix}, \tag{2.7}
$$

where $c_a \equiv \cos\theta_a$ and $s_a \equiv \sin\theta_a$. The complex phase is the only source of CP-violation within the Kobayashi-Maskawa theory.

The extension of Eq. 2.3 and 2.4 is the defintion of the weak eigenstates by an rotation of the mass eigenstates,

$$
\begin{pmatrix} d_w \\ s_w \\ b_w \end{pmatrix} = \begin{pmatrix} V_{ud} & V_{us} & V_{ub} \\ V_{cd} & V_{cs} & V_{cb} \\ V_{td} & V_{ts} & V_{tb} \end{pmatrix} \begin{pmatrix} d_m \\ s_m \\ b_m \end{pmatrix}, \tag{2.8}
$$

where x_w denotes a weak eigenstate and x_m a mass eigenstate. With the cosine terms in Eq. 2.7 being close to unity and the sine terms being $\mathcal{O}(0.1)$ or smaller, Eq. 2.3 and 2.4 are excellent approximations for the first two weak eigenstates.

Since V_{ij} describes a rotation, it has to be unitary,

$$
V \times V^+ = \mathbb{1}_{3\times3}; \quad \sum_i V_{ij} V_{jk}^+ = \delta_{ik}, \, \forall i,k \tag{2.9}
$$

where $\mathbb{1}_{3\times3}$ is the three-times-three unit matrix, and δ_{ij} is the Kronecker delta. From these relations one can therefore infer equations which have to be satisfied if the theory of Kobayashi and Maskawa is correct. One of those is

$$
V_{ub}^* V_{ud} + V_{cb}^* V_{cd} + V_{tb}^* V_{td} = 0. \tag{2.10}
$$

Interpreted geometrically, as shown in Fig. 2.1, these relations are labeled the "unitary triangles", and testing them is the main aim of the precision experiments Belle at KEK (Tsukuba, Japan), and BaBar at SLAC (Stanford,
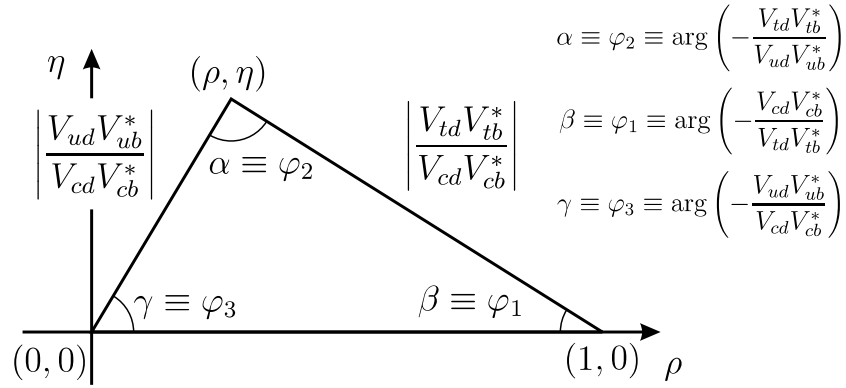
Figure 2.1: The unitary triangle which is related to the equation $V_{ub}^* V_{ud} + V_{cb}^* V_{cd} + V_{tb}^* V_{td} = 0$. The basis of the triangle has been normalized to 1. There exist two nomenclatures for the angles, both of which are indicated in the figure.

USA). The sides and angles of this triangle can be measured independently from each other. If the theory of Kobayashi and Maskawa were wrong, then these different measurements would report incompatible results.

Fig. 2.2 shows the combination of all currently available measurements of parts of the unitary triangle [24]. There is one region which is compatible with all these results and, even more, it is exactly one region, so there is no ambiguity in the interpretation. The conclusion from these results is that the theory of Kobayashi and Maskawa describes the phenomena of CP-violation which have been found up until now. Possible deviations from the predictions of the theory are of the order of 10%. Because of this conclusion, Kobayashi and Maskawa were awarded half the Nobel prize in physics in 2008.

2.5   Semileptonic b decays

Decays of the kind $b \to cW^-$, $W^- \to \ell^- \bar{\nu}$ are excellent probes to determine the value of the modulus of V_{cb}, $|V_{cb}|$. This value contributes to the length of the basis of the unitary triangle or, if one normalizes that to 1, to the lengths of the other two legs of the triangle, as shown in Fig. 2.1. Measuring it with high precision is therefore of utmost importance.
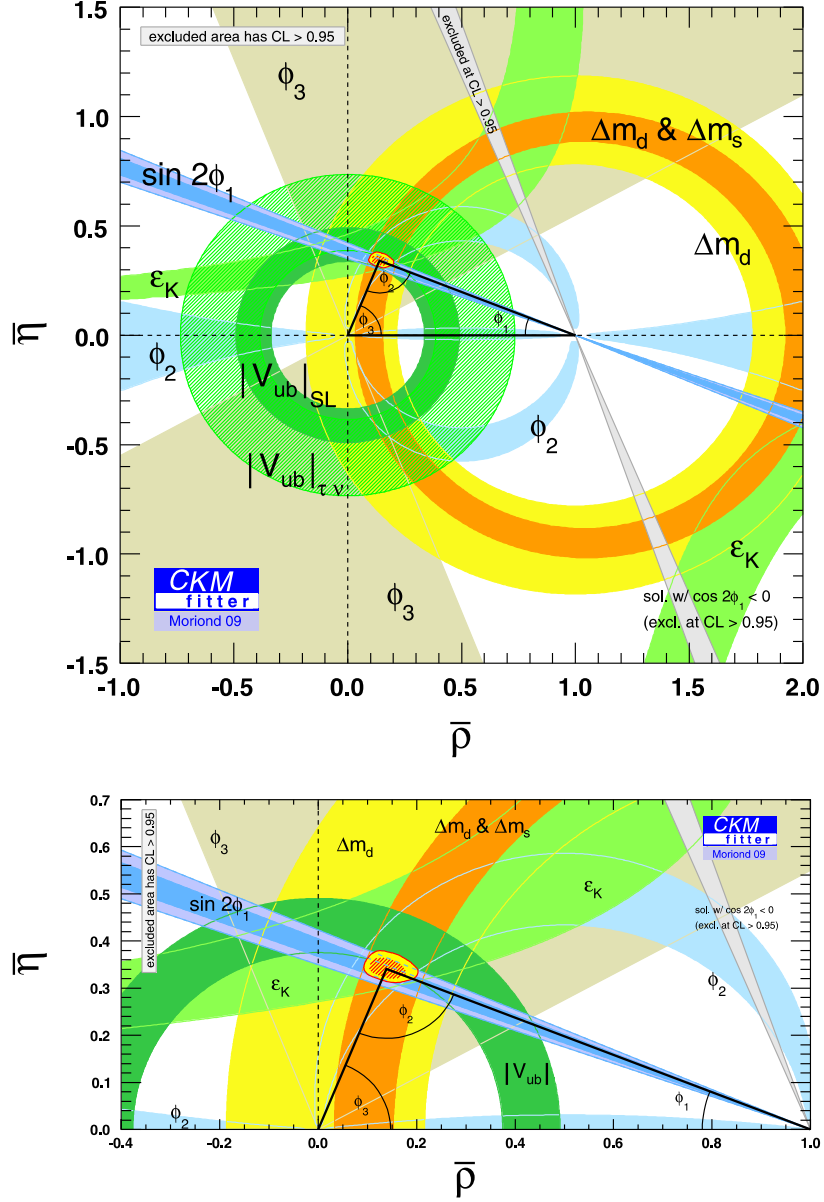
Figure 2.2:   Comparison of various measurements of the unitary triangle, compiled by the CKMfitter group [24]. The tip of the shown triangle (solid black) gives the average of of all the measurements, the red shaded area depicts the one sigma range of this average. The other colored areas give the results one can infer from single measurements.
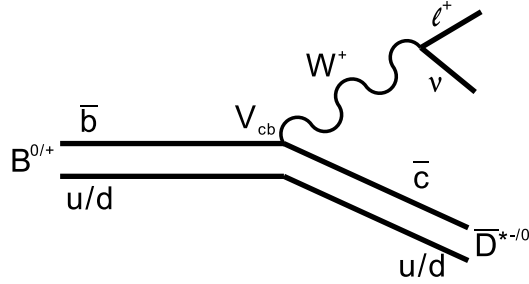
Figure 2.3: Quark-level Feynman diagram for the decays $B^0 \to D^{*-}\ell^+\nu$ and $B^+ \to \bar{D}^{*0}\ell^+\nu$.

These decays are dominated by tree level contributions, which are shown in Fig. 2.3 for the transitions $B^0 \to D^{*-}\ell^+\nu$ and $B^+ \to \bar{D}^{*0}\ell^+\nu$[3]. As given in Eq. 2.5, the Lagrangian of the interaction between b and c is linear in the CKM matrix elements V_{cb}. On tree level, the probability of this process to occur is proportional to $|V_{cb}|^2$. Determining the total number of B mesons produced and the number of $B \to D^*\ell^+\nu$ decays observed would in principle be sufficient to determine a value of $|V_{cb}|$. As will be discussed in Chapter 3 the situation is more complicated due to QCD effects.

Two approaches of measurements of $|V_{cb}|$ based on semileptonic decays exist. Either one does not specifically search for one specific meson containing a c meson created in $b \to c\ell\nu$ decays. Rather, only the lepton is searched for and investigated. This is the so-called "inclusive" ansatz. In the "exclusive" approach, the charm meson is also reconstructed and analyzed. The work presented here concentrated on exclusive analyses.

2.6   Open questions

While the overall success of the CKM-mechanism is stunning, both on the theoretical and the experimental side, CP-violation cannot yet be considered as being completely investigated.

The major question with respect to the evolution of the universe can defi-

---

[3]Charge conjugation is implied throughout this work.

nitely not be answered on basis of the CP-violation explained by the CKM
mechanism alone. The currently known processes would only allow for a ra-
tio of baryon density to photon density of $\frac{n_B}{n_\gamma} \sim 10^{-20}$. As mentioned above,
the WMAP exeriment reported $\frac{n_B}{n_\gamma} = (5.1^{+0.3}_{-0.2}) \times 10^{-10}$, which amounts to a
deviation by a factor of 10^{10}.

Also, while the accuracy of the experimental measurements in the CKM
sector is very high, experimental questions remain.

For example, various measurements of $|V_{cb}|$ are available, but do not show
perfect agreement with each other. The inclusive and exclusive approaches
to extract $|V_{cb}|$ yield results which differ by about 2.5 standard deviations,
meaning that this can barely be explained by a statistical fluctuation [10].
Also within the exclusive analyses, the results barely agree with each other.
One possible explanation would be a misrepresentation of some systematic
uncertainty.

These facts imply that an improved measurement, which is even more accu-
rate than the already existing ones, can yield important results.

Chapter 3

Heavy quark effective theory

A designer knows he has achieved perfection not when there is nothing left to add, but when there is nothing left to take away.

Antoine de Saint-Exupry

As described above, the investigation of the weak decay of b quarks is a powerful tool to investigate fundamental parameters of the Standard model, the CKM matrix elements. This work centers on the analysis of the decay $b \to cW^-$, which yields the parameter $|V_{cb}|$. Due to the effect of confinement present in QCD we cannot investigate free quarks, but only bound states like baryons or mesons. In the decay of these particles, the weak interaction, like it is described by the Kobayashi-Maskawa mechanism, is not a priori separated from the effects of strong interaction between the quarks. It is therefore imperative to correctly consider the implications of QCD in order to be able to derive $|V_{cb}|$. In the system of a B meson, which consists of a $\bar{b}$ anti-quark and either an u or a d quark[1], the most powerful ansatz to do so is to use an effective theory, specifically tailored for the needs of this question, the so-called Heavy Quark Effective Theory (HQET).

---

[1] Throughout this work, charge conjugated states are implicitly considered as well.

3.1   General idea

The presentation of the theoretical framework given here will not concentrate on the intricate technical problems associated with the derivation of the formalism, but will rather focus on the broad implications. More detailed information can be found in various reviews of this topic, like Ref. [4, 25].

The main idea is a series of steps as follows: In the system of a B meson, we find a rather heavy constituent (the $\bar{b}$ anti-quark) and a light one (the u or d quark). The situation thus is not entirely unlike the hydrogen atom. There the first ansatz is to assume an infinite mass of the nucleus and consider only the degrees of freedom associated with the electron. Similarly, if we let $m_b \to \infty$, all dependency on the flavor of the heavy quark vanishes and many results are invariant under flavor transition. Thus a new symmetry arises in this approximation, which is called the "Heavy quark symmetry". The change of the flavor of the heavy quark is exactly the feature of a weak decay of the B meson. In order to derive more accurate relations, this naive ansatz can be enhanced by considering a Taylor expansion of the full theory in $1/m_b$ and investigating more than just the leading term.

All effects due to QCD are considered in terms of so-called form factors, which are one-dimensional functions. The shape of these functions is not fixed by HQET, in principle a huge set of functions might be possible. Therefore this formulation is not sufficient for use in an experimental procedure, one first has to limit the number of variables to a finite set. This is done by considering a set of dispersion relations.

3.2   Heavy quark symmetry

As in all quantum field theories, the coupling constant of QCD depends on the momentum transfer Q^2 between the interacting particles. The effective coupling constant can be parametrized as

$$\alpha_s(Q^2) = \frac{g_{eff}^2(Q^2)}{4\pi} = \frac{12\pi}{(33 - 2n_f)\ln\left(Q^2/\Lambda_{QCD}^2\right)}. \tag{3.1}$$

n_f gives the number of generations of fundamental fermions (*i.e.* quarks), in the theory. According to the theory of Kobayashi and Maskawa as well as various experimental investigations this number equals 3. The factor of $(33 - 2n_f)$ in the denominator is due to the non-Abelian structure of $SU(3)$, the color gauge group of QCD. Unlike the photon, the gluons carry charge and therefore couple to themselves in loops. This is also the reason for the fundamental difference in the behavior of the coupling constants of Quantum Electrodynamics and QCD. While the former rises with rising momentum transfer, α_s becomes smaller (as long as $n_f < 33/2$).

This unique feature of QCD is called asymptotic freedom [26, 27]. In the domain of high momentum transfer the strong interaction is perturbative and can be probed very similar to the electromagnetic interaction. For small Q^2 on the other hand the coupling constant becomes large and a perturbative approach is no longer feasible. This fundamental difference in behavior defines the scale associated with perturbative QCD, Λ_{QCD}.

The typical size of hadrons is usually given as $R_{\text{had}} \sim 1/\Lambda_{\text{QCD}} \sim 1\text{fm}$, thus $\Lambda_{\text{QCD}} \approx 0.2\text{GeV}^2$. A quark with mass far above this scale, $m_Q \gg \Lambda_{\text{QCD}}$, is labeled a heavy quark. Using this diction, the quarks of the Standard Model (SM) are divided into two classes, the heavy quarks (c, b, and t) and the light ones (u, d and s). Between heavy quarks the effective coupling α_s is small, since the Compton wavelength

$$\lambda_Q \sim 1/m_Q \tag{3.2}$$

is small as well.

For systems composed of both heavy and light constituents this is not the case. Since the size of e.g. B mesons is again roughly R_{had}, the momenta exchanged within such a system are typically of the order Λ_{QCD} and thus large with respect to the light quarks. The configuration of the light constituents interacting with the heavy quarks is therefore not trivial, but rather a complicated ensemble of light quarks and gluons which is sometimes labeled as the "brown muck" [28].

---

[2]The use of natural units, $c = \hbar = 1$, is implied.

However, with respect to the heavy quark, the picture can be simplified. With its Compton wavelength being much smaller than R_{had}, a hard probe with at least $Q^2 \sim m_Q^2$ would be needed to give rise to a sizable interaction. The light quarks are therefore predominantly influenced by the color field. In the rest frame of the heavy quark it is actually only the color-electric field, which leads to an interaction with the light constituents. In the limit $m_Q \to \infty$, systems with different flavor of the heavy quark can still be described by the same system of light degrees of freedom. This is the so-called "heavy quark symmetry" [28].

3.3   Effective theory for $m_Q \to \infty$

The section above contained some qualitative statements on the behavior of heavy quarks. In order to be able to derive more general implications the derivation of an effective Lagrangian is needed. For $m_Q \to \infty$ we essentially find the leading term of a Taylor expansion of the full Feynman rules of QCD.

As written above, within a hadron the momenta exchanged between a heavy quark Q and light constituents are much smaller than it's mass m_Q. Due to the large difference in mass, it is a good approximation to equal the velocity of the heavy quark with that of the hadron,

$$\vec{v}_Q \approx \vec{v}_{had}.$$

The momentum can be given as

$$p_Q^\mu = m_Q v^\mu + k^\mu, \tag{3.3}$$

where the "residual momentum" k^μ is of the order Λ_{QCD} and small compared to $m_Q v^\mu$. v^μ is the four-velocity of the hadron, satisfying $v^\mu v_\mu = v^2 = 1$. Let us now consider the case of a very heavy quark by considering the limit $m_Q \to \infty$, with v and k fixed. This simplifies the Feynman rules of the system.

The heavy quark propagator can be written as [4, 28]

$$\frac{i}{\not{p}_Q - m_Q} = \frac{i}{v \cdot k} \frac{\not{v} + 1}{2} + \underbrace{\mathcal{O}(1/m_Q)}_{\to 0}.$$ (3.4)

In the limit $m_Q \to \infty$, only one part remains. Similarly, the vertex rule of the full theory, $igT_a\gamma^\mu$, becomes [4, 28]

$$igT_a\gamma^\mu \to igT_a v^\mu + \underbrace{\mathcal{O}(1/m_{q^H})}_{\to 0}.$$ (3.5)

As usual in quantum field theories, these rules have to be obtainable as the derivative of a Lagrangian. The expression [4, 28]

$$\mathcal{L}_{eff} = \bar{H}_v iv D H_v = \bar{H}_v (iv^\mu \partial_\mu + gT_a v^\mu A_\mu^a) H_v,$$ (3.6)

fulfills this requirement, where D is the covariant derivative and the effective heavy quark field $H_v(x)$ is defined as the approximation [29]

$$Q(x) \approx e^{-im_Q \, v \cdot x} H_v(x).$$ (3.7)

The heavy quark field $H_v(x)$ is constrained to satisfy

$$\not{v} H_v(x) = H_v(x).$$ (3.8)

Eq. 3.6 gives the Lagrangian of the HQET under the condition $m_Q \to \infty$ [28, 29, 30].

It is an approximation of the full Lagrangian of QCD and does not yet include any corrections due to finite quark mass. Detailed discussions have been the topic of several reviews over the last decades [4, 25].

3.4   Weak decays of infinitely heavy mesons

This mass independent setup can already be used to investigate some of the properties of the weak decay of heavy mesons [28]. Let $\{|M(v)\rangle\}$ be the set of meson states, each containing one heavy quark Q and one light one q. v denotes the mesons four-velocity and therefore fulfills $v_\mu v^\mu = 1$. These states are normalized according to

$$\langle M(\tilde{v})|M(v)\rangle = 2v^0, (2\pi)^3 \delta^3(\vec{p} - \vec{\tilde{p}}), \tag{3.9}$$

which is a mass independent normalization prescription. When considering the limit $m_Q \to \infty$, the heavy degrees of freedom vanish and the light degrees of freedom characterize any state $|M(v)\rangle$ completely.

Elastic scattering of a pseudo scalar meson, $P(v) \to P(\tilde{v})$ at a time t_0, can be described as follows. For $t < t_0$, the light degrees of freedom define the initial state, which is some configuration around a heavy color source moving with velocity v. The mean velocity of the light constituents will be equal to this quantity, $\langle v_l \rangle = v$. The elastic scattering at $t = t_0$ is induced by an external vector current coupled to the heavy quark. Effectively, this scattering instantaneously replaces the color source $H(v)$ with one moving with a different velocity, $H(\tilde{v})$. This however means that at $t = t_0 + \epsilon$ the light constituents are traveling in the color field of a source which is boosted relative to their rest frame. This leads to the exchange of soft gluons, which rearrange the light degrees of freedom such that a final state meson moving with velocity $\tilde{v}$ appears. For $v = \tilde{v}$ the frames naturally coincide and there is no change at all, for all other velocities one finds a form factor suppression. In the limit $m_Q \to \infty$, this form factor is the so-called "Isgur-Wise function" and depends only on the Lorentz boost $\gamma = v_\mu \tilde{v}^\mu$. It also governs the weak decay of mesons in the limit $m_Q \to \infty$, as can be derived as follows [28].

Let us denote a pseudoscalar meson moving with a velocity v and containing a heavy quark Q with P and one moving with velocity $\tilde{v}$ containing a different heavy quark $\tilde{Q}$ with $\tilde{P}$. The heavy quark fields, as defined in Eq. 3.7, are denoted by H_v and $\tilde{H}_{\tilde{v}}$ respectively.

The heavy meson-heavy meson transition element $\langle \tilde{P} | \tilde{H}_{\tilde{v}} \gamma_\mu H_v | P \rangle$ is of the general form [28]

$$\langle \tilde{P}(\tilde{v}) | \tilde{H}_{\tilde{v}} \gamma_\mu H_v | P(v) \rangle = f_+(v_\nu \tilde{v}^\nu) \left[v + \tilde{v} \right]_\mu + f_-(v_\nu \tilde{v}^\nu) \left[v - \tilde{v} \right]_\mu. \qquad (3.10)$$

The functions $f_\pm$ depend on the product of the meson four-velocities and are the form factors associated with the decay.

The light degrees of freedom of the initial quark carry momenta of the order $v\Lambda_{QCD}$, those of the final quark momenta of the order $\tilde{v}\Lambda_{QCD}$. The squared invariant momentum transfer experienced by the light degrees of freedom is therefore of the order

$$q^2 \approx \Lambda_{QCD}^2 (v_\mu \tilde{v}^\mu - 1), \qquad (3.11)$$

which is small compared to the heavy quark mass as long as $v_\mu \tilde{v}^\mu$ is of the order of unity.

In Eq. 3.8 we constrained the heavy quark field to fulfill $\not{p} H_v(x) = H_v(x)$, $\bar{H} \not{p} = \bar{H}_v(x)$, where $\not{p} = \gamma_\mu p^\mu$. If we contract both sides of Eq. 3.10 with $(v - \tilde{v})^\mu$ we find

$$\langle \tilde{P}(\tilde{v}) | \tilde{H}_{\tilde{v}} H_v - \tilde{H}_{\tilde{v}} H_v | P(v) \rangle = 0 =$$
$$= f_+ \left[v + \tilde{v} \right]_\mu \left[v - \tilde{v} \right]^\mu + f_- \left[v - \tilde{v} \right]_\mu \left[v - \tilde{v} \right]^\mu,$$
$$= f_+ \underbrace{\left[1 + \tilde{v}_\mu v^\mu - v_\mu \tilde{v}^\mu - 1 \right]}_{=0} + f_- \underbrace{\left[1 - \tilde{v}_\mu v^\mu - v_\mu \tilde{v}^\mu + 1 \right]}_{\neq 0}, \quad (3.12)$$

where we used $v_\mu v^\mu = \tilde{v}_\mu \tilde{v}^\mu = 1$ and therefore

$$f_- = 0. \qquad (3.13)$$

For $v = \tilde{v}$ and thus $v_\mu \tilde{v}^\mu = 1$, Eq. 3.10 gives the matrix element of a conserved current associated with heavy quark symmetry, with the $\mu = 0$ component being related to a generator of the symmetry. From this one obtains the normalization [31, 32, 33, 34],

$$f_+(1) = 1. \qquad (3.14)$$

The interpretation of this normalization is simply that in case of equal velocity in the initial and the final state, the light constituents do not experience any change in the color field and are therefore unchanged. This kinematic point is labeled as "zero recoil", since the rest frames of the two mesons coincide. As one can see, only one single form factor governs the transition $P \to \tilde{P}$. It is often labeled the Isgur-Wise function and denoted with ξ in the literature.

3.5 Differential decay widths for finite quark mass

If one is interested in the transition between heavy mesons where also a spin flip occurs, the picture becomes more complicated. Of particular interest is the decay of a pseudoscalar meson P into a vector meson V and a W boson. Here, the W couples to the difference of vector and axial vector currents, $V - A$. There is currently no theoretical argument which allows to derive this particular behavior, however no experimental evidence of a deviation has been found up until now. In this case one has to investigate two matrix elements here, $\langle V(\tilde{v}, \epsilon)|\tilde{H}_{\tilde{v}}\gamma_\mu H_v|P(v)\rangle$ and $\langle V(\tilde{v}, \epsilon)|\tilde{H}_{\tilde{v}}\gamma_\mu\gamma_5 H_v|P(v)\rangle$, where ϵ is the polarization vector for V and $\gamma_5 = \gamma_1\gamma_2\gamma_3\gamma_4$.

Considering the effective three-body decay $P \to V\ell\nu$, the hadronic current has the general form ([4, 25, 35]),

$$\langle V(p_V, \epsilon)|V^\mu - A|P(p_P)\rangle = \frac{2i\epsilon^{\mu\nu\alpha\beta}}{m_P + m_V}\epsilon^*_\nu(p_V)_\alpha(p_P)_\beta V(q^2)$$
$$- (m_P + m_V)\epsilon^{*\mu}A_1(q^2) + \frac{\epsilon^* \cdot q}{m_P + m_V}(p_P + p_V)^\mu A_2(q^2)$$
$$+ 2m_V\frac{\epsilon^* \cdot q}{q^2}q^\mu A_3(q^2) - 2m_V\frac{\epsilon^* \cdot q}{q^2}q^\mu A_0(q^2), \tag{3.15}$$

where $q^\mu = p_P^\mu - p_V^\mu$, $A_3(q^2) = \frac{m_P+m_V}{2m_V}A_1(q^2) - \frac{m_P-m_V}{2m_V}A_2(q^2)$ and $A_0(0) = A_3(0)$. Each term is linear in the polarization vector ϵ. In case of ℓ being a light charged lepton, either an electron or a muon, terms proportional to q^μ are nearly negligible. For $m_\ell \to 0$, therefore three form factors completely

describe the process $P \to V\ell\nu$,

$$\lim_{m_\ell \to 0} \langle V(p_V, \epsilon)|V^\mu - A|P(p)\rangle \approx \frac{2i\epsilon^{\mu\nu\alpha\beta}}{m_P + m_V}\epsilon^*_\nu(p_V)_\alpha(p_P)_\beta V(q^2)$$
$$- (m_P + m_V)\epsilon^{*\mu}A_1(q^2) + \frac{\epsilon^* \cdot q}{m_P + m_V}(p_P + p_V)^\mu A_2(q^2). \quad (3.16)$$

$A_1(q^2)$ and $A_2(q^2)$ can be associated with the exchange of a particle with quantum numbers $J^P = 1^+$ and $V(q^2)$ with $J^P = 1^-$.

If one additionally considers the consecutive decay of V into two pseudo scalars, $V \to P_1 P_2$, a set of four independent kinematic variables describes the kinematics of the decay. One is the momentum transfer q^2, which equals the mass of the virtual W meson mediating the semileptonic decay of the meson P. Often a function of q^2 is used,

$$w = \frac{m_P + m_V - q^2}{2m_P m_V} = \frac{p_P \cdot p_V}{m_P m_V}, \ \frac{\mathrm{d}w}{\mathrm{d}q^2} = -\frac{1}{2m_P m_V}, \qquad (3.17)$$

where p_P and p_V are the four-momenta of the P and V mesons. In the rest frame of the P meson, this expression simplifies and becomes $w = E_V/m_V = \gamma_V$. This is simply the Lorentz boost between the P and the V rest frames.

Additionally, a set of three angles as shown in Fig. 3.1 is used, $\{\theta_\ell, \theta_V, \chi\}$. θ_ℓ is measured in the rest frame of the W boson, it is the polar angle between the charged lepton ℓ and the direction opposite to the spatial momentum of the vector meson V. Similarly, θ_V is defined in the V rest frame. It gives the polar angle between the meson P_1 and the direction opposite to the W boson. Whether P_1 or P_2 are chosen is arbitrary, as long as one ignores the last variable, χ. As sketched in Fig. 3.1, this parameter gives the angle between the plane defined by the decay of the W boson and the plane defined by the decay of the V meson. The orientation of the planes has to be defined consistently with the choice of whether P_1 or P_2 are used to define θ_V to ensure the correct calculation of the sign of χ.

In our particular case, the initial meson P is a B meson, V is a D^*, P_1 a D^0 and P_2 a π. Fig. 3.1 shows this nomenclature.

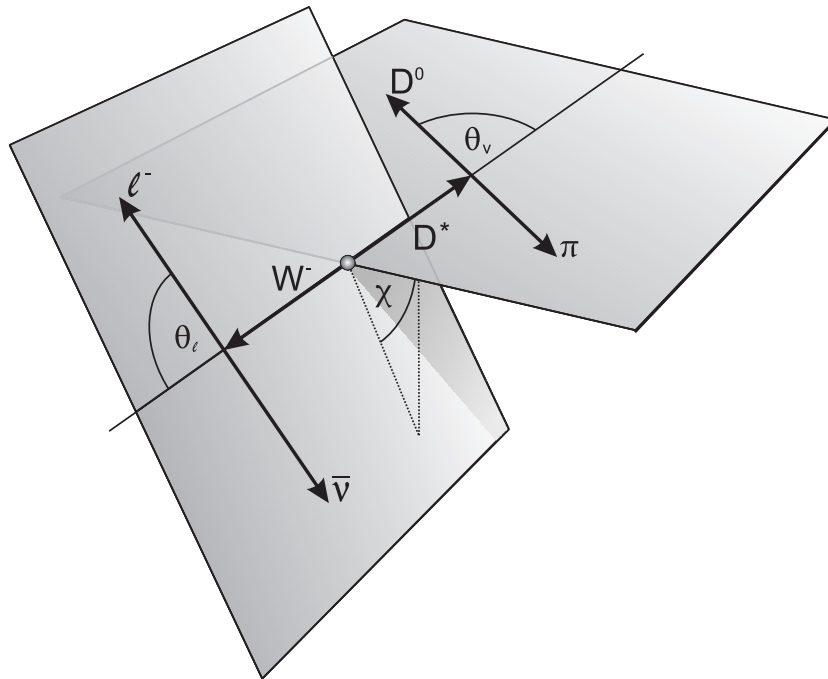In order to simplify the physical interpretation of the hadronic current shown

Figure 3.1: Definition of the angles θ_ℓ, θ_V and χ. It is equally valid for both the decays $B^0 \to D^{*-}\ell^+\nu_\ell$, $D^{*-} \to \bar{D}^0\pi_s^-$ and $B^- \to \bar{D}^{*0}\ell^+\nu_\ell$, $\bar{D}^{*0} \to \bar{D}^0\pi_s^0$.

in Eq. 3.16, it is sometimes advisable to define the so-called helicity ampli-
tudes H_0, H_+ and H_-. In this interpretation, one separates the matrix ele-
ment in components associated with a helicity of 0, +1 or -1 of the V and
the W, respectively. The equations, which relate the axial-vector and vector
form factors to the helicity amplitudes are [25]

$$H_0(q^2) = \frac{(m_P^2 - m_V^2 - q^2)(m_P + m_V)}{2m_V \sqrt{q^2}} A_1(q^2) - 4\frac{m_P^2 p_V^2}{2m_V \sqrt{q^2}(m_P + m_V)} A_2(q^2),$$
(3.18)

and

$$H_\pm(q^2) = (m_P + m_V) A_1(q^2) \mp \frac{2m_P m_V}{m_P + m_V} V(q^2).$$
(3.19)

With these definitions, the differential decay rate can be expressed as a func-
tion of the helicity amplitudes ([25], [36], [37]),

$$\frac{\mathrm{d}^4\Gamma(P \to V\ell\nu, V \to P_1 P_2)}{\mathrm{d}q^2 \mathrm{d}\cos\theta_V \mathrm{d}\cos\theta_\ell \mathrm{d}\chi} = \frac{3}{8(4\pi)^4} G_F^2 |V_{q'Q}|^2 \frac{p_V q^2}{m_P^2} \mathcal{B}(V \to P_1 P_2)$$

$$\times \Big\{ (1 - \eta\cos\theta_\ell)^2 \sin^2\theta_V |H_+(q^2)|^2 +$$

$$+ (1 + \eta\cos\theta_\ell)^2 \sin^2\theta_V |H_-(q^2)|^2 +$$

$$+ 4\sin^2\theta_\ell \cos^2\theta_V |H_0(q^2)|^2 -$$

$$- 4\eta\sin\theta_\ell(1 - \eta\sin\theta_\ell)\sin\theta_V \cos\theta_V \cos\chi H_+(q^2)H_0(q^2) +$$

$$+ 4\eta\sin\theta_\ell(1 + \eta\sin\theta_\ell)\sin\theta_V \cos\theta_V \cos\chi H_-(q^2)H_0(q^2) -$$

$$- 2\sin^2\theta_\ell \sin^2\theta_V \cos 2\chi H_+(q^2)H_-(q^2) \Big\},$$
(3.20)

where p_V is the magnitude of the three-momentum of V in the rest frame of
P and $\mathcal{B}(V \to P_1 P_2)$ gives the branching ratio of the decay $V \to P_1 P_2$.

Within the framework of HQET, one usually gives all equations in terms of
one form factor $h_{A_1}(w)$ and two form factor ratios $R_1(w)$ and $R_2(w)$, which
are defined as,

$$V(w) = \frac{R_1(w)}{R^{*2}} \frac{2}{w+1} A_1(w) ,$$
(3.21)

$$A_2(w) = \frac{R_2(w)}{R^{*2}} \frac{2}{w+1} A_1(w) .$$
(3.22)

The function $h_{A_1}(w)$ is defined as

$$h_{A_1}(w) = \frac{1}{R^*}\frac{2}{w+1}A_1(w) \ . \tag{3.23}$$

Using these nomenclatures, the helicity amplitudes become ([1, 2, 9]),

$$H_i(w) = m_B\frac{R^*(1-r^2)(w+1)}{2\sqrt{1-2wr+r^2}}h_{A_1}(w)\tilde{H}_i(w) \ , \tag{3.24}$$

where

$$\tilde{H}_{\mp} = \frac{\sqrt{1-2wr+r^2}\left(1\pm\sqrt{\frac{w-1}{w+1}}R_1(w)\right)}{1-r} \ , \tag{3.25}$$

$$\tilde{H}_0 = 1 + \frac{(w-1)(1-R_2(w))}{1-r} \ , \tag{3.26}$$

with $R^* = (2\sqrt{m_P m_V})/(m_V + m_V)$ and $r = m_V/m_P$.

Eq. 3.20 then becomes [25]

$$\frac{\mathrm{d}^4\Gamma(P \to V\ell^+\nu_\ell)}{\mathrm{d}w\mathrm{d}(\cos\theta_\ell)\mathrm{d}(\cos\theta_V)\mathrm{d}\chi} = \frac{6m_P m_V^2}{8(4\pi)^4}\sqrt{w^2-1}(1-2wr+r^2)G_F^2|V_{cb}|^2 \times$$

$$\times \Big\{(1-\cos\theta_\ell)^2\sin^2\theta_V H_+^2(w) + (1+\cos\theta_\ell)^2\sin^2\theta_V H_-^2(w)$$

$$+ 4\sin^2\theta_\ell\cos^2\theta_V H_0^2(w) - 2\sin^2\theta_\ell\sin^2\theta_V\cos 2\chi H_+(w)H_-(w)$$

$$- 4\sin\theta_\ell(1-\cos\theta_\ell)\sin\theta_V\cos\theta_V\cos\chi H_+(w)H_0(w)$$

$$+ 4\sin\theta_\ell(1+\cos\theta_\ell)\sin\theta_V\cos\theta_V\cos\chi H_-(w)H_0(w)\Big\}. \tag{3.27}$$

G_F is the fermi constant, $G_F = (1.16637 \pm 0.00001) \times 10^{-5}\mathrm{GeV}^{-2}$ [18].

The angular distributions are a direct result of the kinematics of the decay [25]. For example, in case both the V and the W carry helicity $+1$, the angular distribution of the charged lepton emitted in the W decay is proportional to the Wigner d-function,

$$d^1_{\lambda_W,\lambda_\ell-\lambda_\nu}(\theta_\ell) = d^1_{1,-1}(\theta_\ell) = \frac{1-\cos\theta_\ell}{2}. \tag{3.28}$$

and the angular distribution of the P_1 meson in the V rest frame is given by

$$d^1_{\lambda_V,\lambda_{P_1}-\lambda_{P_2}}(\theta_V) = d^1_{1,0}(\theta_V) = -\frac{\sin\theta_V}{\sqrt{2}}. \qquad (3.29)$$

The two equations 3.28 and 3.29 explain the θ_ℓ and θ_V dependency of the term proportional to $|H_+(w)|^2$ in Eq. 3.27.

The one-dimensional differential decay rate as a function of w can be obtained from Eq. 3.27 by integration over the angular variables and is

$$\frac{\mathrm{d}\Gamma}{\mathrm{d}w} = \frac{G_F^2}{48\pi^3}m_{D*}^3\big(m_B - m_{D*0}\big)^2\mathcal{G}(w)\mathcal{F}^2(w)|V_{cb}|^2 \ , \qquad (3.30)$$

where

$$\mathcal{F}^2(w)\mathcal{G}(w) = h_{A_1}^2(w)\sqrt{w-1}(w+1)^2\left\{2\left[\frac{1-2wr+r^2}{(1-r)^2}\right]\right.$$
$$\left. \times \left[1+R_1(w)^2\frac{w-1}{w+1}\right] + \left[1+(1-R_2(w))\frac{w-1}{1-r}\right]^2\right\} \ , \qquad (3.31)$$

and $\mathcal{G}(w)$ is a known phase space factor,

$$\mathcal{G}(w) = \sqrt{w^2-1}(w+1)^2\left[1+4\frac{w}{w+1}\frac{1-2wr+r^2}{(1-r)^2}\right]. \qquad (3.32)$$

3.6   Parametrization of the form factors

As stated before, the exactly defined form factor in the heavy-quark limit, the Isgur-Wise function $\xi(w)$, has to be corrected in realistic systems by terms in order of powers Λ_{QCD}/m_b. At minimal w, lattice QCD can be used to obtain the normalization $\mathcal{F}(1)$. Therefore $|V_{cb}|$ can be obtained by extrapolation of measured differential decay rates to $w = 1$.

Since extrapolation necessarily leads to large systematic uncertainties, it is advisable to constrain the shape of the form factors. In this case, the extrapolation is essentially obtained implicitly via determination of a set of free parameters. A suitable approach can be obtained by dispersion tech-

niques ([5], [38], [39], [40], [41]). Starting from first principles, the analytical properties of two-point functions of local currents and the positivity of the corresponding spectral functions, a parametrization can be obtained.

Given that w can vary in the interval $[1, w_{max}[$, with $w_{max} \sim 1.5$, an expansion in $(w - 1)$ may appear advisable. However, the theoretical uncertainties which enter this particular ansatz render it almost useless. A very stable parametrization can be obtained if one introduces a conformal mapping $w \to z(w)$, which transforms the cut w plane onto the interior of the unit disc, $|z| < 1$ [5].

Using the definition

$$z(w) = \frac{\sqrt{w + 1} - \sqrt{2}}{\sqrt{w + 1} + \sqrt{2}}, \qquad (3.33)$$

and Taylor expansion of the form factor $V(w)$, which governs the decay $B \to D\ell\nu$, one obtains [5]

$$\frac{V_1(w)}{V_1(1)} \approx 1 - 8\rho^2 z + (51\rho^2 - 10)z^2 - (252\rho^2 - 84)z^3. \qquad (3.34)$$

If one limits the expression in Eq. 3.34 to the linear term, the parameter ρ^2 can be interpreted as the slope of the form factor. In any case it governs the dependency of the form factor on the kinematic variable w.

For the case $B \to D^*\ell\nu$, Eq. 3.34 can be used to infer relations for the three form factors governing the decay. The ratio of the form factor $A_1(w)/V_1(w)$ can be given as [5]

$$\frac{A_1(w)}{V_1(w)} \approx 0.948(1 - 0.212z - 4.007z^2 - 1.342z^3 + \dots). \qquad (3.35)$$

Using equation Eq. 3.34 one therefore obtains,

$$A_1(w) \approx A_1(1) \left(1 - 8\,\rho^2 z + (53\,\rho^2 - 15)z^2 - (231\,\rho^2 - 91)z^3\right). \qquad (3.36)$$

The ratios $R_1(w)$ and $R_2(w)$ defined in Eqs. 3.21, 3.22 can be represented as

second order polynomials in $(w-1)$ [5],

$$R_1(w) \approx R_1(1) - 0.12(w-1) + 0.05(w-1)^2$$
$$R_2(w) \approx R_2(1) + 0.11(w-1) - 0.06(w-1)^2. \qquad (3.37)$$

While this particular choice of expansion is arbitrary and other parametrizations, like a linear ansatz are possible, this approach is a stable and widely used representation.

The differential decay width with respect to w, $\mathrm{d}\Gamma/\mathrm{d}w$, is usually expressed in terms of one single function $\mathcal{F}$, which can be related to $A_1(w)$, $R_1(w)$ and $R_2(w)$,

$$\left\{1 + \frac{4w}{w+1}\frac{1-2wr+r^2}{(1-r)^2}\right\}\mathcal{F}(w)^2 = \left\{2\frac{1-2wr+r^2}{(1-r)^2}\left[1+\frac{w-1}{w-1}R_1(w)\right]^2\right.$$
$$\left. + \left[1+\frac{w-1}{1-r}\left(1-R_2(w)\right)\right]^2\right\}A_1(w)^2,$$

again with $r = m_V/m_P$. As can be seen, at zero recoil $\mathcal{F}(w)$ and $A_1(w)$ coincide. Thus the labeling of the remaining normalization parameter as $A_1(1)$ or $\mathcal{F}(1)$ is arbitrary.

In the infinite quark-mass limit, the heavy quark symmetry (HQS) predicts $\mathcal{F}(1) = 1$. Corrections to this limit have been calculated in lattice QCD. The most recent result obtained in unquenched lattice QCD reads $\mathcal{F}(1) = 0.921 \pm 0.013 \pm 0.020$ [6]. An older calculation, performed in the quenched approximation, predicts (including a QED correction of 0.7%) $\mathcal{F}(1) = 0.919^{+0.030}_{-0.035}$ [42]. These values are compatible with estimates based on non-lattice methods [43].

3.7   Experimental implications

Eqs. 3.36 and 3.37 reduce the uncertainty due to QCD induced effects from an a priori unknown function into a single normalization factor, $\mathcal{F}(1)$, and a small set of free parameters. If one uses results given in [5], $R_1(1) = 1.27$

and $R_2(1) = 0.8$, or fixes these ratios to values determined otherwise, only the parameter ρ^2 and the normalization $\mathcal{F}(1)|V_{cb}|$ are unknown and are to be determined from data [44, 45, 46, 47]. A more stable approach can be obtained by floating the leading term in the expansions of the functions $R_1(w)$ and $R_2(w)$, Eqs. 3.37, in a fit to real data and thus to determine these values experimentally [1, 2, 9, 48].

This work is based on analyses of Belle data [1, 2], where $\mathcal{F}_1|V_{cb}|$ and all three form factor parameters introduced in the sections above are determined.

Chapter 4

The Belle experiment

The whole is greater than the sum of its parts.

Aristotle

The Belle experiment is situated at the Tsukuba Campus of the Japanese national High Energy Accelerator Research Organization (kō-enerugī kasokuki kenkyū-kikō, KEK). Tsukuba lies about 50 kilometer northeast of Tokyo in the Kanto plain. As of Summer 2009, the Belle collaboration operating the experiment consists of more than 370 scientists from 60 institutions spanning 14 countries of the world. The main goal of Belle is to investigate CP violation in systems of B mesons and, most notably, to test the Cabibbo-Kobayashi-Maskawa mechanism of CP violation. In order to achieve this goal, both an excellent detector system (which is able to identify long-lived particles and to resolve momenta and decay vertices with high accuracy) and a special accelerator setup (which is capable to deliver a high rate of B mesons) are needed.

The Belle experiment has been operational since 1999.

4.1   The KEKB accelerator

The KEKB accelerator consists of two 3 km long beam lines, which are filled by a linear pre-accelerator. An aerial view of the Tsukuba campus and a schematic of the accelerator layout are shown in Fig. 4.1.

The energies of the two KEKB beams are not equal; this setup is called an asymmetric collider. The high energy ring (HER) contains electrons of an energy of 8 GeV, the low energy ring (LER) contains positrons of 3.5 GeV. If filled, the two beams consist of about 5000 bunches of about 10^{10} particles, which corresponds to a bunch crossing rate of about once every 2 ns. The maximal currents reached in the beams are about 1.6 A for HER and 1.1 A for LER. Near the interaction region, the LER beam goes along the axis of the solenoid magnetic field created by the Belle detector, while the HER beam is tilted horizontally by $\theta_{beam} = 22$mrad.

Neglecting the electron mass, the components of the four-momenta of the two beams are[1]

$$p_H = \begin{pmatrix} E_H \\ 0 \\ E_H \, \sin\theta_{beam} \\ E_H \, \cos\theta_{beam} \end{pmatrix}, \; p_L = \begin{pmatrix} E_L \\ 0 \\ 0 \\ -E_L \end{pmatrix}, \tag{4.1}$$

and the invariant mass of $P = p_H + p_L$ is

$$\sqrt{s} = \sqrt{P_\mu P^\mu} = \sqrt{2E_H E_L(1 + \cos\theta_{beam})} \approx 2\sqrt{E_H E_L} \approx 10.58\text{GeV}. \tag{4.2}$$

This it the mass of the third radially excited $b\bar{b}$ state, the so-called $\Upsilon(4S)$, which decays almost exclusively into pairs of B mesons [18].

The cross section of $e^+e^- \rightarrow hadrons$ as shown in the review [50] can be seen in Fig. 4.2.

This mass is only marginally higher than the mass of 2 B mesons, therefore these particles are created nearly at rest in the center of mass frame. Due to

---

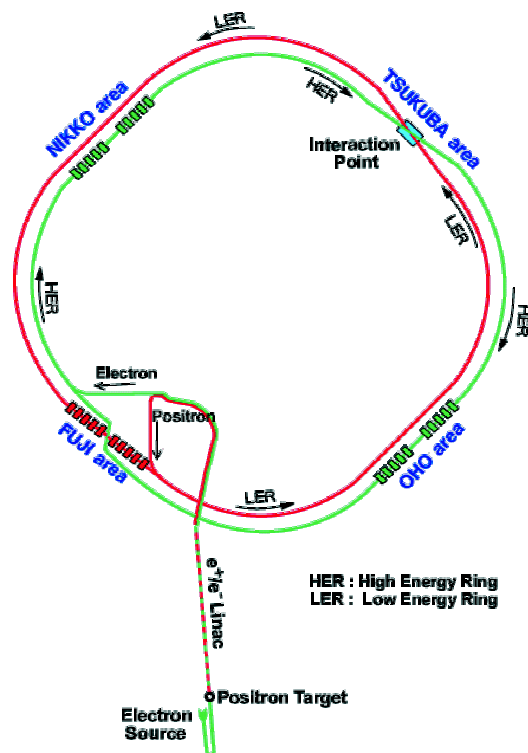[1]The coordinate system used below is defined in Fig. 4.4.

Figure 4.1: Top: Aerial view of KEK with Mt. Tsukuba in the background. Bottom: Schematic of the KEKB accelerator. [49]
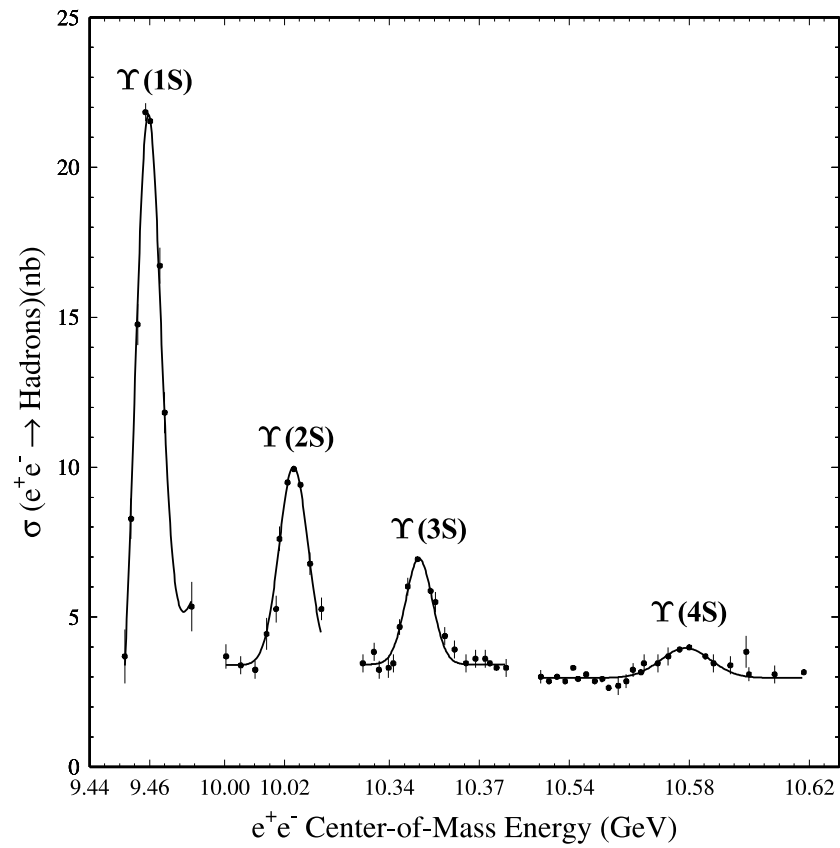
Figure 4.2: Measurements of the hadronic cross section of e^+e^- as a function of the center-of-mass energy. The four clearly visible resonances correspond to bound $b\bar{b}$ states, the Υ vector mesons. [50]

the asymmetry of the colliding beams there is a Lorentz boost between the laboratory and the center-of-mass frame. Therefore, from the point of view of the detector, the particles experience time dilation, with a boost factor $\beta\gamma \approx 0.425$. This increases the average flight length of the two B mesons to about $200\mu m$ and therefore simplifies the separation of the two decay vertices.

The performance of an accelator is characterized by its peak luminosity, $\mathcal{L}$, which can be obtained from the rate of e^+e^- collisions, R. It is defined by

$$R = \mathcal{L}\sigma_{e^+e^-}, \tag{4.3}$$

where $\sigma_{e^+e^-}$ is the total e^+e^- cross section. Due to losses of the beams, mainly by interactions with rest gas in the vacuum tube, the luminosity of a so-called "fill" degrades exponentially with time. Therefore, the beams either have to be dumped and completely refilled after a certain time, or they have to be continuously refilled. The second approach is currently used at KEK. While more challenging in terms of accelerator operation, this allows for a more efficient recording of data by the experiment. KEKB was designed to reach a peak luminosity of $10^{34}cm^{-2}s^{-1}$, however, it exceeded this goal in 2004. The maximum peak luminosity achieved so far by the accelerator was $2.11 \times 10^{34}cm^{-2}s^{-1}$, on June 17, 2009.

The integrated luminosity, which corresponds to the total number of events recorded at KEK, reached 950 fb^{-1} in summer 2009. Fig. 4.3 shows the official snapshot of integrated luminosity versus time.

4.2 The Belle detector

The aim of the Belle experiment is to allow for precise investigations of the decay of B mesons, with the main objective being the measurement of CP violation in B systems. For this, high precision in the determination of decay vertices and the momenta of the particles produced in these decays is necessary.
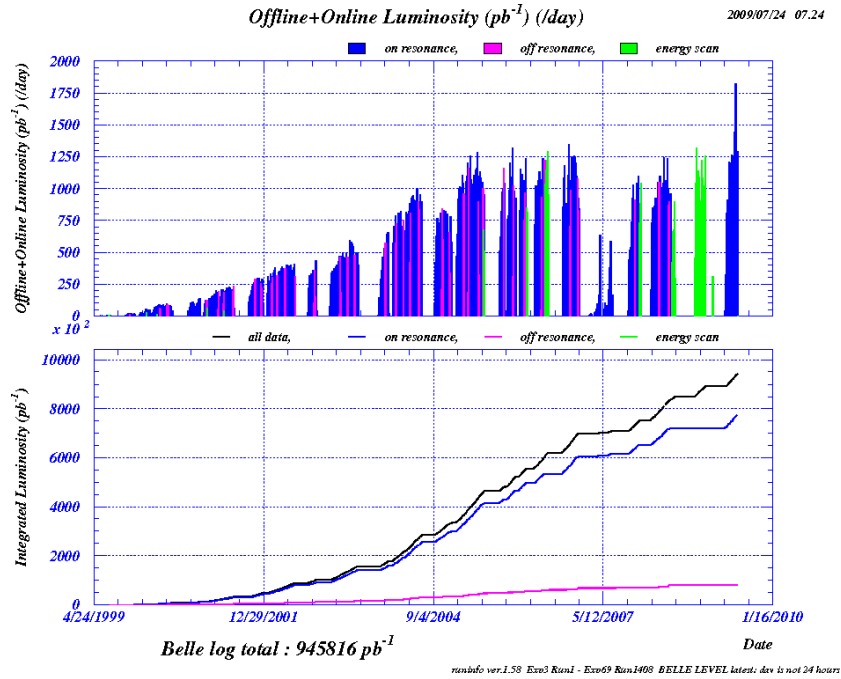
Figure 4.3: The integrated luminosity recorded by the Belle experiment, from 1999 until summer 2009. The colors indicate accelerator setups with different center-of-mass energies. Blue: E_{cm} on the $\Upsilon(4S)$ resonance ("on-resonance data"), pink: E_{cm} below the $\Upsilon(4S)$ resonance ("off-resonance data"), green: E_{cm} near the $\Upsilon(5S)$ resonance ("energy scan").

Fig 4.4 and 4.5 show schematics of the Belle detector. Fig. 4.4 also contains
the definition of the commonly used coordinate system: The z axis is set along
the axis of the magnetic field created by the Belle detector, i.e. opposite to
the direction of the LER. The x axis is the horizontal radial axis, and the y
axis is the axis perpendicular to both, such that (x, y, z) form a right-handed
coordinate system. The polar angle θ is measured with respect to the z axis,
the azimuthal angle ϕ in the (xy) plane with respect to the x axis.

The Belle detector is a magnetic spectrometer covering a large-solid-angle.
It is designed as a nearly 4π detector, the acceptance of the main compo-
nents covering a range $\theta \in (17°, 150°)$ in the polar angle. The main com-
ponents comprise a Silicon Vertex Detector (SVD), a 50-layer Central Drift
Chamber (CDC), an Aerogel Čerenkov Counter system (ACC), a barrel-like
arrangement of Time-Of-Flight scintillation counters (TOF), and an Electro-
magnetic Calorimeter (ECL).These components are located inside a super-
conducting solenoid coil that provides a 1.5 T magnetic field. The final part
of the detector is an iron flux-return located outside the coil. This compo-
nent is instrumented to operate as a K_L and μ detection system (KLM). The
detector is described in great detail in Ref. [51].

4.2.1   Interaction region

In order to allow efficient operation of the experiment, the two colliding
beams have to travel in high vacuum which is maintained within the so-
called beam pipes. In the primary interaction region (IP) the two separate
pipes of the HER and the LER merge into one.

For many analyses, the precise determination of decay vertices is critical.
The dominating limiting factor in the resolution in z-direction is multiple
Coulomb scattering. In order to reduce it, the material budget in the im-
mediate vicinity of the interaction has to be minimized. This is achieved by
constructing the central part of the beam pipe as a double-wall beryllium
cylinder (with a thickness of 0.5 mm for each wall) which is mounted on alu-
minium pipes extending to the outside of the interaction region. The inner
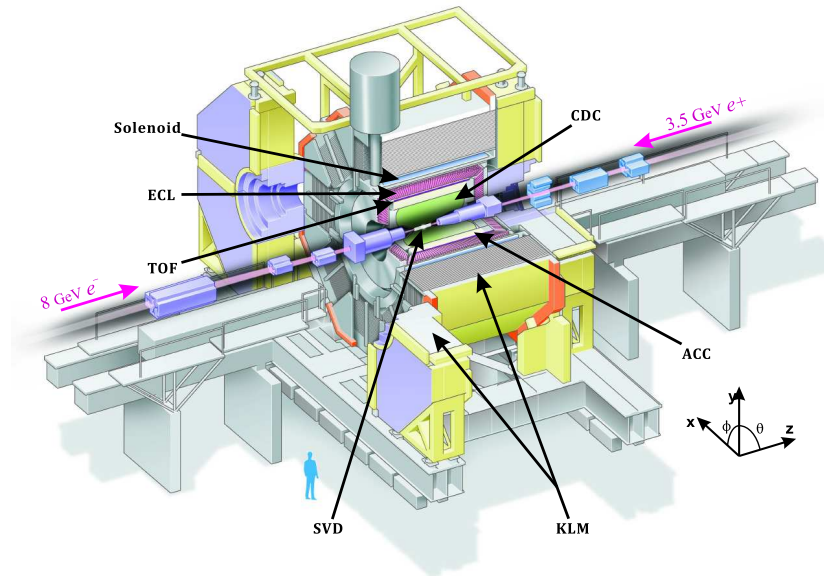diameter was 40 mm at the startup of the Belle experiment, during a detec-

Figure 4.4: Schematic of the Belle Detector. ([49], high lights and coordinate system by the author)
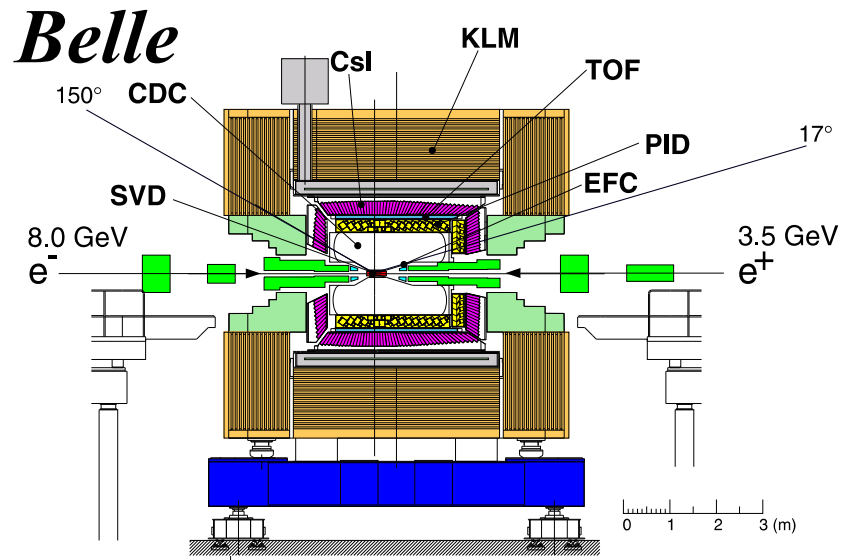

Figure 4.5: Sideview of the Belle Detector. [51]

tor upgrade in 2003 this was reduced to 30 mm. A 2.5 mm gap between the
two walls is constantly flushed with helium gas for cooling. This is necessary
since on the one hand placing the vertex detectors as close as possible to
the interaction point improves the vertex resolution, while on the other hand
the beam-induced heating of the beam pipe reaches levels of a few hundred
watts. This heat level might damage the detectors if not compensated by
active cooling.

To shield the interaction region from beam induced background several hor-
izontal masks have been installed. For example, synchrotron radiation is
shielded such that it is either blocked by a mask or passes the IP without
interacting with the beam pipe.

4.2.2   Silicon vertex detector (SVD)

The main objective of Belle is to investigate time-dependent CP violation
in B meson decays. To achieve this, the distance in z direction between the
decay vertex positions of B meson pairs has to be measured with a precision
of about 100 μm. This is the main task of the SVD. However, the information
of this subdetector is also important for identification and measurement of
D and τ particles as well as for tracking generic charged tracks.

Silicon detectors are extremely fast detectors, with response times of a few
nanoseconds. The typical width of the silicon wafers is of the order of a few
100 μm.

The basic idea of a silicon detector is as follows: A voltage is applied to a
volume of doted silicon, with highly doted silicon being used as cathodes and
anodes. In particle detectors, the voltage is usually chosen sufficiently high to
completely deplete the silicon bulk. If an ionizing particle passes the detector
volume, electrons of the valence band are excited into the conduction band
and electron-hole pairs are created. Due to the electric field, these pairs drift
to the electrodes and induce an electrical signal, which can then be amplified
and interpreted.

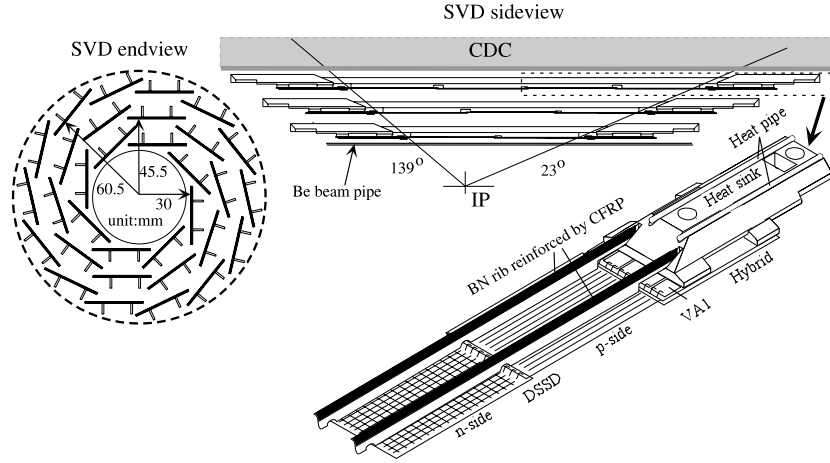In case of a so-called "micro strip detector", the cathode is not simply a plate,

Figure 4.6: Schematic view of the three-layer SVD1 detector. [51]

but is segmented. In case of a "double sided silicon detector", both the cathode and the anode are segmented into strips, with their relative orientation being rotated by 90°. In this configuration two-dimensional information on the location of the incident particle is available, by analyzing the current induced in various strips.

As already stated above, Coulomb scattering is a dominating factor in vertex resolution, especially since most of the particles of interest in Belle carry momenta of less than 1 GeV/c. In order to reduce the material budget, the mechanical support structure has to be as light as possible while still preserving the necessary stability. Additionally, the readout electronics is placed outside of the tracking volume.

The first silicon detector consisted of three layers of double sided silicon detectors, the polar coverage was $\theta \in (23°, 139°)$. During an upgrade in 2003 a fourth layer was installed. The polar coverage of the upgraded SVD was increased to match the coverage of the CDC, $\theta \in (17°, 150°)$. To distinguish the two configurations, the newer one is called the *SVD2*, Fig. 4.7, while the older is now labeled the *SVD1*, Fig. 4.6. The read-out electronics of the *SVD2* has been constructed with strong participation by the Institute for High Energy Physics in Vienna.
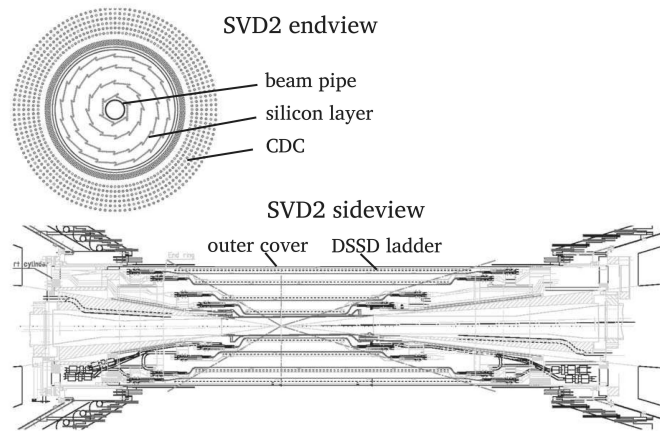
SVD2 endview

beam pipe
silicon layer
CDC

SVD2 sideview
outer cover   DSSD ladder

Figure 4.7: Schematic view of the four-layer SVD2 detector. [52]

4.2.3 Central drift chamber (CDC)

Virtually all measurements at the Belle experiment depend on the precise determination of the momenta of charged tracks. For this purpose the Belle detector was equipped with a drift chamber.

Drift chambers operate on the principle of gas ionization, that is, a particle transversing the detector volume excites outer shell electrons of gas molecules or atoms sufficiently to create an electron-ion pair.

The electric field in the inner part chamber is extremely homogeneous. The ionized particles are accelerated until they reach a saturation velocity where the energy gained from the electrical field equals the average energy lost due to interactions with the surrounding gas. Once this velocity is reached there is a simple linear correlation between the time the particles take to reach the cathodes and the velocity. Exact determination of the incident time therefore allows accurate determination of the position of the incident particle.

The momentum of the particle is not directly determined via time measurements. Multiple measurements of the position of the incident particle allow to determine an accurate estimate of the particle path. In the very homogeneous field of a solenoid magnet an excellent approximation of the track will

be a helix, with the curvature being inversely proportional to the particle momentum. At Belle, this is realized in a 1.5 T solenoid magnetic field.

Fig. 4.8 shows the configuration of the CDC. Since due to the asymmetric beam energies the center of mass carries a non-zero momentum in z direction, the CDC has been constructed asymmetrically as well. This ensures an angular coverage of $\theta \in (17°, 150°)$. It consists of 50 cylindrical layers, with radii between 103.5 mm and 874 mm. In total, 8400 drift cells make up the detector.

A low-Z gas is used in the CDC to minimize multiple Coulomb scattering. Additionally this also reduces background from synchrotron radiation, since low-Z gases feature a smaller photo-electric cross section than e.g. argon-based gas mixtures. The Belle CDC is filled with a 50% helium-50% ethane gas mixture. The radiation length of this mixture is about 640 m, the drift velocity saturates as 4 cm/μs. The large ethane component increases the dE/dx resolution, which improves particle identification of charged particles.

4.2.4 Particle identification - Time-Of-Flight scintillation counters (TOF), Aerogel Čerenkov Counter system (ACC)

The combination of SVD and CDC allows for an accurate determination of the spatial momentum of charged tracks. The forth momentum component can either be determined directly, by measuring the energy of the particle, or via particle identification, which allows to determine the particle mass. In the energy range probed by the Belle experiment the latter approach is very efficient. The identification of electrons and muons relies to a large extent on the shower shape in the ECL respectively the signal in the muon chambers and is extremely accurate. The separation of charged hadrons is more difficult. Therefore, the Belle detector features two dedicated components for this purpose, the TOF and ACC. The information of these two components are combined with dE/dx information from the CDC to obtain a good separation of different types of charged particles, with special emphasis being
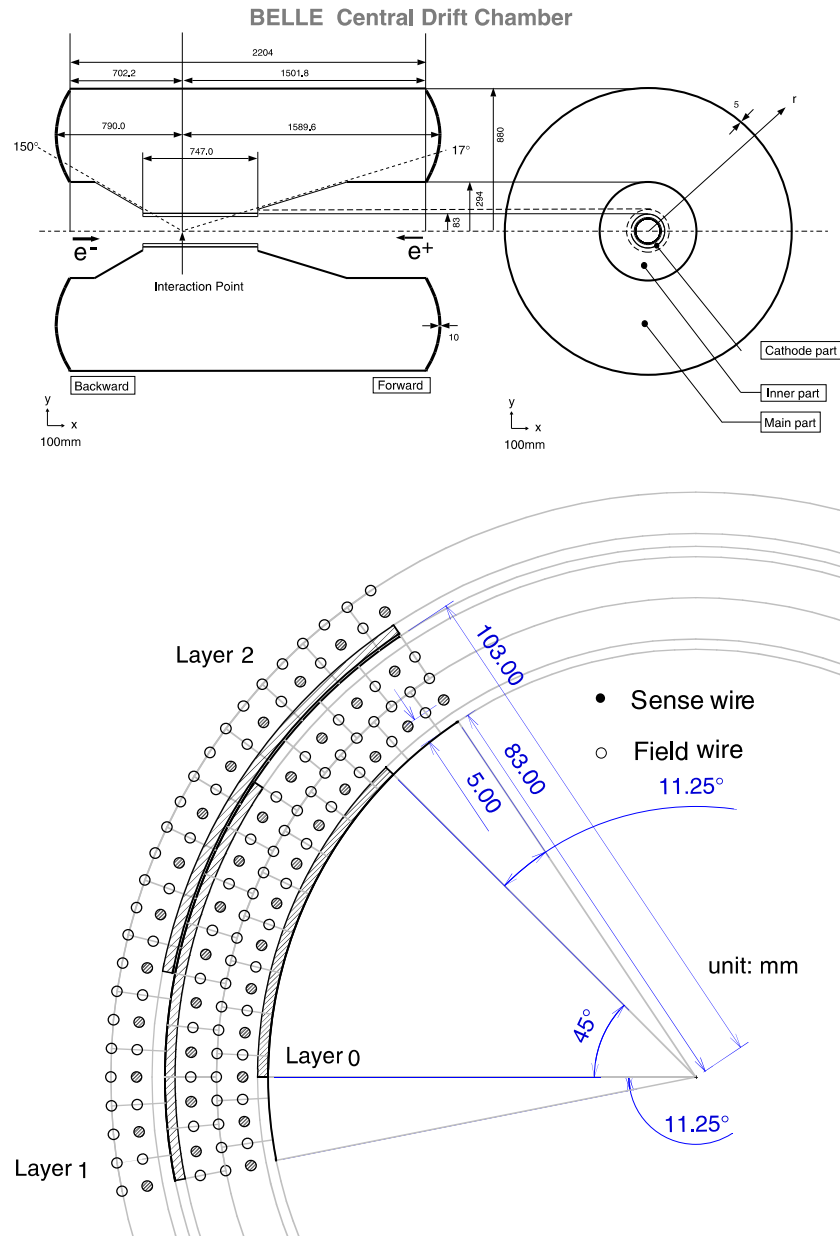
Figure 4.8: Top: Longitudinal structure of the central drift chamber of the Belle experiment. Bottom: Cell structure and the cathode sector configuration of the central drift chamber. [51]

placed on the separation of $\pi^\pm$ from $K^\pm$ mesons.

Time-of-Flight counters (TOF)

Time-of-flight measurements rely on extremely precise time measurements of an incident particle. Two time stamps are needed to calculate the particle velocity. Combined with a separate measurement of the particle momentum, e.g. via the curvature of the track in a magnetic field, this allows the determination of the particle mass and thus to identify the particle.

A TOF system with 100 ps time resolution is effective to provide particle identification for momenta below about 1.2 GeV. About 90% of the tracks produced in $\Upsilon(4S)$ decays fall into this momentum range. Additionally, the TOF subdetector also provides fast timing signals for the trigger. To keep the TOF trigger rate below a critical value of about 70 kHz, additional thin trigger scintillation counters (TSC) are used to complement the TOF counters. In each event, the signal from two ends of a TOF counter is averaged and put into coincidence with the signal of a TSC counter to create a fast trigger signal. If the TSC did not give a signal, the information from the TOF modules is discarded.

Fine-mesh-dynode photomultiplier tubes are placed directly on the TOF and TSC scintillation counters, which consist of fast scintillators with an attenuation length longer than 2m. 64 TOF/TSC modules make up the detector. They are placed at a radius of 1.2 m from the interaction point and cover a polar angle range $\theta \in (34°, 120°)$.

Fig. 4.9 shows the $\pi^\pm/K^\pm$ separation power based on information obtained exclusively from TOF measurements.

Aerogel Čerenkov counter system (ACC)

TOF and $\mathrm{d}E/\mathrm{d}x$ measurements in the CDC distinguish $\pi^\pm$ from $K^\pm$ mesons in a low-momentum region. To extend the range of particle identification an array of silica aerogel threshold Čerenkov counters is used.
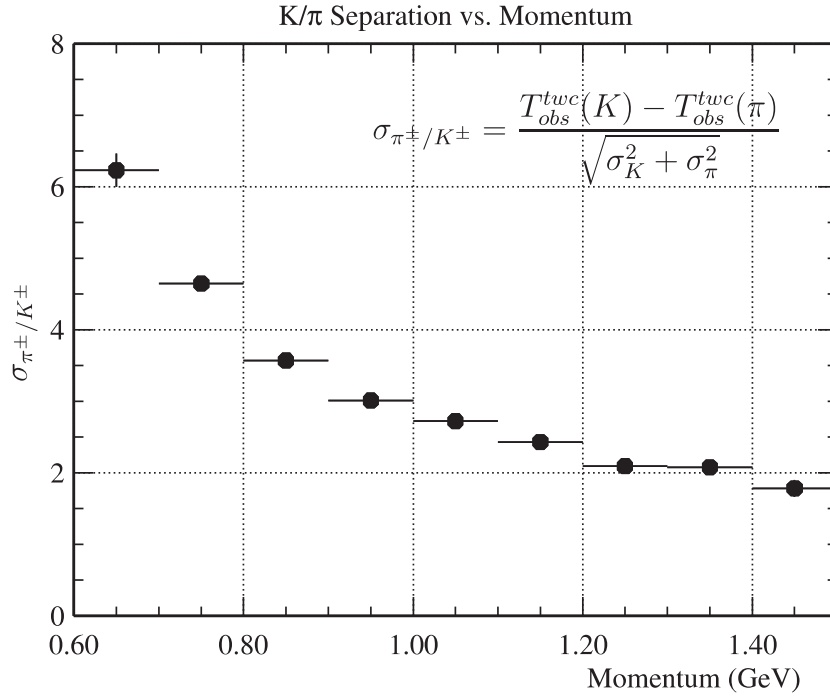
Figure 4.9: $\pi^{\pm}/K^{\pm}$ separation by the TOF subdetector. σ_K and σ_π are the time resolutions for Kaons and Pions, respectively. These quantities are momentum dependent. T_{obs}^{twc} is defined by the empirical formula $T_{obs}^{twc} = T_{raw} - \frac{z}{V_{eff}} + \frac{S}{\sqrt{Q}} + F(z)$, where T_{raw} is the signal time, z is the particle hit position on a TOF counter and Q is the charge of the signal. V_{eff}, S and $F(z)$ are obtained from optimizing T_{obs}^{twc} against the time-of-flight predictions using the track length calculated from the fit to hits in CDC. [51]

Čerenkov radiation is emitted when a charged particle's velocity exceeds the speed of light in a medium, i.e. if the relation

$$|\vec{v}| \geq \frac{c}{n}$$

(4.4)

holds, where n is the index of refraction of the medium. If set up correctly, two particles with the same momentum, but different mass and therefore different velocity, will not both emit Čerenkov radiation, which allows to distinguish them. Only about 1% of the particle energy is emitted as Čerenkov radiation, therefore this method does not seriously hamper the determination of the particle energy with subsequent detectors.

The ACC barrel part consists of 960 counter modules segmented into 60 cells in ϕ direction, the forward end-cap part is made up by 228 modules arranged in 5 concentric layers. The typical ACC module is made of 5 aerogel tiles, stacked inside a thin aluminium box. One or two fine mesh-type photomultiplier tubes are attached directly to the aerogels, in order to allow efficient detection of Čerenkov light.

For each charged track one can calculate a probability of the track being a kaon, P_K, and the probability of having found a pion, P_π, based on the information of the ACC. The discriminating variable is usually the so-called likelihood ratio,

$$PID(K) = \frac{P_K}{P_\pi + P_K}, PID(\pi) = 1 - PID(K),$$

(4.5)

which takes values in the range $(0, 1)$. Fig. 4.10 shows the likelihood ratio $PID(K)$ as a function of particle momentum. As mentioned above, the identification of electrons and muons relies on other detector components. Therefore, the two probabilities defined in Eq. 4.5 are the most important output derived from the ACC.
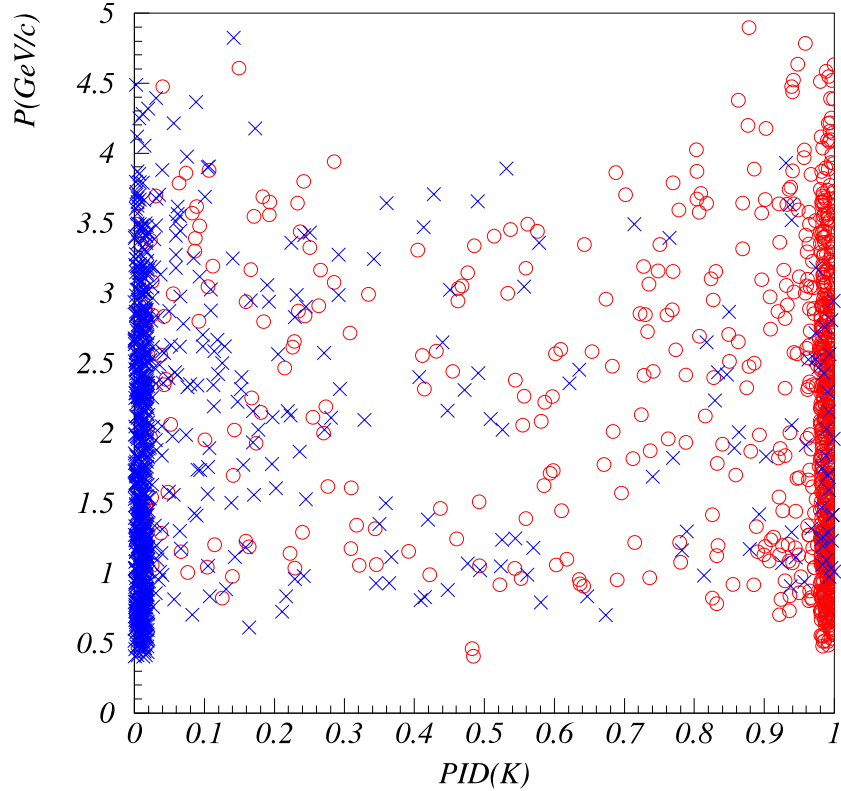
Figure 4.10: Two dimensional plot of the π/K likelihood ratio based on information of the ACC subdetector versus the particle momentum. Blue crosses: charged pions, red circles: charged kaons. A performance test using tagged $D^0 \to K^-\pi^+$ events in real data is shown. Due to very efficient tagging of either a D^0 or $\bar{D}^0$, and with $D^0 \to K^-\pi^+$ being the only D^0 decay emitting exactly two charged particles, the charge of the particles is directly correlated to the flavor. This allows to cross check the information obtained from the ACC ([51]).

4.2.5   Electromagnetic calorimeter (ECL)

The aim of a calorimeter is to absorb the total energy of an incident particle, in order to allow an energy measurement. Both neutral and charged particles can be detected and measured.

Detection of photons emitted in B-meson decays is the prime objective of the Belle ECL sub detector. Most of these photons are end-products of decay cascades and therefore carry momenta below 500 MeV. But certain decays like $B^0 \rightarrow \pi^0\pi^0, \pi^0 \rightarrow \gamma\gamma$ can emit high energy photons, with energies up to 4 GeV in the laboratory rest frame. Therefore high resolution is required in a wide energy range. Detection of high momentum π^0 additionally requires good separation of two nearby photons and determination of their small opening angle. Therefore a fine-grained segmentation in the calorimeter is required.

Additionally, electron identification relies primarily on the comparison of measured charged track momentum and the energy deposition in the ECL. Due to bremsstrahlung, electrons experience a strong electromagnetic interaction when passing the rather dense material of the ECL and are unable to traverse the subdetector. The energy deposited by an electron has to match the kinetic energy of the charged track plus the nearly negligible electron mass. Good resolution in this detector part therefore increases fake electron rejection.

A highly segmented array of 8736 Thallium doped Caesium Iodide ("CsI(Tl)") scintillator crystals with silicon photodiode readout is used as the ECL at Belle. These crystals feature large photon yield, weak hygroscopicity and high mechanical stability. The configuration of the ECL can be seen in Fig. 4.11. The barrel region is made up of a section of 3.0 m length with an inner radius of 1.25 m. Two end-caps are placed at $z = +2.0$ m and $z = -1.0$ m from the interaction point. The ECL has a polar coverage of $\theta \in (17°, 150°)$. Gaps due to cable pathways and other construction components lead to a small reduction of about 3% of the total acceptance.

In scintillation crystals, atoms or molecules are easily excited by photons or

charged particles. In the dexcitation to the ground state photons are emitted, typically in the wave length range from visible to X-rays. This light signal is then conducted via a light waveguide to a photo multiplier, where it is converted into an electrical signal.

In a calorimeter such a scintillation process does not occur only once per incident particle, rather a so-called "shower" is created. For high energetic particles the ionization and excitation processes which lead to scintillation process do not dominate the inelastic cross section. For electrons and positrons with momenta above $\sim 10\text{MeV}$ bremsstrahlungs effects dominate and photons are radiated into the detector volume, $e^{\pm} \to e^{\pm}\gamma$. For photons with similar momenta pair production dominates, $\gamma \to e^{+}e^{-}$. These processes create an electromagnetic cascade. In each step additional photons, electrons and positrons are created, until the average energy of the shower particles drops below the critical energy of about 10MeV. Once this threshold has been reached, ionization and excitation processes start to dominate, which in turn result in a scintillation signal.

The effective shielding of materials is usually given in units of the so-called "radiation length". After having passed one radiation length x_0 the energy of a traversing particle has been reduced by a factor $1/e$ part of the incident energy,

$$E(x) = E_0\, e^{-\frac{x}{x_0}}. \tag{4.6}$$

The size of the ECL corresponds to 16 radiation lengths for photons. Therefore only a minimal part of the photon energy is not deposited within the ECL.

Extreme forward calorimeter (EFC)

In addition to the central ECL detector, the Belle experiment is also equipped with an Extreme Forward Calorimeter (EFC), which is placed in the very high-radiation area around the beam pipe near the interaction point. It covers the polar angle intervals $\theta \in (6.4°, 11.5°)$ and $\theta \in (163.3°, 171.2°)$ and consists of radiation hard Bismuth Germanate crystals.
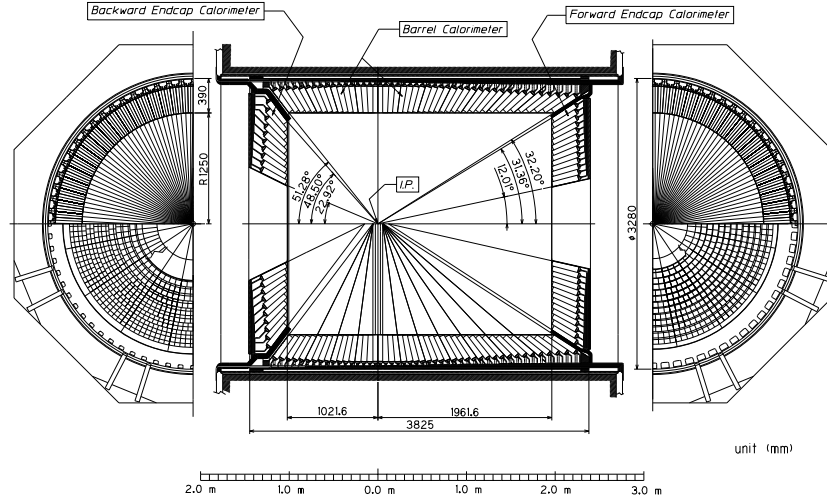
Figure 4.11: Overall configuration of the main electromagnetic calorimeter. [51]

The main purpose of the EFC is the usage as a beam monitor for the KEKB control and as a luminosity monitor. Additionally it also functions as a radiation shield for the more sensitive CDC sub detector. The information acquired by the EFC is usually not included in physics analyses.

4.2.6 K_L and μ detection system (KLM)

The only particles capable of traversing the calorimeter are charged and neutral hadrons, most notably the K_L^0 meson, and muons. These particles are stable enough so that most of them decay outside the detector, and they do not interact strongly enough with the crystals of the ECL to deposit all of their energy there.

The purpose of the so-called KLM is to identify K_L and muons with a momentum greater than 600 MeV/c. The barrel covers the angular region $\theta \in (45°, 125°)$ and two end caps the regions $\theta \in (20°, 45°)$ and $\theta \in (125°, 150°)$.

The active detector components consist of glass resistive plate counters [53, 54, 55], which consist of two parallel plate electrodes separated by a gas-filled

gap. An ionizing particle traversing the gap induces a streamer in the gas, which results in a local discharge of the plates. This discharge then results in a signal on external pickup strips.

The detector consists of alternating layers of charged-particle detectors and 4.7 cm thick iron plates. 15 detector and 14 iron layers make up the barrel, the end caps consist of 14 layers of each component. The main purpose of the iron components is to serve as a flux return yoke for the magnetic field of 1.5 T created by the Belle solenoid. It also serves as an absorber material for K_L which interact with the iron and produce a shower of ionizing particles, providing a total of 3.9 radiation lengths of material (in addition to the about 0.8 radiation lengths provided by the ECL). However, the size of the total shower produced by K_L mesons fluctuates. Therefore an accurate measurement of the K_L energy is not possible and only the direction of the K_L can be determined.

Separation of muons from charged hadrons is achived by comparing the energy deposition of the charged track along its path. In contrast to strongly interacting particles, muons deposit only a marginal fraction of their energy prior to entering the KLM system. Muons with momenta below 500 MeV/c do not reach the KLM and have to be discarded.

4.2.7   Solenoid magnet

A superconducting solenoid provides a 1.5 T magnetic field [56, 57, 58]. The nearly homogeneous part of the field covers a cylindrical volume of 3.4 m in diameter and 4.4 m in length.

The solenoid is positioned between the particle identification detectors (ACC, TOF) and the ECL.

Figure 4.12: The Belle Collaboration. Graphics created by the author on behalf of the collaboration.

4.3   The Belle collaboration

The Belle collaboration is an international consortium of scientists, who built and operate the Belle detector and analyse the data recorded by it. It currently consists of more than 370 members from 60 institutions in 14 countries of the world (see Fig. 4.12 for illustration).
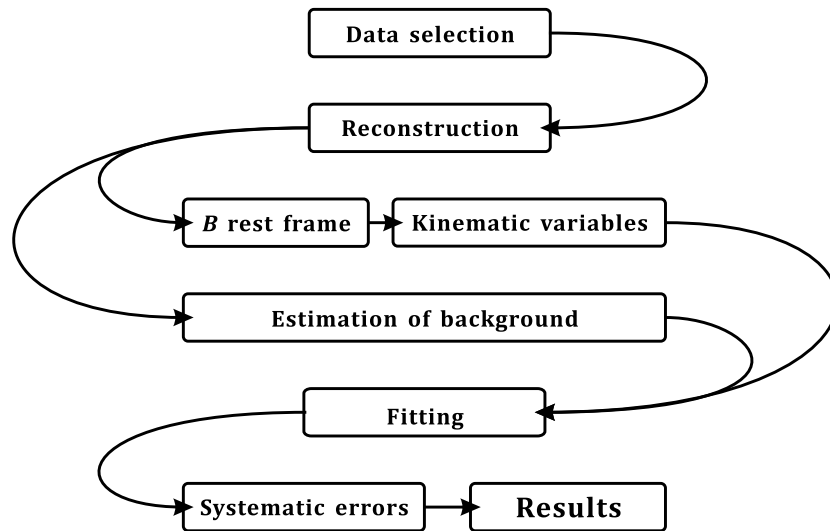
Figure 4.13: Illustration of all analysis steps which have been taken to obtain the results presented in this work from data recorded by the Belle Experiment. The individual steps will be explained in detail in the following chapters.

Chapter 5

Reconstruction of events

The man who moves a mountain begins by carrying away small stones.

Confucius

5.1 Data sample

The two analyses presented here use the Belle data taken until summer 2003. This data set consists of 140 fb^{-1} taken at the $\Upsilon(4S)$ resonance. Considering the production cross section of $e^+e^- \to b\bar{b}$ this corresponds to about 152 million $B\bar{B}$ events. Another 15 fb^{-1} taken 60 MeV below the resonance are used to investigate and subtract the non-$B\bar{B}$ background, which is often labeled as "continuum background".

For determination of several background sources from B meson decays, Monte Carlo (MC) samples equivalent to about three times the integrated luminosity are used. Monte Carlo simulated events are generated with the EVTGEN program [59], followed by full detector simulation based on GEANT [60]. Effects due to QED bremsstrahlung in $B \to X\ell\nu$ decays are added using the PHOTOS package [61].
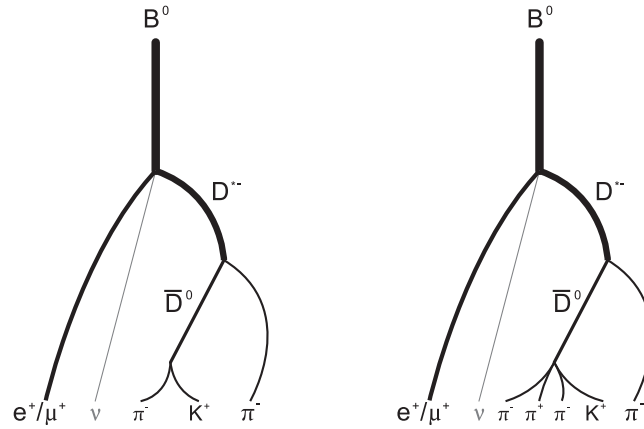
Figure 5.1: Schematic representation of the reconstructed B^0 decay cascades. The left schematic shows the $D^0 \rightarrow K^-\pi^+$ mode, the right one the $D^0 \rightarrow K^-\pi^+\pi^-\pi^+$ mode. The labels in the bottom line indicate the particles which traverse the detector and can either be reconstructed (black) or are invisible to the experiment (the neutrino, gray), while the particles drawn above them decay within the detector volume and cannot be detected directly. The tracks of charged particles are curved to indicate the deflection in a magnetic field. Neither the curvature nor the length of the drawn lines are indicative of particle properties (like the mean lifetime or the momentum).
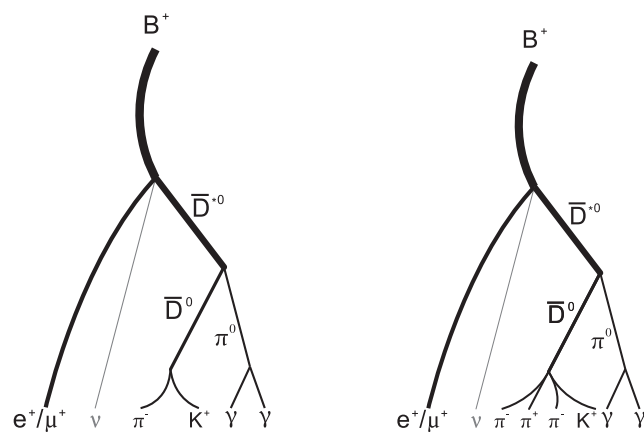

Figure 5.2: Same as Fig. 5.1 for the reconstructed B^+ decay cascades.

5.2   Event reconstruction

Let $\bar{B}$ represent either a neutral $\bar{B}^0$ or a charged B^- meson. The decay cascade $\bar{B} \to D^*\ell^-\bar{\nu}_\ell$, $D^* \to D^0\pi_s$ and $D^0 \to K^-\pi^+$ or $D^0 \to K^-\pi^+\pi^-\pi^+$ is reconstructed[1], with ℓ being a light charged lepton, $\ell \in \{e, \mu\}$. Thus, a total of four decays channels is investigated in each of the analyses ("$K\pi, e$"; "$K\pi, \mu$"; "$K3\pi, e$"; "$K3\pi, \mu$"). A graphic representation of the decay cascades can be seen in Fig. 5.1 and 5.2.

The K and π mesons, as well as the muon μ, are unstable particles and proceed to decay further. However, their mean lifetime is long enough for them to traverse the Belle detector and produce signals in the various detector components. Any possible decays occurring at a later point are irrelevant for analyses of Belle data.

In case of $\bar{B}^0$ decays, a D^{*+} meson is produced and the low momentum pion emitted in the D^* decay, which is often labeled "slow" or "soft" pion, will be charged, π_s^+. In B^- decays, the D^{*0} meson will emit a neutral pion, which decays predominantly into two photons, $\pi_s^0 \to \gamma\gamma$.

The final states which are detected by the Belle detector therefore amount to one charged high momentum kaon, one (three) charged high momentum pions and one light lepton in case of the $D^0 \to K\pi$ ($D^0 \to K3\pi$) mode. In B^0 decays we find one additional low momentum charged pion, in B^+ decays the two photons emitted by a low momentum neutral pion.

Hadronic events are selected based on the charged track multiplicity and the visible energy in the calorimeter. The selection is described in detail in Ref. [62]. We also apply a moderate cut on the ratio of the second to the zeroth Fox-Wolfram moment [63], $R_2 < 0.4$, to reject non-$B\bar{B}$ events.

---

[1] As mentioned before, throughout this entire work charge conjugation is implied, *i.e.* we differentiate neither between the decays $\bar{B}^0 \to D^{*+}\ell^-\bar{\nu}_\ell$ and $B^0 \to D^{*-}\ell^+\nu_\ell$ nor between $B^- \to D^{*0}\ell^-\bar{\nu}_\ell$ and $B^+ \to \bar{D}^{*0}\ell^+\nu_\ell$.

5.2.1 D^0 selection

As stated above, neutral D meson candidates are searched for in the decays channels $D^0 \to K^-\pi^+$ ("$K\pi$") and $D^0 \to K^-\pi^+\pi^-\pi^+$ ("$K3\pi$"). Depending on the selected D^0 channel, one kaon and either one or three pions are searched for in any event passing the soft constraints mentioned above. These tracks are then combined to form a D^0 candidate, $i.e.$ the four-momenta of the selected charged tracks are added to form the four-momentum of the D^0 candidate.

These particles are required to originate from the interaction point. To ensure this, the impact parameters in $R\phi$ and z have to satisfy $dr < 2$ cm and $|dz| < 4$ cm, respectively. This ensures that the helices contain points within the beam pipe. Additionally, we demand at least one associated hit in the SVD detector. The Čerenkov light yield from ACC, the time-of-flight information from TOF and dE/dx from CDC are required to be consistent with the respective mass hypothesis. As mentioned in section 4.2, a likelihood function can be formed using these informations. Kaon candidates are required to have a kaon likelihood with respect to the pion hypothesis greater than 0.6, pion candidates must have a kaon likelihood less than 0.9.

We fit the charged tracks to a common vertex and reject the D^0 candidate if the χ^2 probability is below 10^{-3}. The momenta of the charged tracks are re-evaluated at the vertex and the D^0 4-momentum is calculated as their sum. The reconstructed D^0 mass is required to lie within ± 3 standard deviations from the nominal mass of about 1.865 GeV$/c^2$ [18]. The standard deviation σ is measured from real data and is found to be about 4.5 MeV$/c^2$ (4 MeV$/c^2$) for the one (three) pion mode.

5.2.2 D^{*+} selection

In case of D^{*+} reconstruction, the D^0 candidate is combined with a slow pion π_s^+. The sign of the π charge is chosen appropriately with respect to the kaon candidate. Due to the low momentum of this π_s candidate, reconstruction efficiency is much lower than in case of the faster tracks emitted

by the D^0. No impact parameter and SVD hit requirements are applied for the π_s. However, we again perform a vertex fit and apply the same vertex requirement, $P_{\chi^2} > 10^{-3}$. The invariant mass difference between the D^* and the D candidates, $\Delta m = m_{D^*} - m_{D^0}$, is required to lie within 0.144 and 0.147 GeV/c^2. Additional suppression of $e^+e^- \to q\bar{q}$ processes is achieved by requiring a D^* momentum below 2.45 GeV/c in the c.m. frame.

5.2.3 D^{*0} selection

To form a D^{*0} candidate, the D^0 candidate is combined with a slow neutral pion π_s^0. The π_s^0 is obtained by combining two photons with $E_\gamma > 100$ MeV for $\theta < 32°$, $E_\gamma > 150$ MeV for $\theta > 130°$, and $E_\gamma > 50$ MeV for photons detected in the barrel region. The invariant $\gamma\gamma$ mass has to lie within 3 standard deviations of the nominal π^0 mass of about 135 MeV/c^2 [18], with $\sigma \approx 5$ MeV/c^2. Additionally, a mass constraint fit is performed and the fit probability has to exceed 10^{-2}. Suppression of non-$B\bar{B}$ background is again achieved by requiring a D^{*0} momentum less than 2.45 GeV/c in the c.m. frame.

For the final fit, only events with an invariant mass difference Δm within 0.140 and 0.1445 GeV/c^2 are considered. However all events in the region $\Delta m \in (0.1355, 0.158)$ GeV/c^2 are investigated to estimate the background.

5.2.4 B candidate selection

Finally, the D^{*0} candidate is combined with a lepton (electron or muon), appropriately charged with respect to the kaon. Both electron and muon candidates have to satisfy the same impact parameter requirement applied to fast kaons and pions, $dr < 2$ cm and $|dz| < 4$ cm.

Additionally, electron candidates are identified using the ratio of the energy detected in the ECL to the track momentum, the ECL shower shape, position matching between track and ECL cluster, the energy loss in the CDC and the response of the ACC counters. The polar angle with respect to the beam has

to lie within 17° and 150°. No SVD hit is required. Muons are identified based on their penetration range and transverse scattering in the KLM detector. The polar angle lies within 25° and 145°. Again, no SVD hit requirement is applied. In the momentum region relevant to this analysis and with the set of standard cuts discussed in Ref. [64, 65], charged leptons are identified with an efficiency of about 90% and the probability to misidentify a pion as an electron (muon) is 0.25% (1.4%).

To supress background, the momenta of the lepton candidates are required to exceed certain thresholds. In the lab frame, the (transverse) momentum of the lepton is required to exceed 0.80 GeV/c (0.65 GeV/c) in case of electrons and 0.85 GeV/c (0.75 GeV/c) in case of muons. We also apply an upper lepton momentum cut at 2.4 GeV/c in the c.m. frame to reject non-$B\bar{B}$ events. In case of the B^0 candidates, a vertex fit is performed and $D^{*+}\ell^-$ candidates are rejected if the vertex probability is less than 10^{-3}.

In case of B^+ events containing electrons, we attempt bremsstrahlung recovery by searching for photons in a cone of 3° around the electron track. If such a photon is found it is merged with the electron and the sum of the momenta is assumed to be the lepton momentum. For B^0 candidates no bremsstrahlung recovery has been attempted in the preliminary Belle result ([1]), but it is planned to add it at a later stage. For correct calculation of the efficiency, on the generator level $B \rightarrow D^*\ell^-\nu\gamma$ events are accepted as good signal candidates.

5.3   Determination of the B meson rest frame

With the neutrino emitted in the B being invisible to the Belle detector, the B momentum is *a priori* unknown. However, the accurate determination of B rest frame is essential to calculate the kinematic angles defined in Fig. 3.1 with high precision. One solution to this would be to reconstruct both B mesons. This technique is labeled "full reconstruction". However, this approach massively reduces the available statistics, since not only all the tracks emitted in the signal decay but also those emitted by the second B

meson have to be found and measured accurately. Therefore this method was not used here, instead a novel reconstruction approach is used.

5.3.1   Variable $\cos\theta_{B,D^*\ell}$

Due to momentum conservation, the direction of the spatial B momentum in the c.m. frame[2], $\vec{p}_B^{\,*}$, has to lie on a cone around the $(D^*\ell)$-axis. The opening angle $\cos\theta_{B,D^*\ell}$ can be calculated from reconstructable data. This quantity is widely used in analyses (e.g. [9]) and allows to obtain a one-dimensional space of possible directions of the B momentum. We find

$$p_B = p_{D^*} + p_\ell + p_\nu, \tag{5.1}$$

$$p_\nu = p_B - p_{D^*\ell}, \tag{5.2}$$

$$p_\nu^2 \approx 0 = m_B^2 + m_{D^*\ell}^2 - 2E_B E_{D^*\ell} + 2\vec{p}_B \cdot \vec{p}_{D^*\ell}, \tag{5.3}$$

and therefore

$$\cos\theta_{B,D^*\ell} = \frac{2E_B^* E_{D^*\ell}^* - m_B^2 - m_{D^*\ell}^2}{2|\vec{p}_B^{\,*}||\vec{p}_{D^*\ell}^{\,*}|} \; . \tag{5.4}$$

In case of a B emitted from an $\Upsilon(4S)$ event, the energy and the magnitude of the spatial momentum of in the c.m. frame, E_B^* and $|\vec{p}_B^{\,*}|$, are known from the beam energies. E_B^* is half of the c.m. energy and $|\vec{p}_B^{\,*}|$ is $\sqrt{E_B^{*2} - m_B^2}$. The quantities $E_{D^*\ell}^*$, $\vec{p}_{D^*\ell}^{\,*}$ and $m_{D^*\ell}$ are calculated from the reconstructed $D^*\ell$ system.

This cosine is being used to constraint the spatial momentum of the B meson. It is also a powerful discriminator between signal and background. Signal events should strictly lie in the interval $(-1, 1)$, the interpretation of $\theta_{B,D^*\ell}$ as an actual angle is valid here. Due to finite detector resolution about 5% of the signal is reconstructed outside this interval. The background on the other hand does not have this restriction at all and is distributed over a larger domain.

---

[2]Quantities evaluated in the c.m. frame are denoted by an asterisk.

5.3.2   Inclusive information from the remaining event

The novel part of our reconstruction ansatz is now the following. For the best guess of the B direction, we combine the hard kinematic constraint mentioned above with an additional estimate of the c.m. frame B momentum vector. This is achieved by summing the momenta of the remaining particles in the event, which yields the quantity $\vec{p}\,^{*}_{\text{inclusive}}$.

To obtain $\vec{p}\,^{*}_{\text{inclusive}}$, we first apply the following track and cluster selection requirements to particles which have not been associated with the $(D^{*}\ell)$ system: neutral clusters are required to satisfy $E_{\gamma} > 100$ MeV for polar angles with respect to the beam direction $\theta < 32°$, $E_{\gamma} > 150$ MeV for $\theta > 130°$ and $E_{\gamma} > 50$ MeV in the barrel region in between; the impact parameter cuts for charged tracks are $\Delta r < 20$ cm and $\Delta z < 100$ cm for $p_{\text{T}} < 0.25$ GeV$/c$, $\Delta r < 15$ cm and $\Delta z < 50$ cm for $p_{\text{T}} < 0.5$ GeV$/c$, and $\Delta r < 10$ cm and $\Delta z < 20$ cm for $p_{\text{T}} > 0.5$ GeV$/c$. We exclude duplicated tracks by selecting pairs of charged tracks with $p_{\text{T}} < 275$ MeV$/c$, momentum difference $\Delta p < 100$ MeV$/c$ and relative angle smaller than $15°$ or larger than $165°$. If such a pair is found, we remove the track with smaller value of $(5\Delta r)^2 + (\Delta z)^2$.

Then, we compute $\vec{p}_{\text{inclusive}}$ in the lab. frame by summing the 3-momenta of all the particles passing the criteria discussed above (denoted by the summation index i),

$$\vec{p}_{\text{inclusive}} = \vec{p}_{\text{HER}} + \vec{p}_{\text{LER}} - \sum_{i} \vec{p}_{i} \,, \tag{5.5}$$

where the indices HER and LER correspond to the colliding beams. The energy component of the inclusive four-momentum is chosen such that when transforming this vector into the c.m. frame we obtain the nominal B energy, which is $E^{*}_{B} = \sqrt{s}/2$. Note that we do not make any mass assumption for the charged particles.
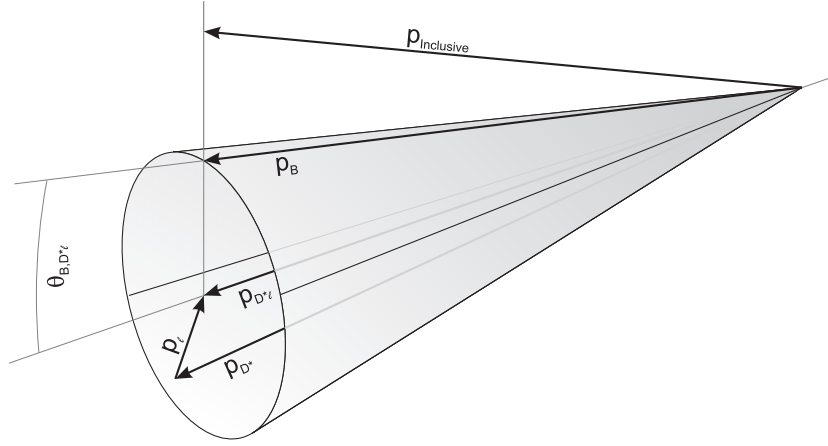
Figure 5.3: Illustration of the reconstruction of the direction of the spatial B momentum. Refer to the text for details.

5.3.3   Best B selection

Finally, we choose the direction on the cone that minimizes the difference to $\vec{p}^{\,*}_{\text{inclusive}}$, as illustrated in Fig. 5.3. This procedure is equivalent to a simple rotation of the spatial $D^*\ell$ momentum in the plane formed by $\vec{p}^{\,*}_{D^*\ell}$ and $\vec{p}^{\,*}_{\text{inclusive}}$.

5.4   Background estimation

The accurate estimation of background underlying the reconstructed signal events is crucial to obtain accurate values for $\mathcal{F}_1|V_{cb}|$ as well as the form factors of the investigated decays. These backgrounds can be investigated by either real data or Monte Carlo simulation.

One possible source for background comes from $e^+e^- \to q\bar{q}$ events, where q is one of u, d, s or c quarks. To investigate this component real data which has been recorded about 60 MeV below the $\Upsilon(4S)$ resonance can be used. This sample cannot contain any B mesons and is therefore ideally suited to investigate the decay of mesons containing only the lighter quarks.

Backgrounds due to B meson decays have to be investigated using simula-

tions. The numbers of simulated events are based on a fixed set of numerical values used for branching ratios of various decays, some of which are no longer in agreement with the current world averages reported by the Particle Data Group [18]. Recreating the entire sample of simulated events is out of the question due to time and computing power constraints.

One efficient way to counter this kind of inaccuracy is to determine the normalization of various background components in a fit to real data. For this purpose, statistical fluctuations have to considered in both the real data and the simulated data sample. Within the ROOT frame work [66] the `TFractionFitter` class, which is based on the `HMCMLL` algorithm reported in Ref. [67], is excellently suited for this purpose.

Additionally, several corrections based on dedicated studies performed by the Belle collaboration are applied. For muon events, the shape of the fake lepton background is corrected by the ratio of the pion fake rate in the experimental data over the same quantity in the Monte Carlo. Additionally, the lepton identification efficiency is reweighted to cope with deviations between simulated and observed lepton abundancies.

In all fits, the continuum normalization is fixed to the on-to-off-resonance luminosity ratio, corrected for the $1/s$ dependence of the $e^+e^- \rightarrow q\bar{q}$ cross-section. From Bhaba ($e^+e^- \rightarrow e^+e^-$) events, the accuracy of this ratio can be determined to be 1.5%. The normalization of the fake lepton component has also been fixed to the MC expectations, since the fit failed to determine this small background contribution reliably. For the uncertainty in this component a conservative value of 30% is assumed.

5.4.1 B^0 background estimation

The background contained in the selected B^0 events can be attributed to the following six sources:

- continuum: any candidate reconstructed in a non-$\Upsilon(4S)$ event
- fake D^*: the D^* candidate is misreconstructed; the lepton candidate is

an actual electron or muon

- fake lepton: the charged lepton candidate is fake; the D^* candidate might be fake or not

- uncorrelated background: the D^* and the lepton stem from different B mesons.

- D^{**}: background from $B \to \bar{D}^{**}\ell^+\nu$ decays with $\bar{D}^{**} \to D^*\pi$ or $B \to D^*\pi\ell^+\nu$ non-resonant

- correlated background: background from other processes in which the D^* and the lepton stem from the same B meson, $e.g$, $B^0 \to D^{*-}\tau^+\nu$, $\tau^+ \to \mu^+\nu\nu$

The fit is performed in the one dimensional $\cos\theta_{B,D^*\ell}$ distribution (Eq. 5.4). As stated above, this distribution is a powerful discriminator between signal and background, since the shapes differ between these various contributions. Fig. 5.4-5.5 show plots of the results of the fit using the `TFractionFitter` class, which is executed separately for each subsample ($K\pi, e$; $K\pi, \mu$; $K3\pi, e$; $K3\pi, \mu$). Agreement between data and the recalibrated Monte Carlo distributions is excellent. After this fit is performed, the final analysis cut $|\cos\theta_{B,D^*\ell}| < 1$ is applied. Table 5.1 shows the signal purity and the fractions of the background components of the events passing all reconstruction and analysis cuts for each channel.
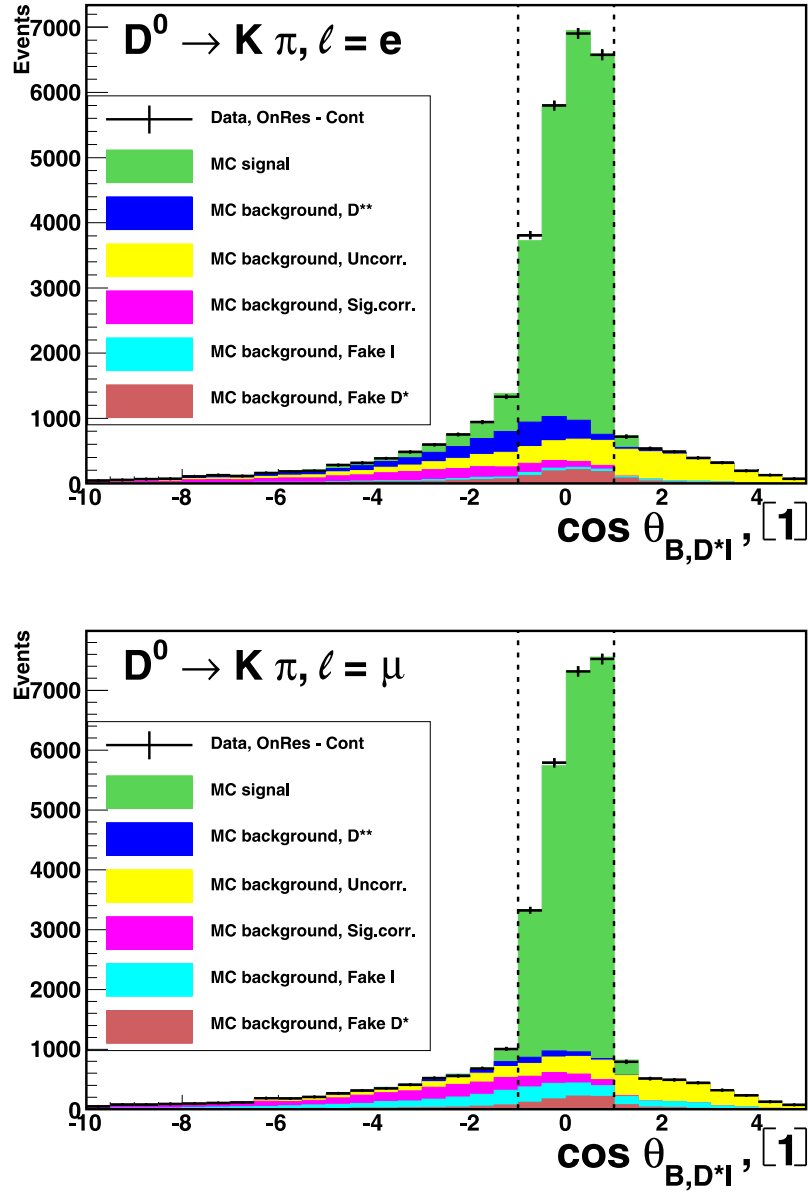
Figure 5.4: Result of the fit to the $\cos\theta_{B,D^*\ell}$ distributions (Eq. 5.4) in the B^0 analysis, $K\pi, e$ and $K\pi, \mu$ sub-samples. The dashed line indicates the final analysis cut, $|\cos\theta_{B,D^*\ell}| < 1$.
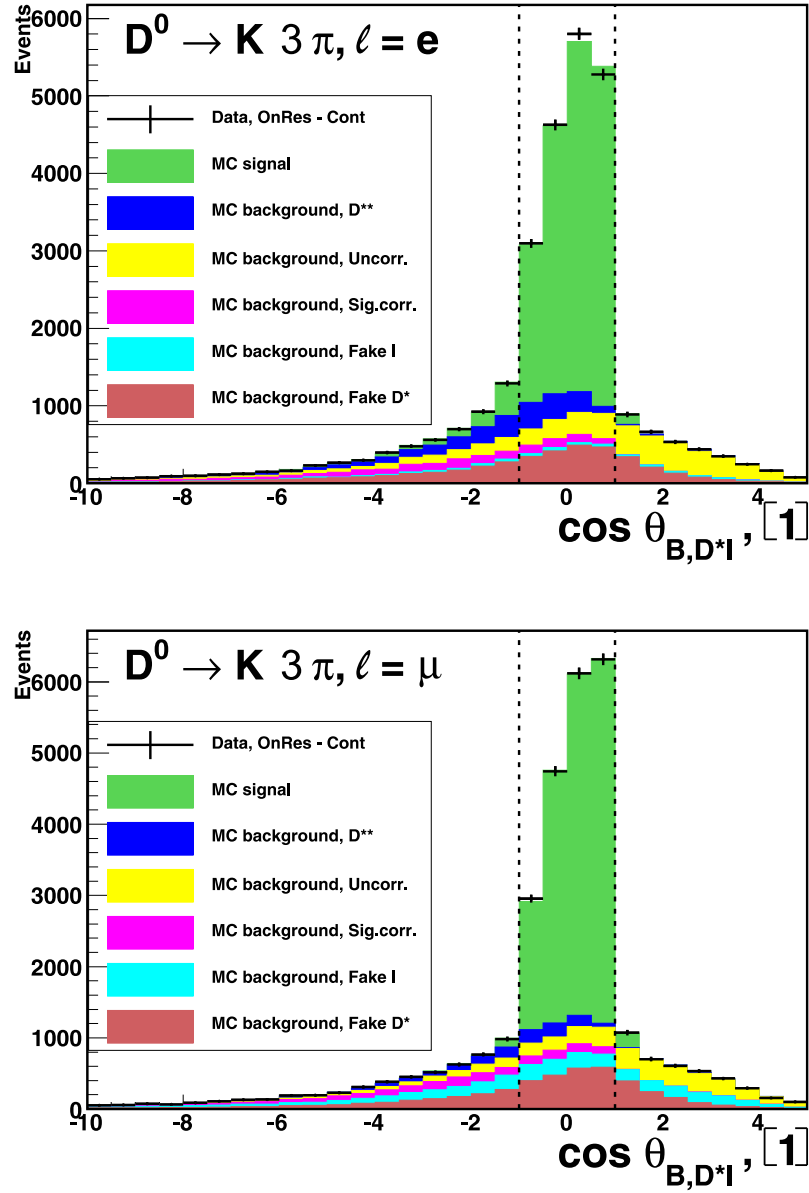
Figure 5.5: Same as Fig. 5.4 for the B^0 analysis, $K3\pi, e$ and $K3\pi, \mu$ sub-samples.

sample	$K\pi, e$	$K\pi, \mu$	$K3\pi, e$	$K3\pi, \mu$
Raw yield	23938	25057	19725	21156
Signal events	19380 ± 276	20278 ± 285	14405 ± 614	15281 ± 559
B^0 signal	$(80.96 \pm 1.15)\%$	$(80.93 \pm 1.14)\%$	$(73.03 \pm 3.11)\%$	$(72.23 \pm 2.64)\%$
Signal correlated	$(1.69 \pm 0.27)\%$	$(2.42 \pm 0.29)\%$	$(2.04 \pm 0.70)\%$	$(2.25 \pm 0.60)\%$
D^{**}	$(4.73 \pm 0.87)\%$	$(1.24 \pm 0.85)\%$	$(5.21 \pm 1.18)\%$	$(2.85 \pm 1.10)\%$
Uncorrelated	$(5.36 \pm 0.28)\%$	$(4.38 \pm 0.30)\%$	$(5.42 \pm 0.58)\%$	$(4.17 \pm 0.55)\%$
Fake ℓ	0.68 % (fixed)	3.62% (fixed)	0.72% (fixed)	4.04% (fixed)
Fake D^*	2.96% (fixed)	2.91% (fixed)	$(8.78 \pm 2.64)\%$	$(9.63 \pm 2.15)\%$
Continuum	3.62% (fixed)	4.51% (fixed)	4.81% (fixed)	4.87% (fixed)

Table 5.1: The signal and background fractions for selected $B^0 \to D^{*-}\ell^+\nu$ events within the signal window $|\cos\theta_{B,D^*\ell}| < 1$.

5.4.2 B^+ background estimation

In case of B^+ candidates, background contributions due to D^* misidentification are significantly higher than in the B^0 case. We therefore add one additional background component compared to the set defined above and consider backgrounds from the following seven sources:

- continuum: any candidate reconstructed in a non-$\Upsilon(4S)$ event,

- fake D^0: the D^0 candidate has been misreconstructed,

- combinatoric D^{*0}: the D^{*0} candidate is misreconstructed, however the D^0 candidate is identified correctly,

- fake lepton: the lepton has been misidentified but the D^{*0} is reconstructed properly,

- uncorrelated background: the D^{*0} and the lepton stem from different B mesons,

- D^{**}: background from $B \to \bar{D}^{**}\ell^+\nu$ decays with $\bar{D}^{**} \to \bar{D}^{*0}\pi$ or $B \to \bar{D}^{*0}\pi\ell^+\nu$ non-resonant, and

- correlated background: background from other processes in which the D^{*0} and the lepton stem from the same B meson, $e.g,$ $B^+ \to \bar{D}^{*0}\tau^+\nu$, $\tau^+ \to \mu^+\nu\nu$.

We perform the fit in the two-dimensional distribution $\cos\theta_{B,D^*\ell}$ vs. Δm. The variable $\cos\theta_{B,D^*\ell}$ defined in Section 5.3.1 again proves to be a good discriminator between signal and background. Additionally, the invariant mass difference between the D^* and the D^0 candidate, $\Delta m = m_{D^*} - m_{D^0}$, allows to precisely calibrate background components containing a misidentified D^* candidate. Components containing correctly reconstructed D^* mesons show a pronounced peak in the Δm distribution, while the other components also contribute to Δm side bands.

Fig. 5.6-5.9 show plots of the results of the fit using the `TFractionFitter` class. Again, the fit is executed separately for each subsample ($K\pi, e$; $K\pi, \mu$;

$K3\pi, e$; $K3\pi, \mu$). The determination of the D^{**} and signal correlated back-grounds works reliably in the two $D^0 \to K^-\pi^+$ modes, but fails in the three pion channels. In these cases we fix the data to MC ratio to the value found in the former channels. We assume the relative uncertainty found in the $K\pi$ modes.

The final analysis requirement applied after this background calibration reads: $|\cos\theta_{B,D^*\ell}| < 1$ and 0.140 GeV/$c^2 < \Delta m < 0.1445$ GeV/c^2. Table 5.2 shows the signal purity and the fractions of the background components of the events passing all reconstruction and analysis cuts for each channel.
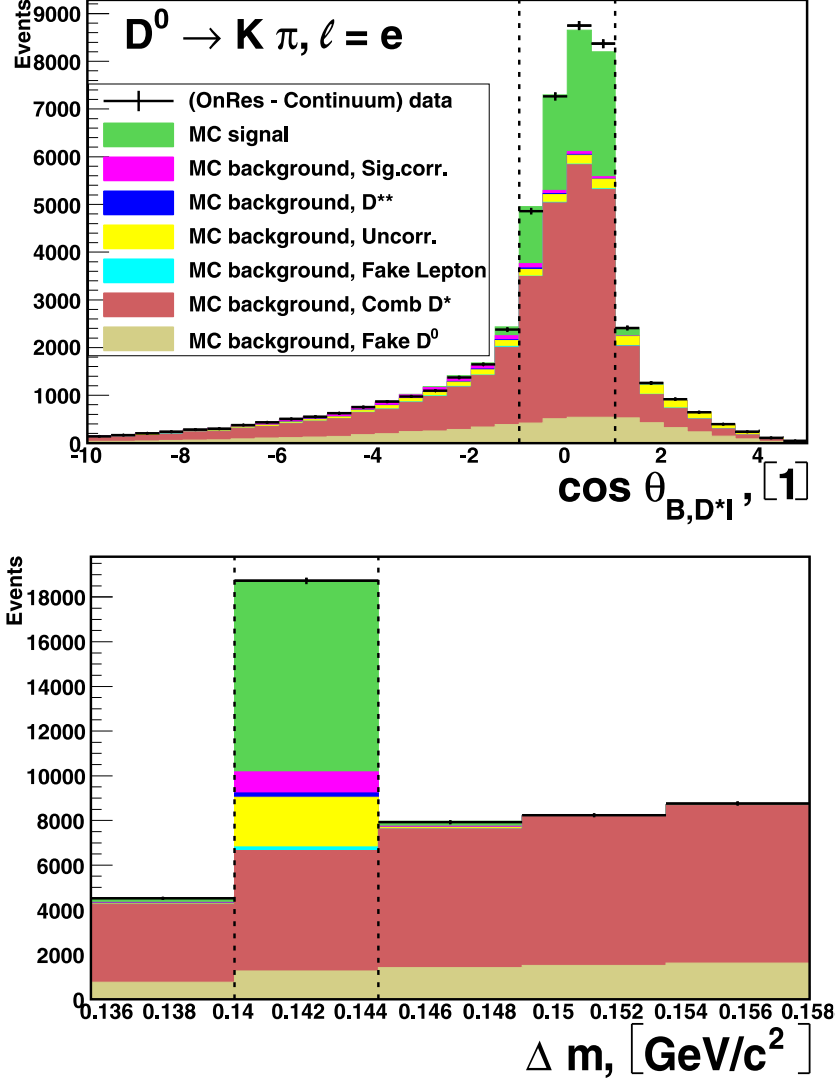
Figure 5.6: Result of the fits to the $\cos\theta_{B,D^*\ell}$ (Eq. 5.4) vs. Δm distributions in the B^+ analysis, $K\pi, e$ sub-sample. The projections in $\cos\theta_{B,D^*\ell}$ and Δm are shown. The dashed line indicates the final analysis cuts, $|\cos\theta_{B,D^*\ell}| < 1$ and 0.140 GeV/$c^2 < \Delta m < 0.1445$ GeV/c^2.
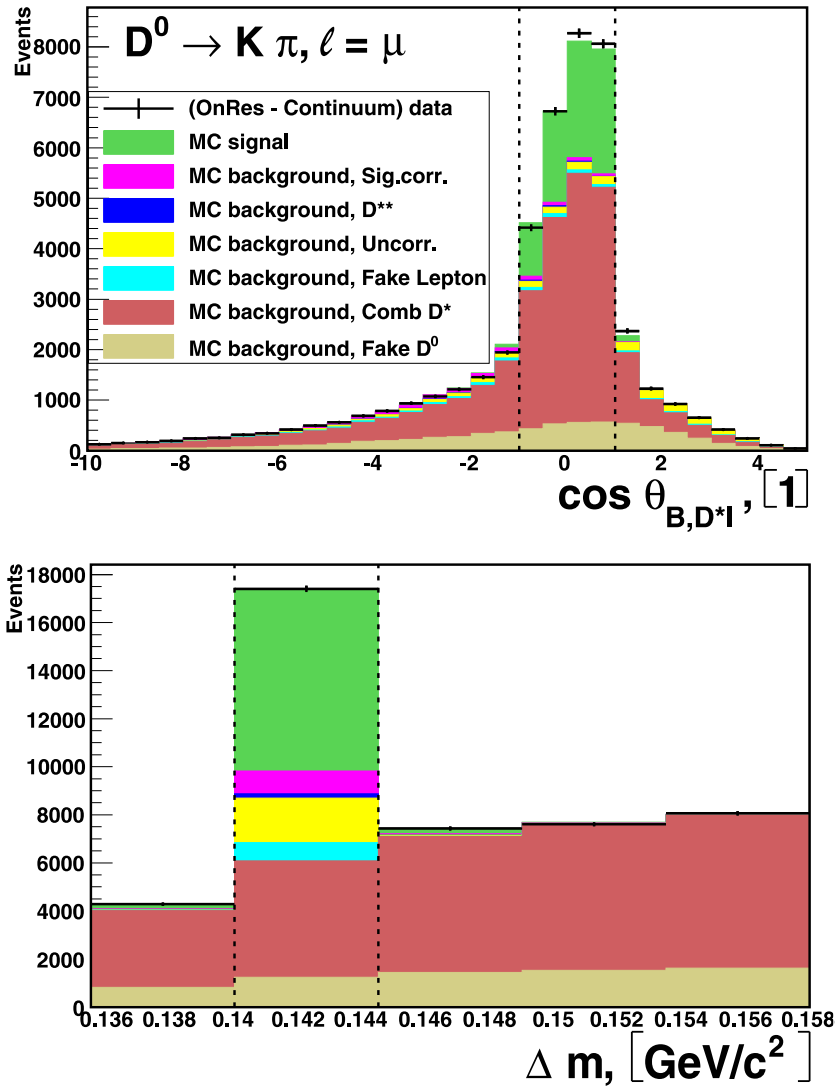
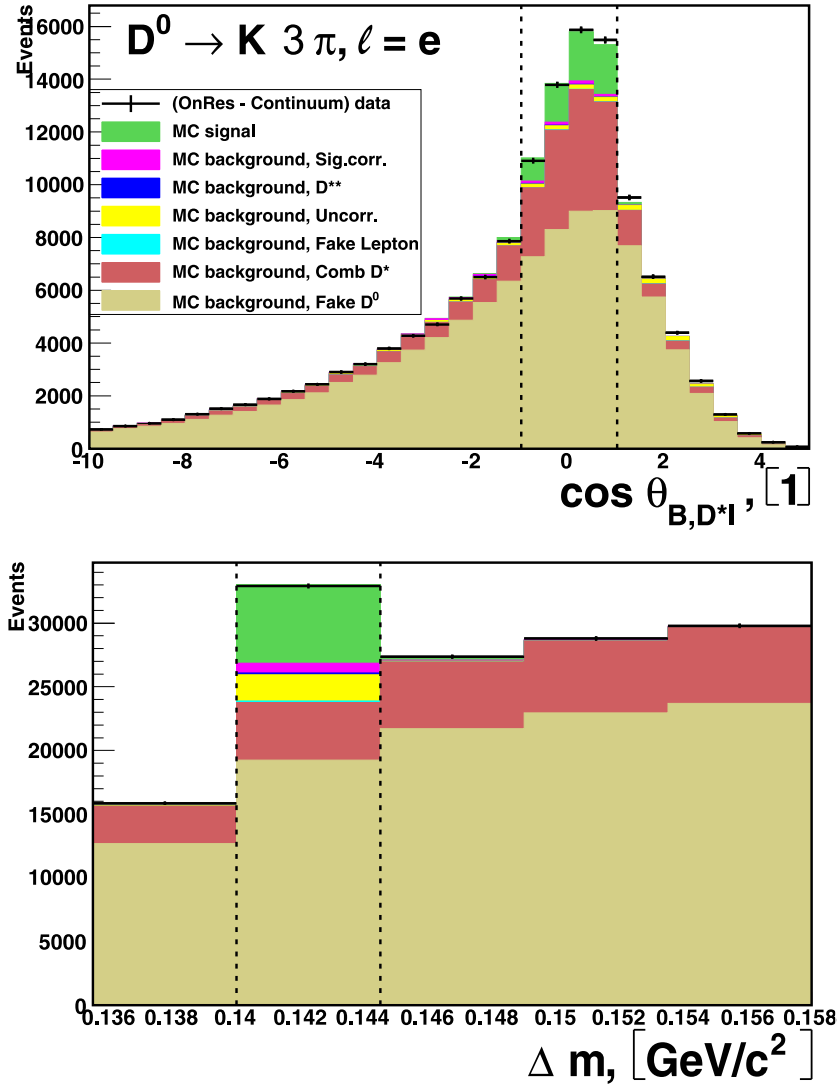Figure 5.7: Same as Fig. 5.6 for the B^+ analysis, $K\pi, \mu$ sub-sample.

Figure 5.8: Same as Fig. 5.6 for the B^+ analysis, $K3\pi, e$ sub-sample.
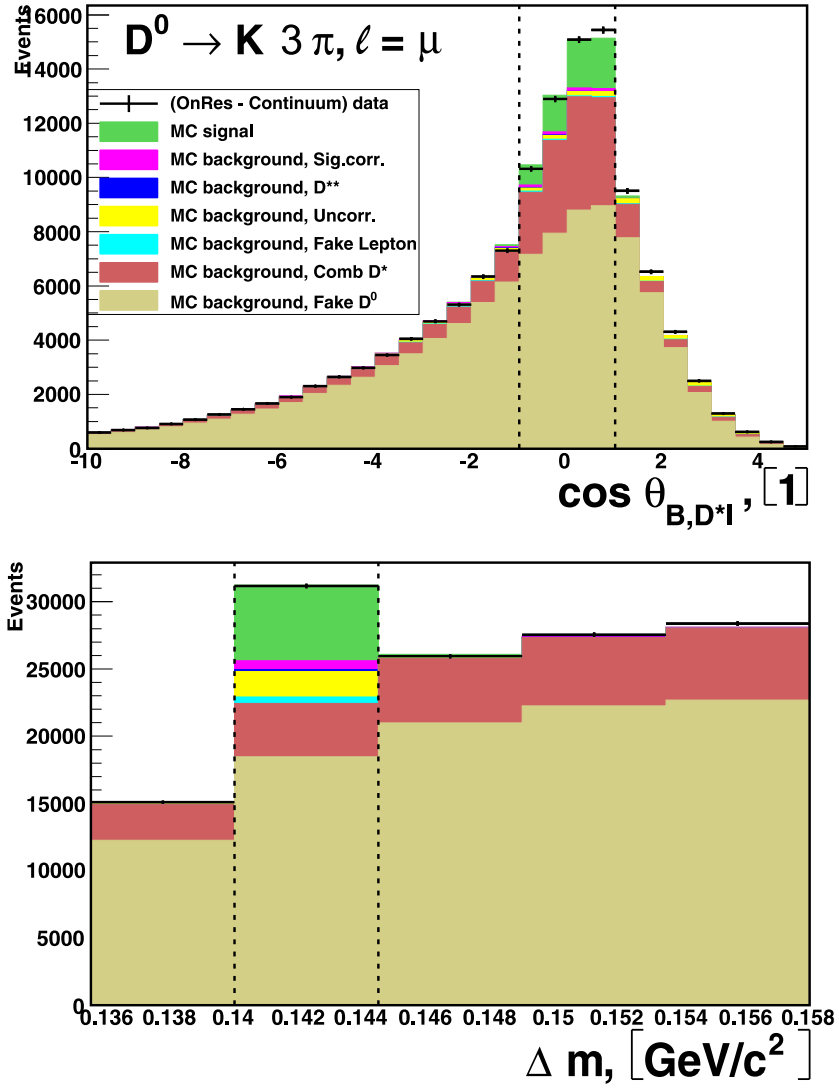
Figure 5.9: Same as Fig. 5.6 for the B^+ analysis, $K3\pi, \mu$ sub-sample.

	$K\pi, e$	$K\pi, \mu$	$K3\pi, e$	$K3\pi, \mu$
Raw yield	13035	12262	16989	16350
Signal events	8133 ± 205	7447 ± 201	5987 ± 229	5539 ± 222
B^+ signal	$(62.39 \pm 1.57)\%$	$(60.73 \pm 1.64)\%$	$(35.24 \pm 1.35)\%$	$(33.88 \pm 1.36)\%$
Signal correlated	$(1.27 \pm 0.31)\%$	$(1.46 \pm 0.32)\%$	$(1.16 \pm 0.26)\%$	$(1.34 \pm 0.31)\%$
D^{**}	$(0.77 \pm 0.98)\%$	$(0.73 \pm 0.98)\%$	$(0.39 \pm 0.50)\%$	$(0.36 \pm 0.47)\%$
Uncorrelated	$(4.97 \pm 0.54)\%$	$(4.25 \pm 0.45)\%$	$(3.48 \pm 0.41)\%$	$(3.30 \pm 0.38)\%$
Fake ℓ	$(0.31 \pm 0.10)\%$	$(1.94 \pm 0.59)\%$	$(0.18 \pm 0.06)\%$	$(0.95 \pm 0.29)\%$
Combinatoric D^{*0}	$(24.76 \pm 0.51)\%$	$(24.30 \pm 0.48)\%$	$(16.35 \pm 0.69)\%$	$(15.19 \pm 0.67)\%$
Fake D^0	$(2.91 \pm 0.25)\%$	$(3.12 \pm 0.23)\%$	$(38.53 \pm 0.50)\%$	$(39.45 \pm 0.51)\%$
Continuum	$(2.63 \pm 0.43)\%$	$(3.46 \pm 0.51)\%$	$(4.68 \pm 0.50)\%$	$(6.14 \pm 0.56)\%$

Table 5.2: The signal and background fractions for selected $B^+ \to \bar{D}^{*0}\ell^+\nu$ events within the signal window $|\cos\theta_{B,D^{*0}\ell}| < 1$ and 0.140 MeV $< \Delta m < 0.1445$ GeV/c^2.

5.5 Kinematic variables

As stated in section 3.5, the investigation of the distributions in the four kinematic variables w, $\cos\theta_\ell$, $\cos\theta_V$ and χ allows to separate the effects due to QCD from the properties of the electro-weak decay $b \to cW$. The definition of the three kinematic angles is shown again in Fig. 5.10. Having calculated the B meson momentum and thus the B rest frame, obtaining the required variables is possible by boosting the momenta of the reconstructed particles into the respective rest frames.

Since the neutrino cannot be detected in a typical collider experiment, the spatial momentum of the W boson, $\vec{p}_W$, cannot be determined directly. Therefore the W rest frame is a priori unknown. However, the energy of the W boson is given by $E_W = E_B - E_{D^*}$ and in the B meson rest frame, the W and the D^* meson are emitted back to back. Measurement of the D^* four-momentum and knowledge of the energy of the B meson is therefore sufficient for calculation of all four kinematic variables.

5.5.1 Calculation of the kinematic variables

The easiest way to calculate the variable $w = (p_B)_\mu (p_{D^*})^\mu / m_B m_{D*}$, which is a linear function of the momentum transfer q^2, is to transform the momentum of the D^* candidate into the B rest frame and to evaluate[3],

$$w = \frac{E'_{D*}}{m_{D*}}. \tag{5.6}$$

As defined in section 3.5 and Fig. 5.10, θ_ℓ is measured in the rest frame of the W boson and gives the polar angle between the charged lepton ℓ and the direction opposite to the spatial momentum of the vector meson D^*. Similarly, θ_V is defined in the D^* rest frame and defines the polar angle between the meson D^0 and the direction opposite to the W boson. Therefore

---

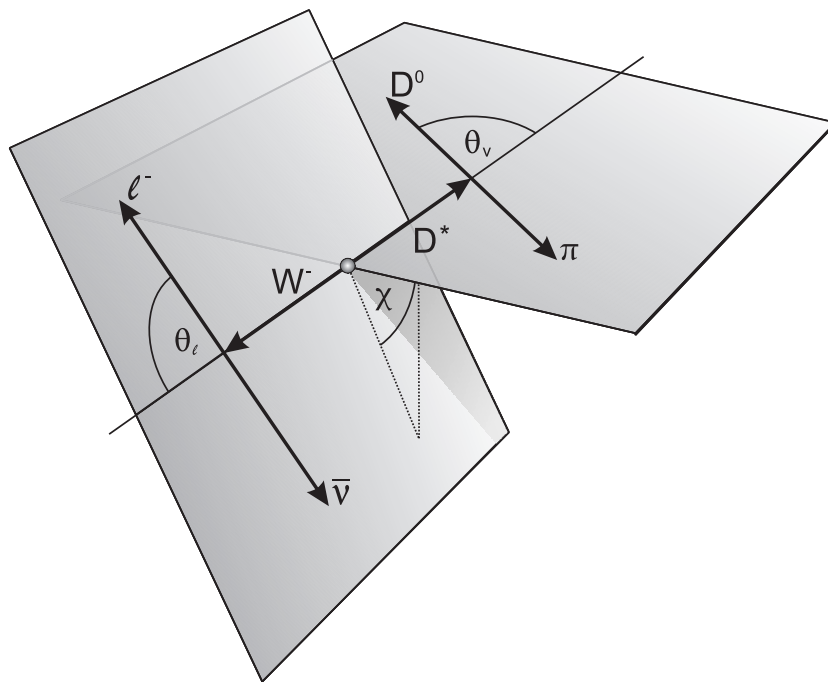[3]Properties denoted with a prime are given in the B meson rest frame

Figure 5.10: Definition of the angles θ_ℓ, θ_V and χ. It is equally valid for both the decays $B^0 \to D^{*-}\ell^+\nu_\ell$, $D^{*-} \to \bar{D}^0\pi_s^-$ and $B^- \to \bar{D}^{*0}\ell^+\nu_\ell$, $\bar{D}^{*0} \to \bar{D}^0\pi_s^0$.
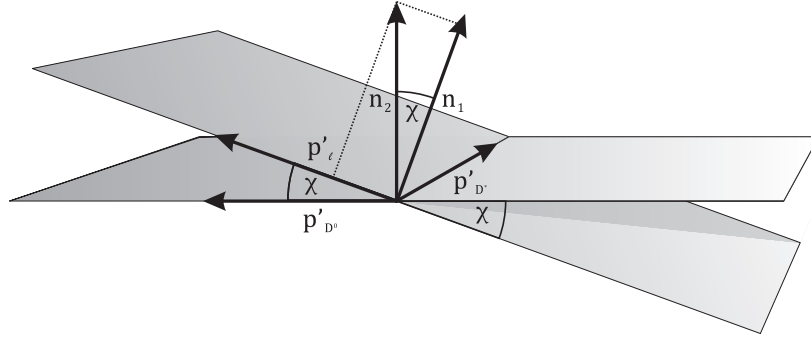
Figure 5.11: Schematic for the calculation of the dihedral angle χ.

we find

$$\cos\theta_\ell = -\frac{\vec{p}_{D^*}^{(W)} \cdot \vec{p}_\ell^{(W)}}{|\vec{p}_{D^*}^{(W)}||\vec{p}_\ell^{(W)}|}, \ \cos\theta_V = -\frac{\vec{p}_W^{(D^*)} \cdot \vec{p}_{D^0}^{(D^*)}}{|\vec{p}_W^{(D^*)}||\vec{p}_{D^0}^{(D^*)}|}. \tag{5.7}$$

where $x^{(W)}$ and $x^{(D^*)}$ denote quantities boosted into the W and D^* rest frame, respectively.

The variable χ measures the angle between the two planes formed by the decays of the W boson and the D^* meson, as shown in Fig. 5.10. This variable varies in the interval $[-\pi, \pi[$. It is therefore important to not only calculate the modulus of this angle, but the sign as well.

As can be seen in Figs. 5.10 and 5.11, the normal vectors of the two planes P_1 (formed by the spatial momentum of the D^* and the ℓ candidates) and P_2 (D^* and D^0) are labeled[4]

$$\vec{n}_1 = \frac{\vec{p}_{D^*}' \times \vec{p}_\ell'}{|\vec{p}_{D^*}'||\vec{p}_\ell'|}, \tag{5.8}$$

$$\vec{n}_2 = \frac{\vec{p}_{D^*}' \times \vec{p}_{D^0}'}{|\vec{p}_{D^*}'||\vec{p}_{D^0}'|}. \tag{5.9}$$

The product $\vec{n}_1 \cdot \vec{n}_2$ measures the component of $\vec{n}_2$ perpendicular to the plane P_1, while the product between $\vec{n}_2$ and any vector in the plane, e.g. $\vec{p}_\ell' \cdot \vec{n}_2$, gives the size of the normal projection of $\vec{n}_2$ into the plane P_1. These quantities are proportional to the cosine and the sine of the angle χ, respectively.

---

[4]As mentioned above, properties denoted with a prime are given in the B meson rest frame.

We therefore find,

$$\cos\chi = \frac{(\vec{p}\,'_{D*} \times \vec{p}\,'_{\ell}) \cdot (\vec{p}\,'_{D*} \times \vec{p}\,'_{D^0})}{|\vec{p}\,'_{D*}|\,|\vec{p}\,'_{\ell}|\,|\vec{p}\,'_{D*}|\,|\vec{p}\,'_{D^0}|}, \tag{5.10}$$

$$\cos\left(\frac{\pi}{2} - \chi\right) = \sin\chi = \frac{\vec{p}\,'_{\ell} \cdot (\vec{p}\,'_{D*} \times \vec{p}\,'_{D^0})}{|\vec{p}\,'_{\ell}|\,|\vec{p}\,'_{D*}|\,|\vec{p}\,'_{D^0}|}, \tag{5.11}$$

and thus obtain,

$$\chi = \arctan\left(\frac{|\vec{p}\,'_{D*}|\;\vec{p}\,'_{\ell} \cdot (\vec{p}\,'_{D*} \times \vec{p}\,'_{D^0})}{(\vec{p}\,'_{D*} \times \vec{p}\,'_{\ell}) \cdot (\vec{p}\,'_{D*} \times \vec{p}\,'_{D^0})}\right). \tag{5.12}$$

This equation maps to the entire domain $\chi \in [-\pi, \pi[$, as required.

5.5.2 Resolutions in the kinematic variables

In general, the reconstructed value of any kinematic variable, v^{rec}, will not be identical to the true value, v^{true}. Rather we will find a distribution with a central value which should be close to the true value and a width which is called the resolution $\delta = v^{rec} - v^{true}$. The resolutions which can be obtained by the procedures described above have been estimated using about 20 fb^{-1} of Monte Carlo simulated data. We find symmetric distributions centered on the true value and obtain excellent values in the resolutions, which are nearly identical in the case of B^0 and B^+ reconstruction. For B^0 we find gaussian resolutions of about $\delta_w = 0.021$, $\delta_{\cos\theta_\ell} = 0.049$, $\delta_{\cos\theta_V} = 0.057$ and $\delta_\chi = 6.46°$, while for B^+ the numbers are about $\delta_w = 0.025$, $\delta_{\cos\theta_\ell} = 0.052$, $\delta_{\cos\theta_V} = 0.047$ and $\delta_\chi = 6.47°$.

Chapter 6

Fit procedures

> *You cannot direct the wind, but you can adjust your sails.*
>
> *Unknown*

6.1 Parametrized fit

In order to extract $\mathcal{F}(1)|V_{cb}|$ and the three form factor parameters ρ^2, $R_1(1)$ and $R_2(1)$, we perform a binned χ^2 fit of the w, $\cos\theta_\ell$, $\cos\theta_V$ and χ distributions over almost the entire phase. Instead of fitting in four dimensions, where we would be massively limited by the available statistics, we fit the four one-dimensional projections of w, $\cos\theta_\ell$, $\cos\theta_V$ and χ. This ensures a sufficiently high abundance of events in each bin, but it also introduces bin-to-bin correlations which have to be accounted for.

6.1.1 Predicted number of events

The distributions in w, $\cos\theta_\ell$, $\cos\theta_V$ and χ are divided into ten bins of equal width. The kinematically allowed values of w are between 1 and ≈ 1.504

(≈ 1.505) in case of B^0 (B^+) decays, but we restrict the w range to values
between 1 and 1.5. In each sub-sample, there are thus 40 bins to be used
in the fit. In the following, we label these bins with a common index i, $i =
1, \ldots, 40$. The bins $i = 1, \ldots, 10$ correspond to the bins of the w distribution,
$i = 11, \ldots, 20$ to $\cos \theta_\ell$, $i = 21, \ldots, 30$ to $\cos \theta_V$ and $i = 31, \ldots, 40$ to the χ
distribution.

The predicted number of events N_i^{th} in the bin i is given by

$$N_i^{\text{th}} = N_B \mathcal{B}(D^* \to D^0 \pi_s) \mathcal{B}(D^0 \to K^- \pi^+, K^- \pi^+ \pi^+ \pi^-) \tau_B \Gamma_i \qquad (6.1)$$

where N_B is the number of B^0 or B^+ mesons in the data sample. $\mathcal{B}(D^* \to
D^0 \pi)$ stands for the branching ratio of either the D^{*+} or D^{*0} meson. These
values are taken from Ref. [18]. In the $(K\pi, e)$ and $(K\pi, \mu)$ sub-samples
$\mathcal{B}(D^0)$ is $\mathcal{B}(D^0 \to K^- \pi^+)$ [18]. In $(K3\pi, e)$ and $(K3\pi, \mu)$ we define $\mathcal{B}(D^0) =
R_{K3\pi/K\pi} \mathcal{B}(D^0 \to K^- \pi^+)$, with $R_{K3\pi/K\pi}$ a fifth free parameter of the fit.
Finally, τ_{B^+} is the B^+ lifetime [18].

Γ_i is the width obtained by integrating Eq. 3.27 in the kinematic variable
corresponding to the bin i from the lower to the upper bin boundary, while the
other kinematic variables are integrated over their full range. This integration
is numerical in the case of w and analytic for the other variables.

The expected number of events N_i^{exp} is related to N_i^{th} as follows

$$N_i^{\text{exp}} = \sum_{j=1}^{40} \left(R_{ij} \epsilon_j N_j^{\text{th}} \right) + N_i^{\text{bkgrd}} \ . \qquad (6.2)$$

Here, the efficiency ϵ_j is the probability that an event generated in the bin j
is reconstructed and passes all analysis cuts, and R_{ij} is the detector response
matrix, which gives the probability that an event generated in the bin j is
observed in the bin i. Both quantities are calculated using MC simulation.
N_i^{bkgrd} is the number of expected background events, estimated as described
in Sect. 5.4.

6.1.2   Calculation of the covariance matrix

Next, we calculate the variances σ_i^2 of N_i^{exp}, which represent the diagonal elements of the covariance matrix C. We consider the following contributions: the uncertainty in N_i^{th} (poissonian); fluctuations related to N repetitions of the yes/no experiment with known success probability ϵ_i (binomial); a similar contribution to the variance related to R_{ij} (multinomial); and the uncertainty in the background contribution N_i^{bkgrd}. This yields the following expression for $\sigma_i^2 = C_{ii}$,

$$
\sigma_i^2 = \sum_{j=1}^{40} \left[R_{ij}^2 \epsilon_j^2 N_j^{\mathrm{th}} + R_{ij}^2 \frac{\epsilon_j(1-\epsilon_j)}{N_{\mathrm{data}}}(N_j^{\mathrm{th}})^2 + \frac{R_{ij}(1-R_{ij})}{N'_{\mathrm{data}}}\epsilon_j^2(N_j^{\mathrm{th}})^2 + \right.
$$
$$
\left. + R_{ij}^2 \frac{\epsilon_j(1-\epsilon_j)}{N_{\mathrm{MC}}}(N_j^{\mathrm{th}})^2 + \frac{R_{ij}(1-R_{ij})}{N'_{\mathrm{MC}}}\epsilon_j^2(N_j^{\mathrm{th}})^2 \right] +
$$
$$
+ \sigma^2(N_i^{\mathrm{bkgrd}}) \ . \tag{6.3}
$$

The first term is the poissonian uncertainty in N_i^{th}. The second and third terms are the binomial and multinomial uncertainties, respectively, related to the finite real data size, where N_{data} (N'_{data}) is the total number of decays (the number of reconstructed decays) into the final state under consideration ($K\pi$ or $K3\pi$, e or μ) in the real data. The quantities ϵ_i and R_{ij} are calculated from MC samples (N_{MC} and N'_{MC}); the uncertainties corresponding to the finite site of the sample are estimated by the fourth and fifth terms. Finally, the last term is the background contribution $\sigma^2(N_i^{\mathrm{bkgrd}})$, calculated as the sum of the different background component variances. For each background component defined in Sect. 5.4 we estimate its contribution by linear error propagation of the scale factor and the error determined by the procedure described above.

In each sub-sample we calculate the off-diagonal elements of the covariance matrix C_{ij} as

$$
C_{ij} = N p_{ij} - N p_i p_j, \forall i \neq j \tag{6.4}
$$

where p_{ij} is the relative abundance of the bin (i, j) in the two-dimensional histogram obtained by plotting the kinematic variables against each other,

p_i, p_j are the relative numbers of entries in the 1-dimensional distribution, and N is the size of the sample. Covariances are calculated for the signal and the different background components, and added with appropriate normalizations. The derivation of this ansatz can be found in Chapter A.

6.1.3 χ^2 ansatz

The covariance matrix is calculated individually for each channel, labelling the four sub-samples ($K\pi$ or $K3\pi$, e or μ) with the index k, and inverted numerically within ROOT [66]. The sub-sample χ^2 functions are calculated,

$$\chi_k^2 = \sum_{i,j} (N_{i,k}^{\mathrm{obs}} - N_{i,k}^{\mathrm{exp}}) C_{ij,k}^{-1} (N_{j,k}^{\mathrm{obs}} - N_{j,k}^{\mathrm{exp}}) \ , \tag{6.5}$$

where N_i^{obs} is the number of events observed in bin i in the data. We sum the four functions $k \in \{K\pi, e; K\pi, \mu; K3\pi, e; K3\pi, \mu\}$ and minimize the global χ^2 numerically using MINUIT [68].

Due to the off-diagonal elements in the covariance matrix C, this double sum will in general not reduce to the single sum of a simple χ^2 ansatz. This is only the case when considering statistically independent variables, where Eq. 6.5 becomes the sum of a total of four primitive χ^2 functions. The procedure is then identical to executing four separate χ^2 fits to each of the one-dimensional distributions.

As stated above, the reconstructed events are divided into the four reconstructed channels and into 10 bins in each of the four distributions. If we consider only one single sub-channel we determine 4 free parameters. If we fit the total sample, we have again 40 bins per channel and try to determine a total of 5 free parameters. Therefore, we expect the values calculated according to Eq. 6.5 to be distributed according to a χ^2 distribution with 36 (155) degrees of freedom if we fit one of the sub-samples (the total sample). This also implies that, if the model assumptions are accurate, and we would be able to reproduce the experiment an infinite number of times, the χ^2 probabilities should be distributed according to a uniform distribution. Since we are only able to investigate a limited number of samples, this test cannot be

realized. Instead we can test that none of the samples show an inprobably high χ^2 value (corresponding, e.g. to a χ^2 probability below 10^{-4}), which might imply an inaccurate definition of the central values or errors used in Eq. 6.5.

6.2   Direct test of the parametrization

The fit approach discussed in the previous section relies on the form factor parameterization by Caprini *et al.* [5] and it is worthwhile to check this assumption. We therefore extract the form factor shape through a fit to the w vs. $\cos\theta_V$ distribution of B^+ events. For the former quantity, we consider six bins in the range from 1 to 1.5. For the latter, we have also six bins between -1 and 1. The contribution from events with $w > 1.5$ is fixed to the very small values predicted by the results of the parametrized fit.

6.2.1   Fit parameters

From Eq. 3.27 we can obtain the double differential decay width $\mathrm{d}^2\Gamma/\mathrm{d}w\,\mathrm{d}\cos\theta_V$ by integration over $\cos\theta_\ell$ and χ.

If we define

$$F_\Gamma = \frac{3\,G_F^2\,(m_B - m_{D^*})^2\,m_{D^*}^3}{4^5\pi^4} \tag{6.6}$$

and

$$\gamma^{\pm\pm}(w) = c(w)|V_{cb}|^2 \frac{1 - 2wr - r^2}{(1-r)^2}\left\{1 \mp \sqrt{\frac{w-1}{w+1}}R_1(w)\right\}^2, \tag{6.7}$$

$$\gamma^{00}(w) = c(w)|V_{cb}|^2\left\{1 + \frac{w-1}{1-r}\left(1 - R_2(w)\right)\right\}^2, \tag{6.8}$$

where $c(w) = \sqrt{w^2 - 1}(w+1)^2 h_{A_1}^2(w)$, the double differential width becomes

$$\frac{\mathrm{d}^2\Gamma(B^+ \to \bar{D}^{*0}\ell^+\nu_\ell)}{\mathrm{d}w\,\mathrm{d}\cos\theta_V} = \frac{16\pi}{3}F_\Gamma\left(\sin^2\theta_V\left(\gamma^{++} + \gamma^{--}\right) + 2\cos^2\theta_V\,\gamma^{00}\right). \tag{6.9}$$

The quantities γ^{kk} correspond to the w-dependence of the different helicity combinations, times kinematic factors. The one-dimensional distribution, as given in Eq. 3.30, depends only on the sum of these three combinations,

$$\frac{\mathrm{d}\Gamma(B^+ \to \bar{D}^{*0}\ell^+\nu_\ell)}{\mathrm{d}w} = \frac{64\pi}{9}F_\Gamma\left(\gamma^{++} + \gamma^{--} + \gamma^{00}\right). \qquad (6.10)$$

The bin contents of the two-dimensional histogram in w vs. $\cos\theta_V$ can be obtained by integration of Eq. 6.9 over the corresponding bin area and considering the reconstruction efficiencies and detector response as described in Eq. 6.2. Each bin content can be given as the linear combination of two linearly independent parts, proportional to Γ^{00} and $\Gamma^{++} + \Gamma^{--}$. The integration of the angular distributions is executed analytically, as described above, the integration with respect to w defines a set of free parameters,

$$\Gamma_i^{kk} = \int\limits_{w_i}^{w_{i+1}} \mathrm{d}w\, \gamma^{kk}, \qquad (6.11)$$

where $w_j = \{w_1, w_2, \ldots, w_7\} = \{1, 13/12, \ldots, 1.5\}$ are the bin boundaries of the 6 bins in w. Additionally we define $\gamma^T = \gamma^{++} + \gamma^{--}$, $\Gamma_i^T = \Gamma_i^{++} + \Gamma_i^{--}$, $\gamma^L = \gamma^{00}$ and $\Gamma^L = \Gamma^{00}$.

We define the χ^2 function $\tilde{\chi}^2_{w,\theta_V} = \sum_{i=1}^{6}\sum_{j=1}^{6}\frac{N_{ij}^{obs}-N^{exp}}{\sigma_{N^{exp}}}$, which depends only on the parameters Γ_i^T and Γ_i^L. Here N^{obs} gives the number of events observed in on-resonance data, N^{exp} the number of expected events, as defined in Eq. 6.2, and $\sigma_{N^{exp}}$ the uncertainty in the expected number of events, as given in Eq. 6.3. This expression is minimized numerically using MINUIT to determine the partial integrals.

Investigation of dedicated sets of toy Monte Carlo showed the reliability of the procedure described above. The results show no indication of a significant bias in either the mean or the errors.

Chapter 7

Results and investigation of systematic uncertainties

> *There is no wealth like knowledge, no poverty like igno-*
> *rance.*

> *Ali ibn Ali-Talib*

The numerical fit described in the previous chapter allows to determine both the central value and the statistical uncertainty for each fit parameter. However, in order to arrive at a presentable result, both the stability of the used method and the dependency of the result on external parameters (like, *e.g.* the B mean lifetime) have to be investigated. From this a systematic uncertainty can be obtained for each parameter. The determination of the systematic error is similar in both analyses, however not entirely identical.

7.1 B^0 analysis

As can be seen in Tab. 5.1, after applying all selection requirements and subtracting backgrounds, $69,345 \pm 377$ signal events are found in the reconstructed B^0 data. Table 7.1 shows the results of the fit to each sub-channel

as well as to the total sample.

The χ^2 values obtained in these fits show good agreement with the statistical expectation. In the two $K3\pi$ channels, the error of the background component containing misidentified D^* mesons is very large, as can be seen in Tab. 5.1. Compared to the procedure described in section 5.4.2, the older method defined in section 5.4.1 is less powerful in discriminating this background from the other components. This results in an overestimation of the error and thus a smaller value of χ^2 in these to fits.

To estimate the systematic uncertainties in the results quoted above, we consider contributions from the following sources: uncertainties in the background component normalizations, uncertainty in the MC tracking efficiency, errors in $\mathcal{B}(D^{*+} \to D^0\pi^+)$ and $\mathcal{B}(D^0 \to K^-\pi^+)$ [69], and uncertainties in the B^0 lifetime [69] and the total number of B^0 mesons in the data sample.

To estimate the uncertainty related to a given background component, we vary the normalization by ± 1 standard deviation of the fit described in Sect. 5.4. The uncertainty in the $D^{**}\ell\nu$ component is inflated by a factor of two to make the amount of $D^{**}\ell\nu$ in each sub-sample consistent. The error in the continuum normalization is taken to be 1.5% as explained earlier.

For the tracking uncertainty, we calculate the track finding error considering only the D^0 decay into $K^-\pi^+$, as the branching fraction for $D^0 \to K^-\pi^+\pi^-\pi^+$ is fitted from data and therefore a possible mismodeling of the tracking efficiency for this mode would be absorbed in $R_{K3\pi/K\pi}$. We thus have four charged tracks. Assuming 1% uncertainty for each track, except for the slow pion from D^{*+} for which we use 2%, and adding these uncertainties linearly. This is the most conservative ansatz and reflects that this systematic error aims to hedge against a possible imperfection in the simulation of the detector. If such an effect would exist, it would impact all charged tracks in a similar fashion, therefore the uncertainties related to each single tracks cannot be independent.

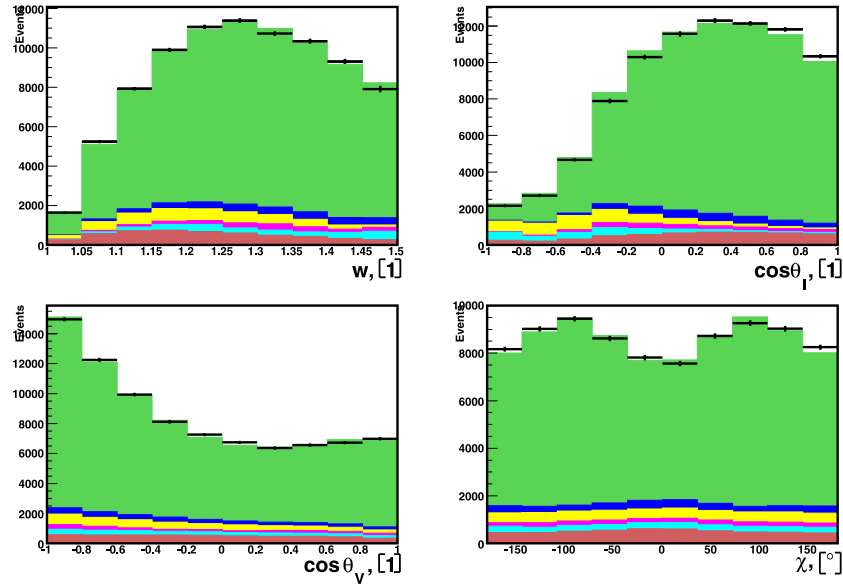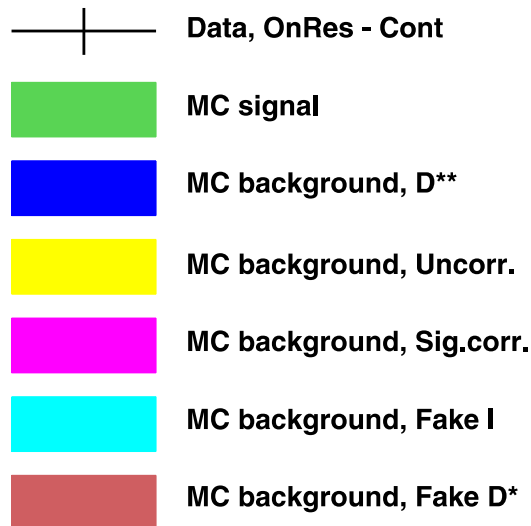The breakdown of the systematic error quoted in Table 7.1 is given in Table 7.3.

Figure 7.1: Result of the fit of the four kinematic variables in the total sample of $B^0 \to D^{*-}\ell^+\nu$ events. (The different sub-samples are added in this plot.) The points with error bars are continuum subtracted on-resonance data. The histograms are the signal and the different background components. The color scheme is explained below.
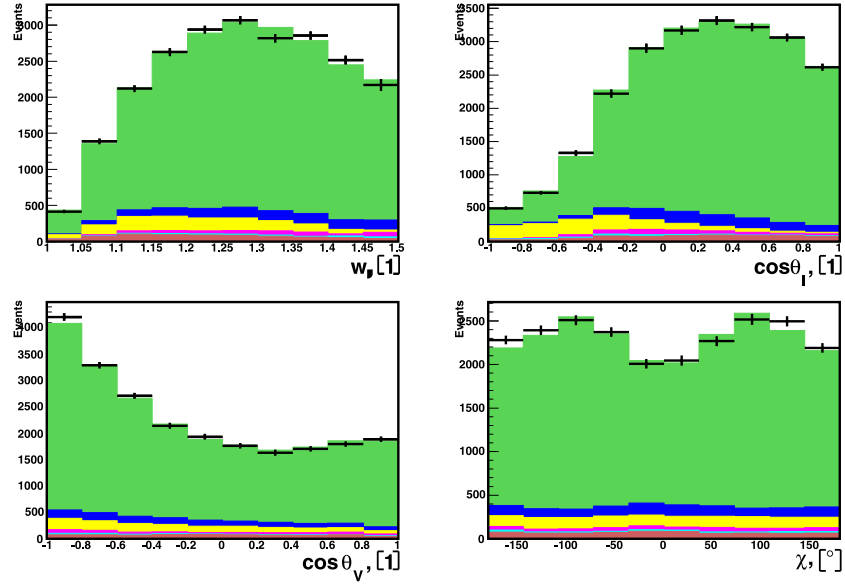
Data, OnRes - Cont

MC signal

MC background, D**

MC background, Uncorr.

MC background, Sig.corr.

MC background, Fake l

MC background, Fake D*

Figure 7.2: Same as Fig. 7.1 for the B^0 analysis, $K\pi, e$ sub-sample.
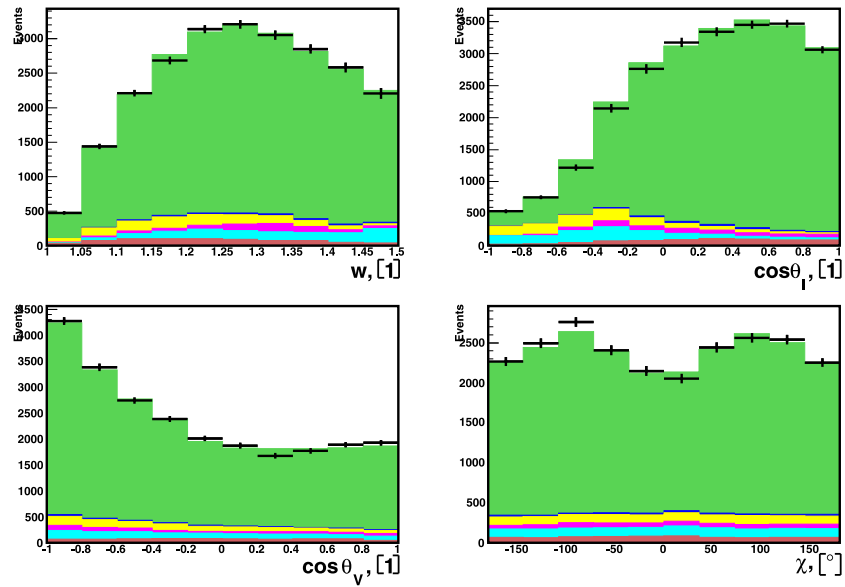
Figure 7.3: Same as Fig. 7.1 for the B^0 analysis, $K\pi, \mu$ sub-sample.
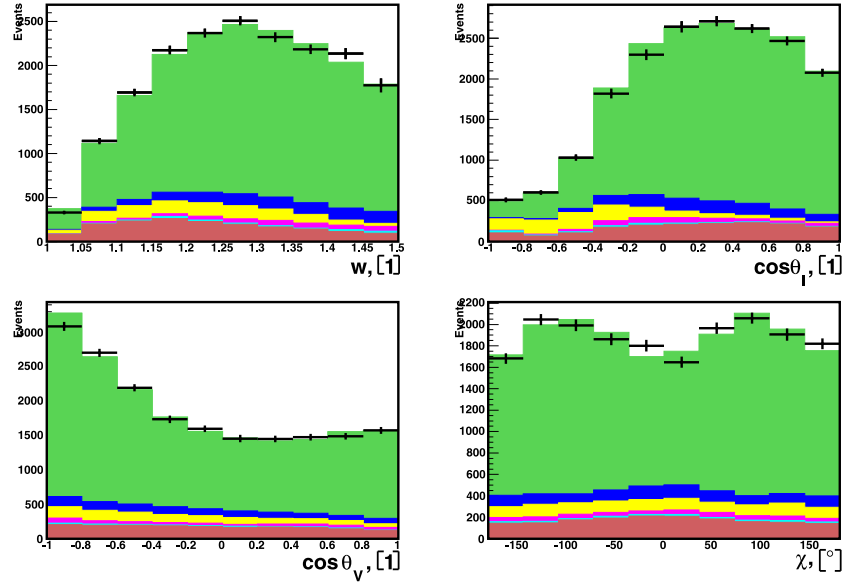
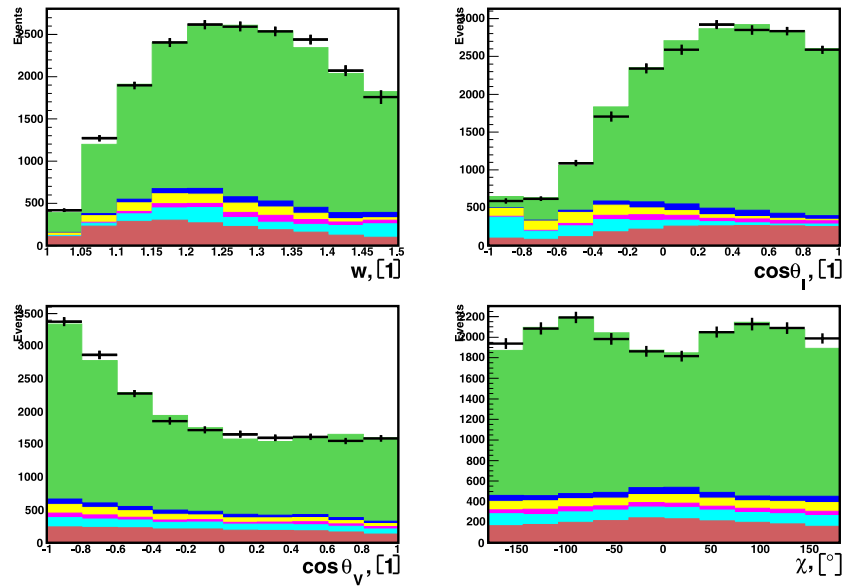Figure 7.4: Same as Fig. 7.1 for the B^0 analysis, $K3\pi, e$ sub-sample.

Figure 7.5: Same as Fig. 7.1 for the B^0 analysis, $K3\pi, \mu$ sub-sample.

sample	$D^0 \to K\pi. \ell = e$	$D^0 \to K\pi. \ell = \mu$	$D^0 \to K3\pi. \ell = e$
ρ^2	$1.329 \pm 0.072 \pm 0.017$	$1.221 \pm 0.075 \pm 0.046$	$1.238 \pm 0.233 \pm 0.053$
$R_1(1)$	$1.455 \pm 0.077 \pm 0.046$	$1.608 \pm 0.087 \pm 0.099$	$1.085 \pm 0.125 \pm 0.044$
$R_2(1)$	$0.782 \pm 0.055 \pm 0.014$	$0.853 \pm 0.055 \pm 0.027$	$0.980 \pm 0.087 \pm 0.027$
$R_{K3\pi/K\pi}$	2.153 (fixed)	2.153 (fixed)	2.153 (fixed)
$\mathcal{B}(B^0 \to D^{*-}\ell^+\nu_\ell)$ (%)	$4.43 \pm 0.03 \pm 0.25$	$4.41 \pm 0.03 \pm 0.26$	$4.42 \pm 0.04 \pm 0.25$
$\mathcal{F}(1)\|V_{cb}\|$ (10^{-3})	$34.3 \pm 0.4 \pm 1.1$	$33.5 \pm 0.4 \pm 1.0$	$35.6 \pm 0.8 \pm 1.3$
χ^2/n.d.f.	29.2/36	37.4/36	19.2/36
$P(\chi^2)$	78.2%	40.4%	99.0%

sample	$D^0 \to K3\pi. \ell = \mu$	Fit to total sample
ρ^2	$1.436 \pm 0.121 \pm 0.062$	$1.293 \pm 0.045 \pm 0.029$
$R_1(1)$	$1.643 \pm 0.163 \pm 0.112$	$1.495 \pm 0.050 \pm 0.062$
$R_2(1)$	$0.842 \pm 0.105 \pm 0.038$	$0.844 \pm 0.034 \pm 0.019$
$R_{K3\pi/K\pi}$	2.153 (fixed)	2.153 ± 0.011
$\mathcal{B}(B^0 \to D^{*-}\ell^+\nu_\ell)$ (%)	$4.47 \pm 0.04 \pm 0.26$	$4.42 \pm 0.03 \pm 0.25$
$\mathcal{F}(1)\|V_{cb}\|$ (10^{-3})	$35.6 \pm 0.7 \pm 1.3$	$34.4 \pm 0.2 \pm 1.0$
χ^2/n.d.f.	17.9/36	138.8/155
$P(\chi^2)$	99.5%	82.0%

Table 7.1: The results of the fits to the sub-samples and the fit result on the total sample of $B^0 \to D^{*-}\ell^+\nu$ events. The first error is statistical, the second is the estimated systematic uncertainty. The breakdown of the systematic uncertainty is given in Table 7.3. All numbers are preliminary.

	$\mathcal{F}(1)|V_{cb}|$	ρ^2	$R_1(1)$	$R_2(1)$
$\mathcal{F}(1)|V_{cb}|$	1.000	0.635	-0.285	-0.220
ρ^2		1.000	0.388	-0.870
$R_1(1)$			1.000	-0.511
$R_2(1)$				1.000

Table 7.2: The statiscal correlation coefficients of $\mathcal{F}_1|V_{cb}|$ and the three form factor parameters in the fit to the full sample of $B^0 \to D^{*-}\ell^+\nu$ events.

	ρ^2	$R_1(1)$	$R_2(1)$	$\mathcal{B}(D^*\ell\nu_\ell)$	$\mathcal{F}(1)|V_{cb}|$
Reconstruction and tracking	—	—	—	-0.221	-0.86
LeptonID	+0.011	+0.022	-0.011	-0.38	-0.097
Norm - Signal Corr.	-0.003	-0.003	+0.007	+0.028	+0.14
Norm - D^{**}	-0.015	-0.038	+0.011	-0.051	-0.25
Norm - Uncorr	+0.009	+0.028	-0.002	-0.003	-0.04
Norm - Fake ℓ	+0.020	+0.037	-0.009	-0.002	-0.04
Norm - Fake D^*	-0.012	-0.011	+0.009	-0.034	-0.33
Norm - Continuum	+0.003	+0.008	+0.000	-0.001	0.00
$\mathcal{B}(D^0 \to K^-\pi^+)$ [18]	—	—	—	-0.081	-0.31
$\mathcal{B}(D^{*+} \to D^0\pi^+)$ [69]	—	—	—	-0.033	-0.13
B^0 life time [69]	—	—	—	-0.026	-0.10
$N(\Upsilon(4S))$	—	—	—	-0.036	-0.14
$f_{+-}/f_{0\bar{0}}$ [69]	-0.003	-0.011	+0.005	+0.001	+0.04
total	0.029	0.062	0.019	0.251	1.04

Table 7.3: The breakdown of the systematic uncertainty in the result of the fit to the full sample of $B^0 \to D^{*-}\ell^+\nu$ events. The "+" ("-") sign indicates that the fit parameter tends to higher (lower) values if the corresponding systematic parameter (*e.g.* the B life time) is increased. This information is important when averaging the results of different analyses.

7.2 B^+ analysis

As can be seen in Tab. 5.2, after applying all selection requirements and subtracting backgrounds, $27,106 \pm 367$ signal events are found in the reconstructed B^+ data. Table 7.4 shows the results of the fit to each sub-channel as well as to the total sample.

Again, the χ^2 values of the fits shown no indication of any problem in the statistical ansatz.

To estimate the systematic uncertainties in the results quoted above, we consider contributions from the following sources: uncertainties in the background component normalizations and shapes, uncertainty in the MC tracking efficiency, PDG errors in $\mathcal{B}(D^{*0} \to D^0\pi^0)$ and $\mathcal{B}(D^0 \to K^-\pi^+)$ [18], and uncertainties in the B^+ lifetime [18] and the total number of B^+ mesons in the data sample.

$\mathcal{B}(D^{*0} \to D^0\pi^0)$, $\mathcal{B}(D^0 \to K^-\pi^+)$, $N(\Upsilon(4S))$ and the B^+ lifetime give an uncertainty on the normalization, but not on the form factors. They are considered analytically, all other uncertainties are investigated numerically. To calculate these systematic uncertainties, we consider 300 pseudo-experiments in which one of 13 quantities (corresponding to the above-mentioned contributions) are randomly varied, taking into account possible correlations between these quantities. The entire analysis chain is repeated for every pseudo-experiment and new values for the fit parameters are obtained. One standard deviation of the pseudo-experiment fit results for a given parameter is used as the systematic uncertainty in this fit parameter. This toy MC approach also allows to derive the systematic correlation coefficients in Table 7.5 in a straightforward way.

In the following, we describe the parameters varied in the pseudoexperiments:

- The tracking efficiencies in five bins of slow pion momentum are varied within their respective uncertainties. These uncertainties are determined from real data by studying the decay $B^+ \to \bar{D}^{*0}\pi^+$ in the same 140 fb^{-1} sample as used for the main analysis. The tracking un-

certainties in different momentum bins are considered fully correlated. Therefore, tracking corresponds only to a single parameter in the toy MC,

- The lepton identification uncertainties are varied within their respective uncertainties [64, 65],

- The normalizations of the 7 background components are varied within the uncertainties determined by the background fit in Sect. 5.4. For Continuum, the on- to off-resonance luminosity ratio is varied by its uncertainty of 1.5 %. Correlations between different background component normalizations are taken into account,

- Additionally, we vary the shape in w of the uncorrelated, combinatoric D^{*0} and fake D^0 components. We fit each of these distributions by a Lorentz distribution and vary each of the parameters within the errors obtained in the fit,

- The number of B^+B^- events is obtained as $N(\Upsilon(4S)) \times \mathcal{B}(\Upsilon(4S) \to B^+B^-)$. We vary the fraction

$$f_{+-}/f_{00} = \mathcal{B}(\Upsilon(4S) \to B^+B^-)/\mathcal{B}(\Upsilon(4S) \to B^0\bar{B}^0)$$

within the error reported by the Particle Data group [18]. This changes both the number of B^+B^- events and the background.

The breakdown of the systematic error quoted in Table 7.4 is given in Table 7.6.
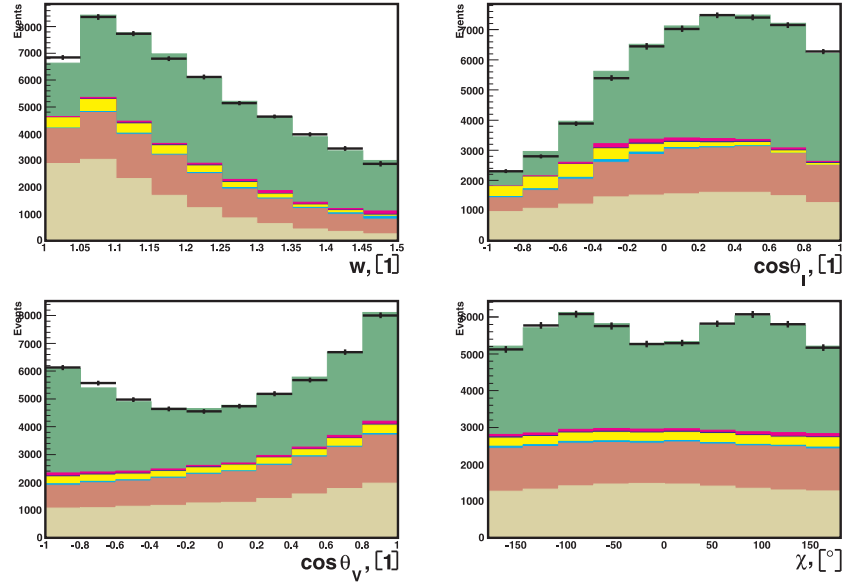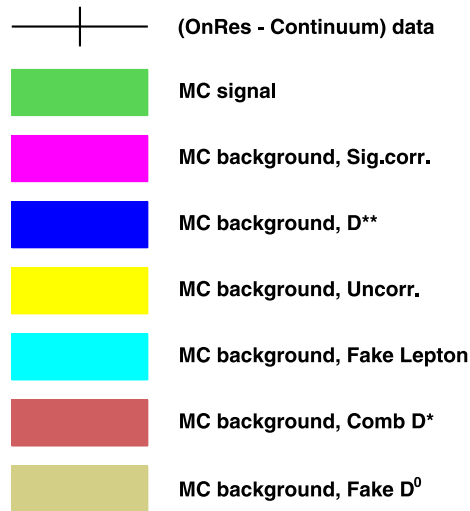
Figure 7.6: Result of the fit of the four kinematic variables in the total sample of $B^+ \to \bar{D}^{*0}\ell^+\nu$ events. (The different sub-samples are added in this plot.) The points with error bars are continuum subtracted on-resonance data. The histograms are the signal and the different background components. The color scheme is explained below.
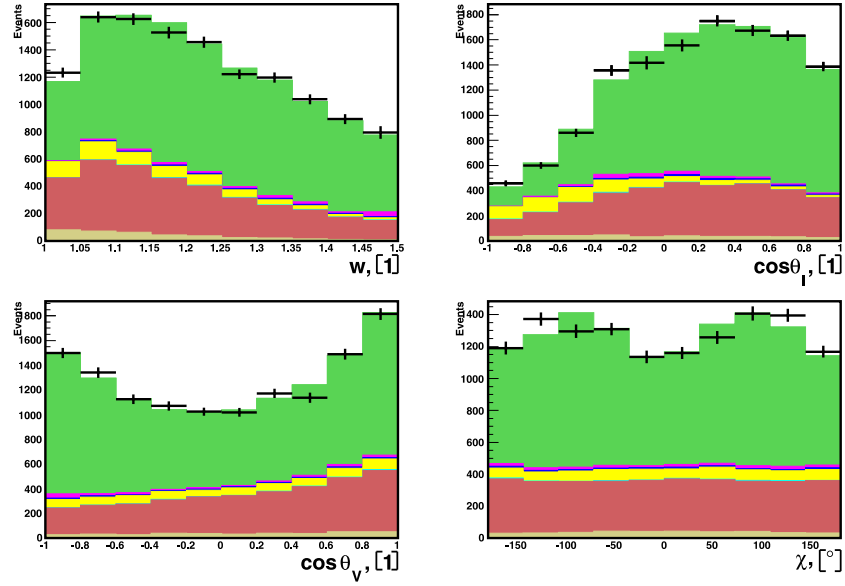
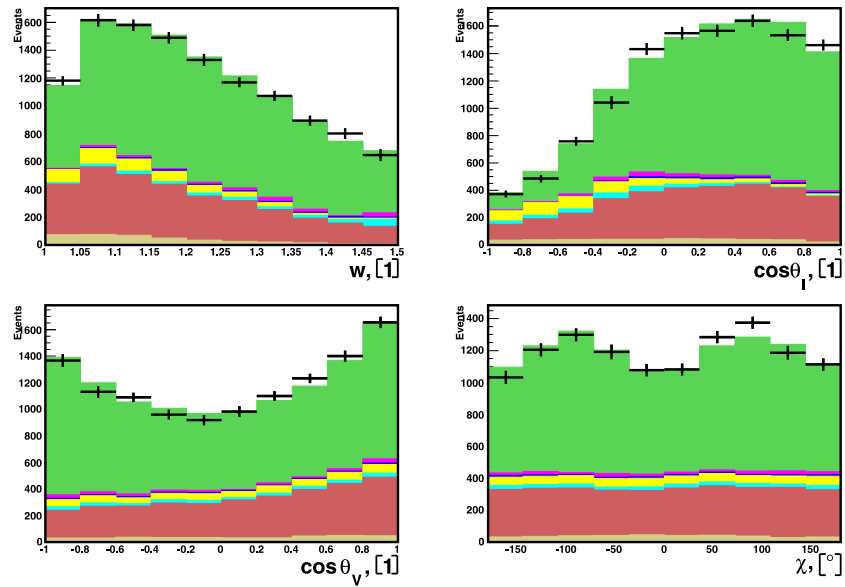Figure 7.7: Same as Fig. 7.6 for the B^+ analysis, $K\pi, e$ sub-sample.

Figure 7.8: Same as Fig. 7.6 for the B^+ analysis, $K\pi, \mu$ sub-sample.
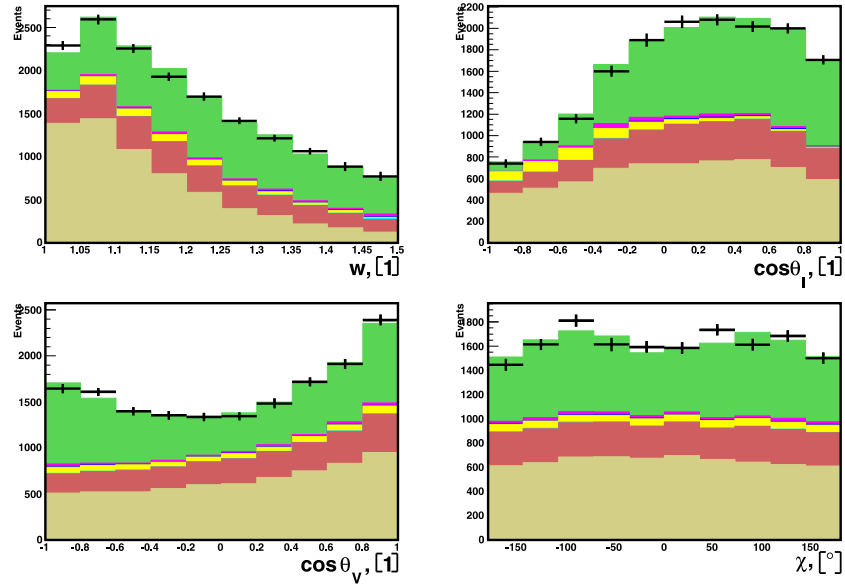
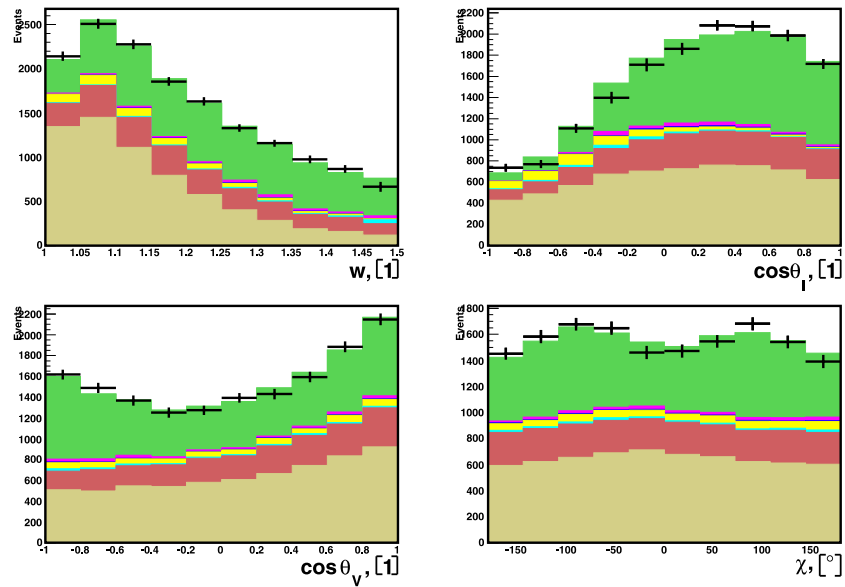Figure 7.9: Same as Fig. 7.6 for the B^+ analysis, $K3\pi, e$ sub-sample.

Figure 7.10: Same as Fig. 7.6 for the B^+ analysis, $K3\pi, \mu$ sub-sample.

	$D^0 \rightarrow K\pi.\ell = e$	$D^0 \rightarrow K\pi.\ \ell = \mu$	$D^0 \rightarrow K3\pi.\ \ell = e$
ρ^2	$1.199 \pm 0.125 \pm 0.048$	$1.370 \pm 0.129 \pm 0.057$	$1.723 \pm 0.162 \pm 0.061$
$R_1(1)$	$1.507 \pm 0.135 \pm 0.090$	$1.568 \pm 0.158 \pm 0.088$	$1.840 \pm 0.271 \pm 0.109$
$R_2(1)$	$0.868 \pm 0.093 \pm 0.034$	$0.839 \pm 0.110 \pm 0.031$	$0.585 \pm 0.198 \pm 0.047$
$R_{K3\pi/K\pi}$	2.072	2.072	2.072
$\mathcal{B}(B^+ \rightarrow \bar{D}^{*0}\ell^+\nu_\ell)$	$4.91 \pm 0.05 \pm 0.57$	$4.77 \pm 0.05 \pm 0.56$	$4.83 \pm 0.07 \pm 0.56$
$\mathcal{F}(1)|V_{cb}| \times 10^3$	$34.3 \pm 0.6 \pm 2.2$	$35.0 \pm 0.6 \pm 2.3$	$36.5 \pm 1.0 \pm 2.3$
$\chi^2/\text{ndf.}$	$48.3\ /\ 36$	$40.6\ /\ 36$	$39.6\ /\ 36$
P_{χ^2}	$8.3\ \%$	$27.5\ \%$	$31.3\ \%$

	$D^0 \rightarrow K3\pi.\ \ell = \mu$	Fit to total sample
ρ^2	$1.434 \pm 0.209 \pm 0.086$	$1.376 \pm 0.074 \pm 0.056$
$R_1(1)$	$1.813 \pm 0.273 \pm 0.106$	$1.620 \pm 0.091 \pm 0.092$
$R_2(1)$	$0.764 \pm 0.191 \pm 0.051$	$0.805 \pm 0.064 \pm 0.036$
$R_{K3\pi/K\pi}$	2.072	2.072 ± 0.023
$\mathcal{B}(B^+ \rightarrow \bar{D}^{*0}\ell^+\nu_\ell)$	$4.83 \pm 0.07 \pm 0.57$	$4.84 \pm 0.04 \pm 0.56$
$\mathcal{F}(1)|V_{cb}| \times 10^3$	$34.8 \pm 1.0 \pm 2.3$	$35.0 \pm 0.4 \pm 2.2$
$\chi^2/\text{ndf.}$	$44.2\ /\ 36$	$187.8\ /\ 155$
P_{χ^2}	$16.3\ \%$	$3.7\ \%$

Table 7.4: The results of the fits to the sub-samples and the fit result on the total sample of $B^+ \rightarrow \bar{D}^{*0}\ell^+\nu$ events. The first error is statistical, the second is the estimated systematic uncertainty. The breakdown of the systematic uncertainty is given in Table 7.6. All numbers are preliminary.

	$\mathcal{F}(1)|V_{cb}|$	ρ^2	$R_1(1)$	$R_2(1)$
$\mathcal{F}(1)|V_{cb}|$	1.000	0.455/0.399/0.295	-0.222 /-0.219/-0.179	-0.054/-0.024/-0.019
ρ^2		1.000	0.648/ 0.413/ 0.540	-0.889/-0.751/-0.841
$R_1(1)$			1.000	-0.749/-0.873/-0.763
$R_2(1)$				1.000

Table 7.5: The statistical/systematic/total correlation coefficients of $\mathcal{F}_1|V_{cb}|$ and the three form factore parameters in the fit to the full sample of $B^+ \to \bar{D}^{*0}\ell^+\nu$ events.

	ρ^2	$R_1(1)$	$R_2(1)$	$\mathcal{F}(1)|V_{cb}| \times 10^3$	$\mathcal{B}(B^+ \to \bar{D}^{*0}\ell^+\nu_\ell)$
Value	1.376	1.620	0.805	34.98	4.841
Statistical Error	0.074	0.091	0.064	0.37	0.044
Tracking	-0.027	+0.025	+0.012	-1.97	-0.491
LeptonID	+0.012	+0.024	-0.011	-0.39	-0.096
Norm - Signal Corr.	-0.007	+0.002	+0.007	+0.13	+0.038
Norm - D^{**}	+0.005	-0.023	+0.002	-0.04	-0.041
Norm - Uncorr	+0.014	+0.074	-0.025	-0.28	-0.023
Norm - Fake ℓ	+0.017	+0.028	-0.010	-0.05	-0.024
Norm - Comb D^{*0}	+0.008	+0.014	-0.008	-0.11	-0.028
Norm - Fake D^0	-0.009	-0.014	+0.007	+0.06	+0.020
Norm - Continuum	+0.004	+0.005	-0.001	0.00	-0.003
Shape - Uncorr	+0.014	+0.003	-0.005	+0.10	
Shape - Comb D^{*0}	+0.027	-0.005	-0.008	+0.21	
Shape - Fake D^0	+0.024	+0.003	+0.008	+0.17	
$\mathcal{B}(D^0 \to K\pi)$				-0.32	-0.089
$\mathcal{B}(D^{*0} \to D^0\pi^0)$				-0.82	-0.227
B^+ lifetime				-0.12	-0.033
$N(\Upsilon(4S))$				-0.14	-0.040
f_{+-}/f_{00}	+0.003	+0.006	-0.003	-0.15	-0.043

Table 7.6: The breakdown of the systematic uncertainty in the result of the fit to the full sample of $B^+ \to \bar{D}^{*0}\ell^+\nu$ events. The "+" ("-") sign indicates that the fit parameter tends to higher (lower) values if the corresponding systematic parameter (*e.g.* the B life time) is increased. This information is important when averaging the results of different analyses.

Chapter 8

Conclusions

Do not believe in anything simply because you have heard it. Do not believe in anything simply because it is spoken and rumored by many. Do not believe in anything merely on the authority of your teachers and elders. But after observation and analysis, when you find that anything agrees with reason and is conducive to the good and benefit of one and all, then accept it and live up to it.

Siddhartha Gautama

The Cabbibo-Kobayashi-Maskawa (CKM) matrix describes the weak interaction between quarks within the standard model. This thesis presents high precision measurements of the CKM matrix element $|V_{cb}|$, which gives the strength of the coupling between the charm and the bottom quark, based on experimental data recorded by the Belle experiment in Tsukuba, Japan. The data sample consists of about 140 fb^{-1} recorded on the $\Upsilon(4S)$ resonance, corresponding to roughly 152×10^6 pairs of B and $\bar{B}$ mesons.

The exclusive decay channels $B^0 \to D^{*-}\ell\nu$ and $B^+ \to \bar{D}^{*0}\ell\nu$ are investigated in two separate analyses using similar techniques, which allows to cross check

the results obtained from two statistically independent samples with each other. In order to determine the spatial momentum of the decaying B meson, a novel reconstruction technique is used, which utilizes the reconstruction of the D^* meson and the light lepton ℓ as well as information obtained by investigating the entire event recorded by the detector.

In order to be able to separate the effects due to quantum chromodynamics (QCD) from those due to the weak interaction, both of which play an important role within the B^0 and the B^+ meson, an effective field theory is used, the so-called "Heavy Quark Effective Theory" (HQET). Additionally, a parametrization scheme based on dispersion relations is utilized. In this approach, a set of three form factor parameters, labeled ρ^2, $R_1(1)$ and $R_2(1)$, describe the distribution of the decays in phase space. $|V_{cb}|$ times a form factor normalization $\mathcal{F}(1)$, which is obtained from lattice QCD calculations, defines the overall normalization of the distribution, and thus the number of decays which can be reconstructed. All free parameters are determined simultaneously from a numerical fit to the distributions in four kinematic variables.

The preliminary results of the analysis of B^0 decays, based on about 69,000 reconstructed $B^0 \to D^{*-}\ell^+\nu_\ell$ decays, are $\rho^2 = 1.293 \pm 0.045 \pm 0.029$, $R_1(1) = 1.495 \pm 0.050 \pm 0.062$, $R_2(1) = 0.844 \pm 0.034 \pm 0.019$ and $\mathcal{F}(1)|V_{cb}| = 34.4 \pm 0.2 \pm 1.0$. The analysis of B^+ decays, based on about 27,000 reconstructed $B^+ \to \bar{D}^{*0}\ell^+\nu_\ell$ events, yields $\rho^2 = 1.376 \pm 0.074 \pm 0.056$, $R_1(1) = 1.620 \pm 0.091 \pm 0.092$, $R_2(1) = 0.805 \pm 0.064 \pm 0.036$ and $\mathcal{F}(1)|V_{cb}| = 35.0 \pm 0.4 \pm 2.2$. The first of the errors stated above shows the statistical uncertainty, the second error gives the systematic one.

The results presented here have not yet been fully incorporated into the world average for $|V_{cb}|$, which is being calculated by the "Heavy Flavor Averaging Group" (HFAG, [10]). However, preliminary updates to the world average, as presented in Fig. 8.1, show that the discrepancies between the various measurements, which are currently available, cannot be solved by the preliminary results shown above. Even more detailed investigations are currently being prepared using the entire data sample of $\Upsilon(4S)$ events collected by the Belle experiment, corresponding to about 710 fb^{-1}.
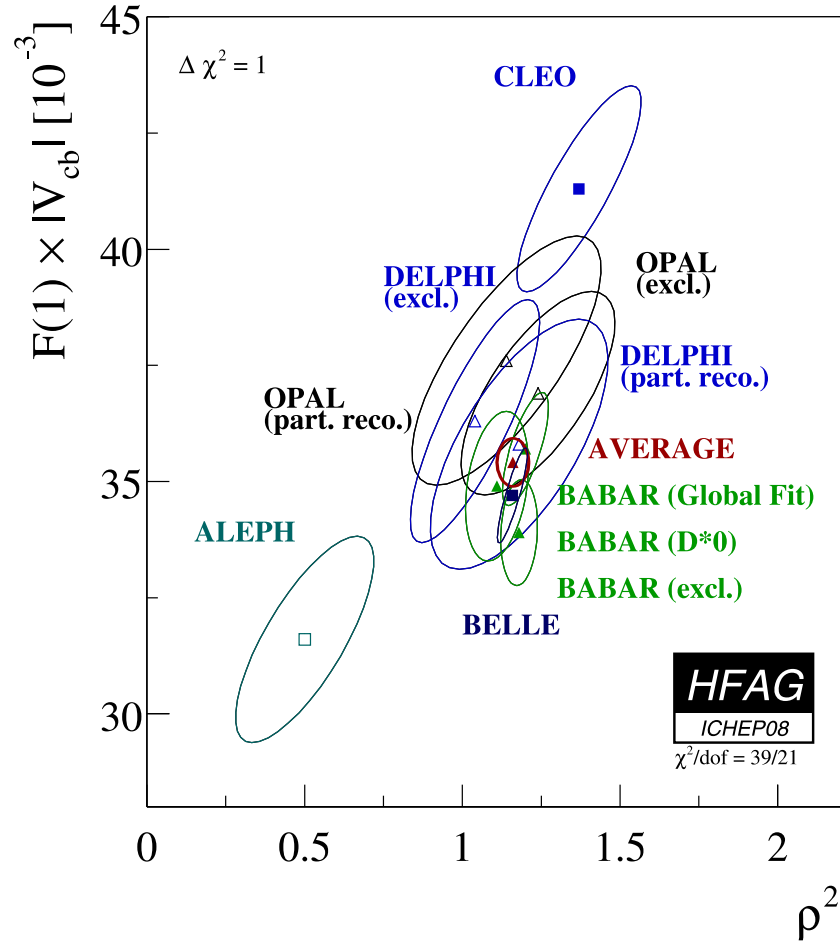
Figure 8.1: Comparison of all available results of exclusive measurements of the form factor parameter ρ^2 and $\mathcal{F}(1)|V_{cb}|$, created by the Heavy Flavor Averaging Group (HFAG, [10]). The ellipses indicate the 1σ uncertainty regions in the parameters and the correlation between them (in the tilt of the ellipse compared to the coordinate axes). The status shown here corresponds to the preliminary update published by HFAG in summer 2008. The preliminary Belle result based on the analysis of the decays of B^0 mesons, which has been discussed in this work ([1]), is included and indicated as the dark blue rectangle (central value) and ellipse (region of uncertainty).

Appendix A

Supplement - Fit procedure

... the world formula allows to derive the entirety of physics from it. All that is missing are some technical details.

Werner Heisenberg (1958).

This empty square shall show the world that I am able to draw like Tizian. All that is missing are some technical details.

Wolfgang Pauli, in reply to above claim.

A.1 Correlation between fit distributions

As mentioned in Section 6.1, the covariance matrix used in the fit to determine the value of V_{cb} and form factors is not diagonal. Rather, the fact that we simultaneously fit four one-dimensional marginal distributions introduces correlations between the histograms of the kinematic variables. The ansatz to estimate these correlations can be derived as follows [70].

Let us divide the distrubutions in w, $\cos\theta_\ell$, $\cos\theta_V$ and χ into n bins each
and let N_i be the content of the bin i. Furthermore, let us build a two-
dimensional histogram by plotting the kinematic variables against each other.
The contents of these 6 histograms (w vs. $\cos\theta_\ell$, w vs. $\cos\theta_V$, w vs. χ, $\cos\theta_\ell$
vs. $\cos\theta_V$, $\cos\theta_\ell$ vs. χ, $\cos\theta_V$ vs. χ), containing $n \times n$ bins each[1], are labeled
with N_{ij}. Naturally, the one-dimensional distributions can be obtained by
integrating the two-dimensional distribution. Similarly, the bin content of
the one-dimensional histogram can be written as the sum of the bin contents
of the two-dimensional histogram,

$$N_i = \sum_j N_{ij}, \ N_j = \sum_i N_{ij}. \tag{A.1}$$

Let us now consider the expectation value of the product of the bin con-
tents of two different bins of the one-dimensional histogram, $E(N_iN_j)$. The
expectation value is a linear function, therefore we can write this expression
as

$$E(N_iN_j) = E\left(\sum_n N_{in} \sum_m N_{mj}\right) = \sum_m \sum_n E(N_{in}N_{mj}). \tag{A.2}$$

For the two-dimensional histogram, the expectation value $E(N_{in}N_{mj})$ can be
easily calculated. Depending on whether or not the bin (i, n) is identical to
(m, j) or not, we find according to the multinomial distribution

$$E(N_{in}N_{mj}) = \begin{cases} Np_{in}, & \forall (i,n) = (m,j) \\ Np_{in} \, Np_{mj} - Np_{in}p_{mj}, & \text{else} \end{cases}, \tag{A.3}$$

where N is the total number of events and p_{xy} is the relative abundance of
the bin (x, y) in the two-dimensional histogram. Similarly p_x shall be the
relative abundance of the bin (x) in the one-dimensional distribution.

By definition, the relations

$$\sum_m p_{mj} = p_j, \sum_n p_{in} = p_i, \tag{A.4}$$

---

[1] All the formulae in this section are equally valid for cases, where the number of bins
is not identical in each of the kinematic variables.

have to hold. Separating the double sum in Eq. A.2 in order to cope with the
case differentiaion in Eq. A.3, we can therefore derive

$$
\begin{aligned}
E(N_i N_j) = \sum_m \sum_n E(N_{in} N_{mj}) = \\
= E(N_{ij} N_{ij}) + \sum_{m \neq i} (N p_{ij}\, N p_{mj} - N p_{ij} p_{mj}) + \\
+ \sum_m \sum_{n \neq j} (N p_{in}\, N p_{mj} - N p_{in} p_{mj}) = \\
= N p_{ij} + N p_{ij}\, N \left(\sum_{m \neq i} p_{mj} \right) - N p_{ij} \left(\sum_{m \neq i} p_{mj} \right) + \\
+ N \left(\sum_{n \neq j} p_{in} \right) N p_j - N \left(\sum_{n \neq j} p_{in} \right) p_j = \\
= N p_{ij} + N p_{ij}\, N\,(p_j - p_{ij}) - N p_{ij}\,(p_j - p_{ij}) + \\
+ N\,(p_i - p_{ij})\, N p_j - N\,(p_i - p_{ij})\, p_j = \\
= N p_{ij} + N p_{ij}\, N p_j - N p_{ij}\, N p_{ij} - N p_{ij} p_j + N p_{ij} p_{ij} + \\
+ N p_i\, N p_j - N p_{ij}\, N p_j - N p_i p_j + N p_{ij} p_j = \\
= N p_i\, N p_j + N p_{ij} - N p_i p_j,
\end{aligned}
\tag{A.5}
$$

which can finally be written as

$$
E(N_i N_j) = E(N_i) E(N_j) + N p_{ij} - N p_i p_j.
\tag{A.6}
$$

On the other hand, from the definition of the covariance we find

$$
E(N_i N_j) = cov(N_i N_j) + E(N_i) E(N_j)
\tag{A.7}
$$

which leads to

$$
C_{ij} = cov(N_i N_j) = N p_{ij} - N p_i p_j,
\tag{A.8}
$$

as stated in Eq. 6.4.

There are three special cases of covariances one can consider. In case of sta-
tistically independent variables, the relation $p_{ij} = p_i p_j$ has to hold, therefore
all diagonal elements vanish. The covariance matrix becomes diagonal and

the fits to the individual kinematic variables decouple completely, as they should.

In case of perfect anti-correlation between two bins, the bin of the two dimensional distribution corresponding to the pair has to be empty. The covariance as given by Eq. 6.4 becomes negative. In case of positive correlation the opposite holds and the covariance matrix element will be positive.

A.2   Proof of principle using toy Monte Carlo

In order to test the statistical viability of the approach described above, we created 900 sets of histograms according to the theoretical distributions in Eq. 3.27 and applied the fit procedure to each of them. The parameters which have been used to generate the histograms are naturally known and it is therefore possible to compare the estimated parameters as determined by the fit to the true values. One variable of particular interest is the so-called standartized residual r, which is defined for any variable v by,

$$r_v = \frac{v^{estimated} - v^{true}}{\sigma_v^{estimated}}, \tag{A.9}$$

where $v^{estimated}$ (v^{true}) is the fitted (true) value of the variable and $\sigma_v^{estimated}$ is the standard deviation obtained from the fit procedure. If the ansatz of the statistical estimate is sound, the distribution of the standartized residuals will be normal distributed, since there is no bias in the central value and the estimated uncertainty equals the actual spread of the results due to statistical fluctuations. As can be seen in Fig A.2, A.3 and A.4, this is the case for each of the parameters ρ^2, R_1 and R_2. For V_{cb}, shown in Fig. A.1, there is no perfect, but still acceptable agreement between the distribution of standartized residuals and a normal distribution.

The number of events as estimated by the fit deviates from the actual generated number by a factor of about 3×10^{-5} and is therefore in excellent agreement.

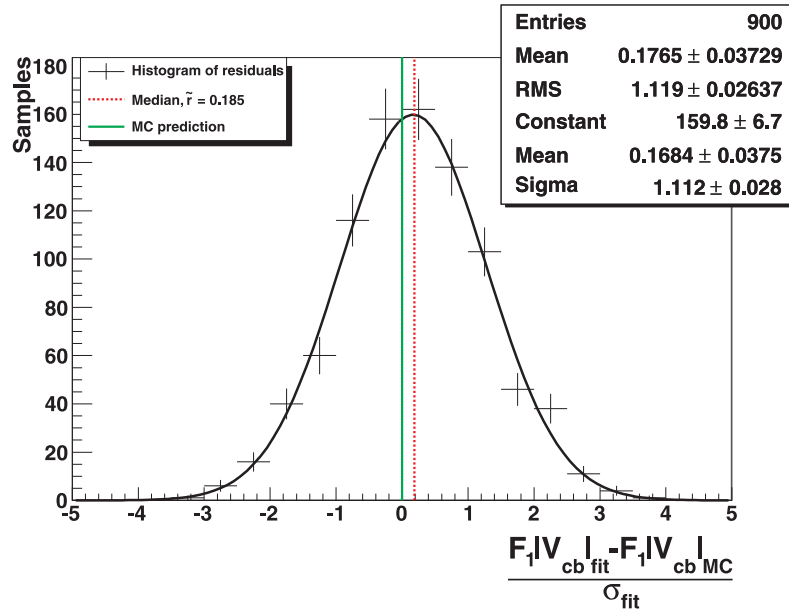These results show that the method is stable and works as intended.

Figure A.1: The histogram of residuals of the fit parameter corresponding to $\mathcal{F}_1|V_{cb}|$. The green line indicates where perfect agreement with the original inputs can be obtained, the red dotted line gives the median of the 900 investigated fits. Ideally the distribution, fitted here with a gaussian function, should be distributed like a normal distribution (central value of 0 and width equal 1).
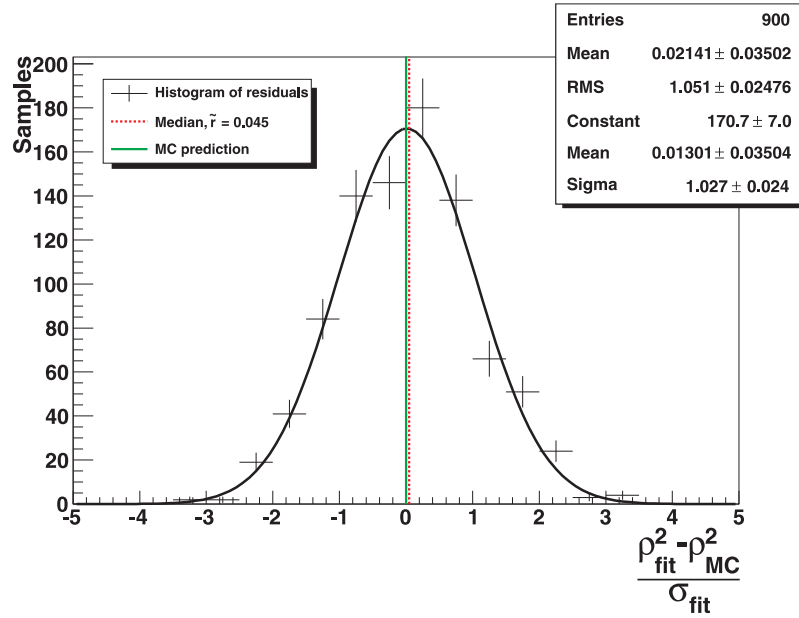
Figure A.2: Same as Fig. A.1 for the parameter ρ^2.
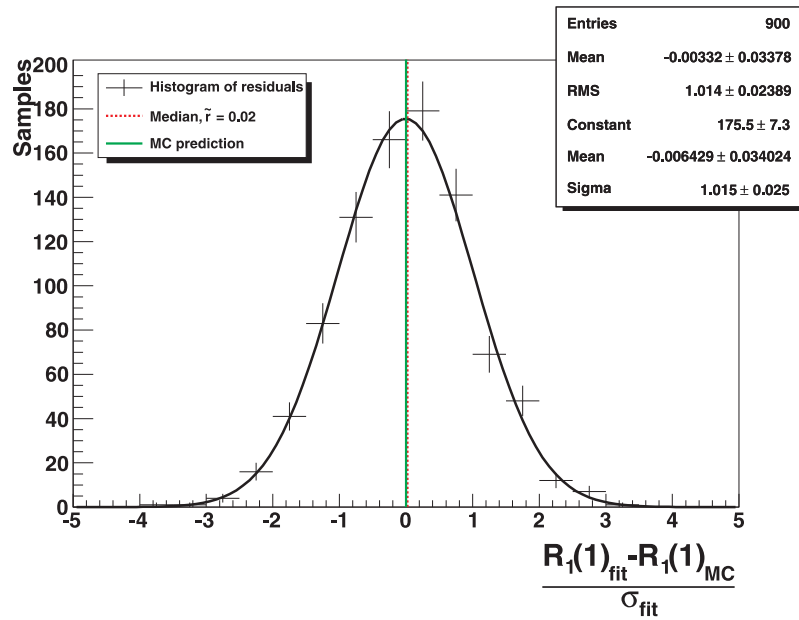
Figure A.3: Same as Fig. A.1 for the parameter $R_1(1)$.

Figure A.4: Same as Fig. A.1 for the parameter $R_2(1)$.
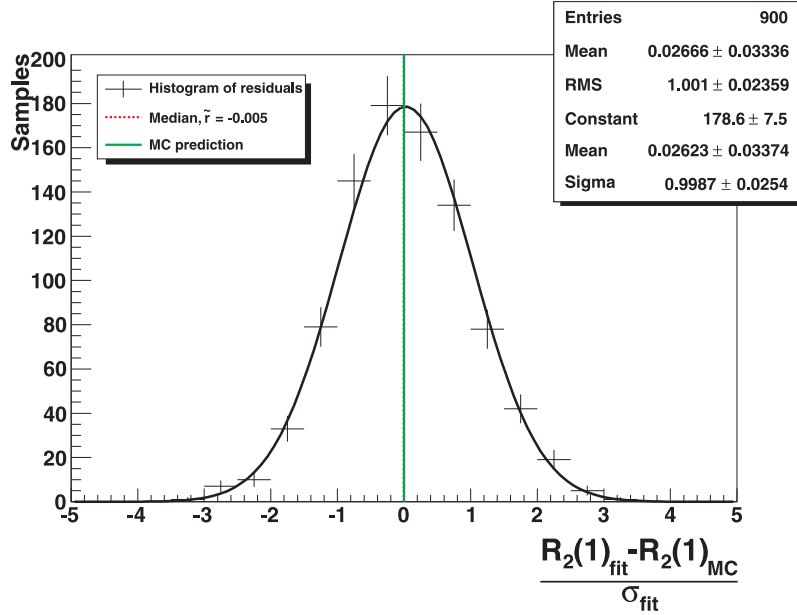
A.3   Monte Carlo samples created with the EVTGEN program

As mentioned above, the EVTGEN program [59] is used by the Belle collaboration to generate simulated events, which can be used e.g. to study backgrounds in analyses of Belle data. Semileptonic decays like $B \to D^*\ell\nu$ are generated by the parametrization described in Section 3.6. However, when comparing the generated distributions in w to the theoretical prediction, small discrepancies appear.

Tab. A.1 and A.2 show the ratio between the central value expected due to the theoretical prediction and the the generated distribution containing 4×10^7 events. The ratio is shown in 10 bins of the variable w. Due to the large number of generated events, the statistical error is negligible. As can be seen, the deviation is minimal over the largest part of the w distribution and becomes significant only in the region of large values of w, where only a small portion of the events resides since the available phase space vanishes.

	N^{exp}/N^{MC}	Phasespace in this region
$w \in (1.00.1.05)$	0.996	0.061
$w \in (1.05, 1.10)$	0.995	0.101
$w \in (1.10.1.15)$	0.995	0.116
$w \in (1.15, 1.20)$	0.996	0.121
$w \in (1.20.1.25)$	0.996	0.120
$w \in (1.25, 1.30)$	0.996	0.114
$w \in (1.30.1.35)$	0.997	0.106
$w \in (1.35, 1.40)$	0.999	0.097
$w \in (1.40.1.45)$	1.002	0.085
$w \in (1.45, 1.50)$	1.022	0.074
$w > 1.50$	1.387	0.005

Table A.1: Ratio between the theoretical prediction and the Monte Carlo simulated distributions for B^0. Additionally, the fraction of events in the corresponding region of phase space is shown.

These discrepancies are not due to some problem in coding the formulae given in Section 3.6. Rather, when comparing the underlying distributions, we find a match within the numerical accuracy, which can be seen in Fig. A.5.

In any case this deviation does not impact the calculation of $|V_{cb}|$ from real data. The fit as described in Chapter 6 does not depend on signal events simulated by Monte Carlo, but rather directly utilizes the theoretical predictions specified in Chapter 3.

A.4   Fit of simulated events after full detector simulation

As a final test of the fit procedure, we investigated simulated events, which have passed a full detector simulation based on GEANT [60]. These samples, corresponding in size to the sample reconstructed in real data, allow to test the fit procedure in a realistic setup. Due to the large computer resource consumption of the full detector simulation, only three samples were available. Therefore, no full statistical analysis similar to the one shown in

	N^{exp}/N^{MC}	Phasespace in this region
$w \in (1.00.1.05)$	0.993	0.061
$w \in (1.05, 1.10)$	0.999	0.101
$w \in (1.10.1.15)$	0.994	0.115
$w \in (1.15, 1.20)$	1.000	0.121
$w \in (1.20.1.25)$	0.997	0.119
$w \in (1.25, 1.30)$	0.999	0.114
$w \in (1.30.1.35)$	0.996	0.106
$w \in (1.35, 1.40)$	1.000	0.097
$w \in (1.40.1.45)$	1.001	0.086
$w \in (1.45, 1.50)$	1.011	0.074
$w > 1.50$	1.223	0.007

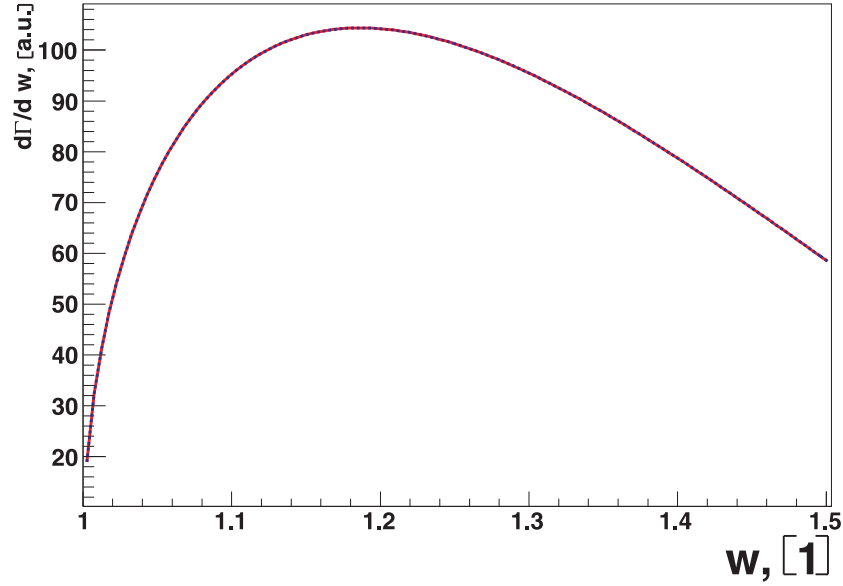Table A.2: Same as Tab. A.1 for generated B^+ events.

Figure A.5: Comparison between the w distribution as used by the EVTGEN Monte Carlo event generator (red solid line) and the code used in the fitting procedure described above (blue dashed line). The two distributions agree within the numerical accuracy.

	stream 0	stream 1	stream 2	MC truth
ρ^2	1.437 ± 0.030	1.426 ± 0.030	1.471 ± 0.030	1.44
$R_1(1)$	1.146 ± 0.032	1.148 ± 0.031	1.180 ± 0.031	1.18
$R_2(1)$	0.700 ± 0.024	0.753 ± 0.024	0.699 ± 0.026	0.71
$R_{K3\pi/K\pi}$	1.861 ± 0.005	1.854 ± 0.005	1.839 ± 0.005	≈ 1.85
$\mathcal{B}(B^+)$	5.170 ± 0.032	5.175 ± 0.032	5.223 ± 0.032	5.20
χ^2/n.d.f.	147.4 / 155	146.0 / 155	177.8 / 155	
P_{χ^2}	65.6 %	68.6 %	10.1 %	

Table A.3: Results of the tests of the fit procedure on Monte Carlo data after full detector simulation for B^0.

	stream 0	stream 1	stream 2	MC truth
ρ^2	1.353 ± 0.049	1.468 ± 0.048	1.479 ± 0.048	1.44
$R_1(1)$	1.105 ± 0.047	1.178 ± 0.052	1.189 ± 0.051	1.18
$R_2(1)$	0.783 ± 0.039	0.701 ± 0.045	0.676 ± 0.045	0.71
$R_{K3\pi/K\pi}$	1.799 ± 0.013	1.912 ± 0.014	1.873 ± 0.014	≈ 1.855
$\mathcal{B}(B^0)$	5.765 ± 0.047	5.618 ± 0.046	5.662 ± 0.046	5.65
χ^2/n.d.f.	199.1 / 155	173.6 / 155	150.0 / 155	
P_{χ^2}	1.0 %	14.6 %	59.9 %	

Table A.4: Results of the tests of the fit procedure on Monte Carlo data after full detector simulation for B^+.

Section A.2 is available, but a qualtiative investigation is possible. The results are shown in Tab. A.3 and A.4. Agreement between the results of the fits and the Monte Carlo parameters is good, which implies that the procedure works dependably under realistic conditions.

Appendix B

Acronyms

"What does AFTEOA stand for?"
"Association For The Elimination Of Acronyms."

QCD Quantum chromodynamics

HQET Heavy Quark Effective Theory

SM Standard Model

HER high energy ring

LER low energy ring

SVD Silicon Vertex Detector

CDC Central Drift Chamber

ACC Aerogel Čerenkov Counter system

TOF Time-Of-Flight scintillation counters

ECL Electromagnetic Calorimeter

KLM K_L and μ detection system

EFC Extreme Forward Calorimeter

Bibliography

[1] I. Adachi, et al. (Belle). *Measurement of the form factors of the decay* $B^0 \to D^{*-}\ell^+\nu_\ell$ *and determination of the CKM matrix element* $|V_{cb}|$ (2008), `arXiv:0810.1657[hep-ex]`

[2] I. Adachi, et al. (Belle). *Measurement of the form factors of the decay* $B^+ \to \bar{D}^{*0}\ell^+\nu_\ell$ *and determination of the CKM matrix element* $|V_{cb}|$ (2009), `arXiv:0910.3534[hep-ex]`

[3] M. Kobayashi, T. Maskawa. *CP-Violation in the Renormalizable Theory of Weak interaction.* Prog. Theo. Phys. **49**, 2, pp. 652–657 (1973)

[4] M. Neubert. *Heavy quark symmetry.* Phys. Rept. **245**, pp. 259–396 (1994), `arXiv:hep-ph/9306320`

[5] I. Caprini, L. Lellouch, M. Neubert. *Dispersive bounds on the shape of* $B \to D^{(*)}\ell\nu$ *form factors.* Nucl. Phys. **B530**, pp. 153–181 (1998), `arXiv:hep-ph/9712417`

[6] C. Bernard, et al. *The* $\bar{B} \to D^*\ell\bar{\nu}$ *form factor at zero recoil from three-flavor lattice QCD: A Model independent determination of* $|V_{cb}|$. Phys. Rev. **D79**, p. 014506 (2009), `arXiv:0808.2519[hep-lat]`

[7] R. A. Briere, et al. (CLEO). *Improved Measurement of |Vcb| using B –> D* l nu Decays.* Phys. Rev. Lett. **89**, p. 081803 (2002), `arXiv:hep-ex/0203032`

[8] K. Abe, et al. (Belle). *Determination of |V(cb)| using the semileptonic decay anti-B0 –> D*+ e- anti-nu.* Phys. Lett. **B526**, pp. 247–257 (2002), `arXiv:hep-ex/0111060`

[9] B. Aubert, et al. (BABAR). *Determination of the form-factors for the decay $B^0 \to D^{*-}\ell^+\nu_l$ and of the CKM matrix element $|V_{cb}|$.* Phys. Rev. **D77**, p. 032002 (2008), `arXiv:0705.4008[hep-ex]`

[10] E. Barberio, et al. (Heavy Flavor Averaging Group). *Averages of $b-$hadron and $c-$hadron Properties at the End of 2007* online update at: `http://www.slac.stanford.edu/xorg/hfag` (2008), `arXiv:0808.1297[hep-ex]`

[11] H. Albrecht, et al. (ARGUS). *Measurement of the decay B- $\to$ D*0 l-anti-neutrino.* Phys. Lett. **B275**, pp. 195–201 (1992)

[12] N. E. Adam, et al. (CLEO). *Determination of the anti-B –> D* l anti-nu decay width and |V(cb)|. ((B)).* Phys. Rev. **D67**, p. 032001 (2003), `arXiv:hep-ex/0210040`

[13] B. Aubert, et al. (BABAR). *Measurement of the Decay $B^- \to D^{*0}e^-\bar{\nu}_e$.* Phys. Rev. Lett. **100**, p. 231803 (2008), `arXiv:0712.3493[hep-ex]`

[14] E. Noether. *Invarianten beliebiger Differentialausdrücke.* Gött. Nachr. **1918**, pp. 37–44 (1918)

[15] E. Noether. *Invariante Variationsprobleme.* Gött. Nachr. **1918**, pp. 235–257 (1918)

[16] W. Pauli (Editor). *N. Bohr and the Development of Physics.* McGraw-Hill, New York (1955)

[17] G. Luders. *Proof of the TCP theorem.* Annals Phys. **2**, pp. 1–15 (1957)

[18] C. Amsler *et al.* (Particle Data Group) (Particle Data Group). *Review of Particle Physics.* Phys. Lett. **B667**, p. 1 (2008)

[19] J. H. Christenson, J. W. Cronin, V. L. Fitch, R. Turlay. *Evidence for the 2π Decay of the K2 Meson.* Phys. Rev. Lett. **13**, 4, pp. 138–140 (1964)

[20] Glashow, S. L., Iliopoulos, J. and Maiani L. *Weak Interactions with Lepton-Hadron Symmetry.* Phys. Rev. D **2**, 7, pp. 1285–1292 (1970)

[21] N. Cabibbo. *Unitary Symmetry and Leptonic Decays.* Phys. Rev. Lett. **10**, 12, pp. 531–533 (1963)

[22] L. Wolfenstein. *Parametrization of the Kobayashi-Maskawa Matrix.* Phys. Rev. Lett. **51**, 21, pp. 1945–1947 (1983)

[23] L.-L. Chau, W.-Y. Keung. *Comments on the Parametrization of the Kobayashi-Maskawa Matrix.* Phys. Rev. Lett. **53**, p. 1802 (1984)

[24] J. Charles *et al.* (CKM Fitter). *Review of Particle Physics.* Eur. Phys. J. C **41**, pp. 1–131.
updated results and plots available at: `http://ckmfitter.in2p3.fr` (2005)

[25] J. D. Richman, P. R. Burchat. *Leptonic and semileptonic decays of charm and bottom hadrons.* Rev. Mod. Phys. **67**, pp. 893–976 (1995), `arXiv:hep-ph/9508250`

[26] D. J. Gross, F. Wilczek. *Ultraviolet Behavior of Non-Abelian Gauge Theories.* Phys. Rev. Lett. **30**, pp. 1343–1346 (1973)

[27] H. D. Politzer. *Reliable Perturbative Results for Strong Interactions?* Phys. Rev. Lett. **30**, pp. 1346–1349 (1973)

[28] N. Isgur, M. B. Wise. *Heavy quark symmetry.* Adv. Ser. Direct. High Energy Phys. **10**, pp. 549–572 (1992)

[29] H. Georgi. *An Effective Field Theory for Heavy Quarks at low-energies.* Phys. Lett. **B240**, pp. 447–450 (1990)

[30] E. Eichten, F. Feinberg. *Spin Dependent Forces in QCD.* Phys. Rev. **D23**, p. 2724 (1981)

[31] M. A. Shifman, M. B. Voloshin. *On Annihilation of Mesons Built from Heavy and Light Quark and anti-B0 <—> B0 Oscillations.* Sov. J. Nucl. Phys. **45**, p. 292 (1987)

[32] S. Nussinov, W. Wetzel. *Comparison of Exclusive Decay Rates for b →
u and b → c Transitions.* Phys. Rev. **D36**, p. 130 (1987)

[33] N. Isgur, M. B. Wise. *Weak Decays of Heavy Mesons in the Static
Quark Approximation.* Phys. Lett. **B232**, p. 113 (1989)

[34] N. Isgur, M. B. Wise. *Weak transition form-factors between heavy
mesons.* Phys. Lett. **B237**, p. 527 (1990)

[35] M. Wirbel, B. Stech, M. Bauer. *Exclusive Semileptonic Decays of
Heavy Mesons.* Z. Phys. **C29**, p. 637 (1985)

[36] F. J. Gilman, R. L. Singleton. *Analysis of semileptonic decays of
mesons containing heavy quarks.* Phys. Rev. D **41**, 1, pp. 142–150
(1990)

[37] J. G. Korner, G. A. Schuler. *Exclusive Semileptonic Heavy Meson
Decays Including Lepton Mass Effects.* Z. Phys. **C46**, p. 93 (1990)

[38] S. Okubo. *Exact bounds for k-l-3 decay parameters.* Phys. Rev. **D3**,
pp. 2807–2813 (1971)

[39] S. Okubo, I.-F. Shih. *Exact inequality and test of chiral sw(3) theory in
k-l-3 decay problem.* Phys. Rev. **D4**, pp. 2020–2029 (1971)

[40] V. Singh, A. K. Raina. *Bounds on Form-Factors and Propagators.*
Fortschr. Phys. **27**, p. 561 (1979)

[41] C. Bourrely, B. Machet, E. de Rafael. *Semileptonic decays of
pseudoscalar particles (M → M′⁻ℓν_ℓ) and short distance behavior of
quantum chromodysnamics.* Nucl. Phys. **B189**, p. 157 (1981)

[42] S. Hashimoto, A. S. Kronfeld, P. B. Mackenzie, S. M. Ryan, J. N.
Simone. *Lattice calculation of the zero recoil form factor of anti-B –>
D* l anti-nu: Toward a model independent determination of |V(cb)|.*
Phys. Rev. **D66**, p. 014503 (2002), arXiv:hep-ph/0110253

[43] N. Uraltsev. *Topics in the heavy quark expansion* (2000),
arXiv:hep-ph/0010328

[44] D. Buskulic, et al. (ALEPH). *Measurements of |V(cb)|, form factors and branching fractions in the decays anti-B0 -> D*+ l- anti-nu/l and anti-B0 -> D+ l- anti-nu/l*. Phys. Lett. **B395**, pp. 373–387 (1997)

[45] G. Abbiendi, et al. (OPAL). *Measurement of |V(cb)| using anti-B0 -> D*+ l- anti-nu decays*. Phys. Lett. **B482**, pp. 15–30 (2000), arXiv:hep-ex/0003013

[46] P. Abreu, et al. (DELPHI). *Measurement of V(cb) from the decay process anti-B0 -> D*+ l- anti-nu*. Phys. Lett. **B510**, pp. 55–74 (2001), arXiv:hep-ex/0104026

[47] J. Abdallah, et al. (DELPHI). *Measurement of |V(cb)| using the semileptonic decay anti- B/d0 -> D*+ l- anti-nu/l*. Eur. Phys. J. **C33**, pp. 213–232 (2004), arXiv:hep-ex/0401023

[48] J. E. Duboscq, et al. (CLEO). *Measurement of the form-factors for $\bar{B}^0 \to D^{*+}\ell\bar{\nu}u$*. Phys. Rev. Lett. **76**, pp. 3898–3902 (1996)

[49] The Belle Collaboration. *Web center* (http:\\belle.kek.jp)

[50] T. E. Browder, K. Honscheid. *B mesons*. Prog. Part. Nucl. Phys. **35**, pp. 81–220 (1995), arXiv:hep-ph/9503414

[51] The Belle Collaboration. *The Belle detector*. Nuclear Instruments and Methods in Physics Research, Section A **479 (1)**, pp. 117–232 (2002), URL doi:10.1016/j.physletb.2003.10.071

[52] R. Abe, et al. *Belle/SVD2 status and performance*. Nucl. Instrum. Meth. **A535**, pp. 379–383 (2004)

[53] R. Cardarelli, et al. *Progress in resistive plate counters*. Nuclear Instruments and Methods in Physics Research, Section A **263 (1)**, pp. 20–65 (1988), URL doi:10.1016/0168-9002(88)91011-X

[54] E. Gorini. *The Resistive plate counter muon system of E771*. Nucl. Phys. Proc. Suppl. **23B**, pp. 249–253 (1991)

[55] L. Antoniazzi, et al. *Resistive plate counters readout system.* Nuclear Instruments and Methods in Physics Research, Section A **307 (2-3)**, pp. 312–315 (1991), URL doi:10.1016/0168-9002(91)90198-Y

[56] Y.Makida, et al. *Performance of a Thin Superconducting Solenoid for Particle Astrophysics.* Advances in Cryogenic Engineering **37**, pp. 401–407 (1992)

[57] The Belle Collaboration. *Belle Technical Design Report.* KEK Report **95-1**, pp. 401–407 (1995)

[58] The Belle Collaboration. *KEKB B-Factory Design Report.* KEK Report **95-7**, pp. 401–407 (1995)

[59] D. Lange. *The EvtGen particle decay simulation package.* Nucl. Instrum. Meth A **462**, p. 152 (2001)

[60] R. Brun, F. Bruyant, M. Maire, A. C. McPherson, P. Zanarini. *GEANT3.* CERN-DD/EE/84 - 1 (1984)

[61] E. Barberio, Z. Was. *PHOTOS: A Universal Monte Carlo for QED radiative corrections. Version 2.0.* Comput. Phys. Commun. **79**, pp. 291–308 (1994)

[62] K. Abe *et al.* (Belle). *Measurement of inclusive production of neutral pions from* $\Upsilon(4S)$. Phys. Rev. D **64**, p. 072001 (2001), arXiv:hep-ex/0103041

[63] G. C. Fox, S. Wolfram. *Observables for the Analysis of Event Shapes in e+ e- Annihilation and Other Processes.* Phys. Rev. Lett. **41**, p. 1581 (1978)

[64] K. Hanagaki, H. Kakuno, H. Ikeda, T. Iijima and T. Tsukamoto. *Electron identification in Belle.* Nucl. Instrum. Meth. A **485**, p. 490 (2002), arXiv:hep-ex/0108044

[65] A. Abashian *et al. Muon identification in the Belle experiment at KEKB.* Nucl. Instrum. Meth. A **491**, p. 69 (2002)

[66] R. Brun, F. Rademakers. *ROOT: An object oriented data analysis framework.* Nucl. Instrum. Meth. **A389**, pp. 81–86 (1997)

[67] R. J. Barlow, C. Beeston. *Fitting using finite Monte Carlo samples.* Comput. Phys. Commun. **77**, pp. 219–228 (1993)

[68] F. James, M. Roos. *Minuit: A System for Function Minimization and Analysis of the Parameter Errors and Correlations.* Comput. Phys. Commun. **10**, pp. 343–367 (1975)

[69] W. M. Yao *et al.* (Particle Data Group) (Particle Data Group). *Review of Particle Physics.* J. Phys. **G33**, p. 1 (2006)

[70] R. Frühwirth. *Private communication*

Acknowledgements

At the end of this work I would like to take the time to give thanks for the support I received during the last three years - support which was vital for the advance and conclusion of this work. Listing everyone by name would mean a work of gigantic proportions - there are simply too many.

I want to thank Doz. MMag. Dr. Manfred Jeitler, who, despite being loaded with many important and time-consuming tasks at CERN, agreed to be my thesis director and spent much of his time in long discussions, which showed me many important aspects and facets of physics. This also extends to Univ.Prof. DI Dr. Christian Fabjan, the director of the Institute for High Energy Physics and the second assessor of my thesis. Facing countless duties and the challenging and exciting times of the LHC startup, he nonetheless took the time for this assessment as well.

Within the Institute for High Energy Physics in Vienna, my deep thanks go to DI Dr. Christoph Schwanda, the head of the Belle group of the institute. What I learned about data analysis, the experiment, the collaboration and particle physics as a whole under his guidance can barely be measured. DI Dr. Laurenz Widhalm and DI Dr. Winfried Mitaroff helped me a lot in many different aspects, from day-to-day routines to commenting and proofreading this thesis, and I want to thank them for this. I am deeply indebted to DI Dr. Wolfgang Waltenberger and Univ.Doz. DI Dr. Rudolf Frühwirth for their aid in technical and statistical questions. And I would like to thank Laurenz and Wolfgang for having been great office colleagues - I really enjoyed our many talks and discussions!

This work would not have been possible without the Belle collaboration. I want to thank our physics convenors, Yoshihide Sakai, Paoti Chang and Karim Trabelsi, would had to keep an eye on every single Belle analysis. They provided many important comments on the analyses presented in this work. Elisabetta Barberio, Maria Rozanska and Kevin Varvell reviewed and commented every result before it was presented in public - thank you for your

effort and the discussions! I have to thank (and apologize to) Nishida Shohei, who had been the drop-in point for all comments on computer problems and issues within the Belle computer system. I thank Chihiro Imai, for all the administrative procedures she helped me with every time I was in Japan. And I want to thank Jimmy MacNaughton, who helped me enormously the first time I visited KEK - how I would have managed without this help I do not know.

Dōmo arigatō!

But all the scientific aid cannot be enough without the support of family and friends. My parents and my grandmother, my brother and my sister-in-law, my little niece - they all helped me to keep up, to clear my head from time to time and to weather the storms that came up along the way.

And finally, there is one last thanks I want to give. In academia, the final place on lists is often a place of honor, the place for the one contributor, without whom everything might have unraveled. I want to thank Mag. pharm. Anna-Maria Zimmermann, from the bottom of my heart, for standing by me and supporting me throughout these years. Hopefully I have been able to give something in return as well.

November 2009   Wolfgang Dungel

Curriculum Vitae

Personal data

Dipl.-Ing. Wolfgang Dungel

Leobendorferstrasse 48/4/8, 2100 Korneuburg

Born August 1, 1982 in Vienna

Education

March 2007 – present   Doktoratsstudium der technischen Wissenschaften, Vienna University of Technology

October 2001 – January 2007   Diplomstudium der Technischen Physik, Vienna University of Technology

October 2000 – September 2001   Military service

September 1992 – June 2000   Bundesrealgymnasium Stockerau

Work experience

April 2007 – present   Research assistant at the Institute for High Energy Physics, Austrian Academy of Sciences

Additional activites

June 2009 – present   Member of the European Particle Physics Outreach Group ("EPPOG")

October 2006 – present   Member of the Austrian Phyical Society

December 2003 – present   Member of the "Österreichische Offiziersgesellschaft Wien"

November 2009   Wolfgang Dungel